

2008

# Determination of CTV-to-ITV margin for free-breathing respiratory-gated treatments using 4DCT and the Novalis ExacTrac Gating System with implanted fiducials

Jason Edward Matney

*Louisiana State University and Agricultural and Mechanical College*

Follow this and additional works at: [https://digitalcommons.lsu.edu/gradschool\\_theses](https://digitalcommons.lsu.edu/gradschool_theses)



Part of the [Physical Sciences and Mathematics Commons](#)

---

## Recommended Citation

Matney, Jason Edward, "Determination of CTV-to-ITV margin for free-breathing respiratory-gated treatments using 4DCT and the Novalis ExacTrac Gating System with implanted fiducials" (2008). *LSU Master's Theses*. 2160.

[https://digitalcommons.lsu.edu/gradschool\\_theses/2160](https://digitalcommons.lsu.edu/gradschool_theses/2160)

This Thesis is brought to you for free and open access by the Graduate School at LSU Digital Commons. It has been accepted for inclusion in LSU Master's Theses by an authorized graduate school editor of LSU Digital Commons. For more information, please contact [gradetd@lsu.edu](mailto:gradetd@lsu.edu).

DETERMINATION OF CTV-TO-ITV MARGIN FOR FREE-BREATHING RESPIRATORY-  
GATED TREATMENTS USING 4DCT AND THE NOVALIS EXACTRAC GATING  
SYSTEM WITH IMPLANTED FIDUCIALS

A Thesis

Submitted to the Graduate Faculty of the  
Louisiana State University and  
Agricultural and Mechanical College  
in partial fulfillment of the  
requirements for the degree of  
Master of Science

in

The Department of Physics and Astronomy

by  
Jason Edward Matney  
B.S., Ball State University, 2004  
December 2008

## **Dedication**

To my dear friend, Alex Santos, who lost his battle with cancer four days before his twenty-second birthday.

## **Acknowledgments**

I thank my advisor Dr. Brent Parker for his guidance through the course of my thesis project. His patience and expertise kept this project moving forward in the right direction, and his professional and personal advice has proven invaluable. I cannot begin to express my gratitude for his time and effort. I want to thank my supervisory committee: Isaac Rosen, James Matthews, Greg Henkelmann, and Daniel Neck. Their input and guidance was invaluable in not only improving this project, but providing me with knowledge that will serve me well throughout my entire career.

Thanks to Dr. Kenneth Hogstrom and all the faculty and administrative personnel of the Medical Physics department and for their dedication to the students. Many thanks go to all of the graduate students that I have had the pleasure of interacting with over the past three years. The faculty, administrators, and fellow students have provided an environment for us to excel in our graduate work.

Finally, I would like to thank the men of Louisiana Beta for providing me a home away from home. Collectively, their friendship and support have helped me through the difficult times.

# Table of Contents

Dedication .....	ii
Acknowledgments.....	iii
List of Tables .....	vii
List of Figures.....	ix
Abstract.....	xii
1 Introduction .....	1
1.1 Statement of the Problem .....	1
1.2 Definition of Volumes.....	3
1.3 Definition of Respiration Characteristics .....	5
1.4 Respiratory Gating and Internal Margins .....	7
1.5 Hypothesis .....	7
1.6 References .....	8
2 Aim 1: Develop an Accurate and Efficient Dosimetry System to Measure Distributions of Respiratory-Gated Radiation Therapy Treatments Using Radiochromic Film .....	10
2.1 Introduction .....	10
2.2 Methods and Materials .....	11
2.2.1 Epson V700 Scanner System .....	11
2.2.2 Vidar Scanner System .....	13
2.2.3 Summary of Scanner Characteristics .....	14
2.2.4 Calibration Film Exposure .....	15
2.2.5 Film Scanning Procedures.....	17
2.2.6 Film Testing .....	20
2.2.6.1 Scanner Constancy .....	20
2.2.6.2 Film-to-Film Variation.....	20
2.2.6.3 Batch-to-Batch Variation .....	20
2.2.6.4 Film Orientation Effects.....	21
2.2.6.5 Scanner Light Effect.....	22
2.2.6.6 Scanner Uniformity .....	22
2.2.6.7 Measurement Noise.....	23
2.3 Results .....	23
2.3.1 Scanner Constancy .....	23
2.3.2 Film-to-Film Variation.....	24
2.3.3 Batch-to-Batch Variation .....	26
2.3.4 Film Orientation Effects.....	28
2.3.5 Scanner Light Effect.....	29
2.3.6 Scanner Uniformity .....	31
2.3.7 Measurement Noise.....	34

2.4	Conclusions .....	35
2.5	References .....	37
3	Aim 2: Measure, Compare, and Evaluate the Coil Localization Accuracy of 4DCT and ExacTrac Gating for Respiratory Motion Amplitudes Greater than 5 mm over a Typical Respiratory Period. ....	39
3.1	Introduction .....	39
3.1.1	The Quasar Respiratory Phantom.....	39
3.1.2	Implanted Markers .....	40
3.1.3	4DCT Acquisition .....	41
3.1.4	ExacTrac System.....	43
3.2	Methods and Materials .....	49
3.2.1	The Quasar Motion Phantom .....	50
3.2.2	Implanted Markers .....	51
3.2.3	Phantom Motion Criteria.....	51
3.2.4	4DCT Methods.....	53
3.2.5	4DCT Coil Motion Study .....	53
3.2.6	ExacTrac Coil Motion Study.....	54
3.3	Results .....	56
3.3.1	4DCT Coil Endpoint Selection Accuracy .....	56
3.3.2	ET Coil Endpoint Selection Accuracy .....	58
3.3.3	4DCT Coil Motion Distortion Results .....	60
3.3.4	Coil Localization Results .....	61
3.4	Conclusions .....	65
3.5	References .....	66
4	Aim 3: Measure the Spatial Distribution of Dose to a Moving Phantom Using a Variety of Gating Window Levels and Amplitudes for Sinusoidal Motion. ....	68
4.1	Introduction .....	68
4.2	Methods and Materials .....	68
4.2.1	Pinnacle Treatment Planning.....	68
4.2.2	Ion Chamber Measurements.....	71
4.2.3	Radiochromic Film Phantom Measurements .....	72
4.2.4	Film Analysis .....	76
4.2.5	Margin Expansion Measurements .....	81
4.2.6	Dose-Volume Calculation .....	82
4.3	Results .....	83
4.3.1	5 mm Motion Data .....	85
4.3.2	10 mm Motion Data .....	85
4.3.3	15 mm Motion Data .....	90
4.3.4	20 mm Motion Data .....	92
4.3.5	25 mm Motion Data .....	92
4.3.6	Margin Expansion Recommendation .....	97
4.3.7	Dose-Volume Calculation .....	102
4.4	Conclusions .....	105
4.5	References .....	106

5	Conclusions.....	107
5.1	Aim 1.....	107
5.2	Aim 2.....	108
5.3	Aim 3.....	109
5.4	Recommendations .....	110
5.5	Response to Hypothesis.....	110
5.6	Future Work .....	110
	Vita .....	112

## List of Tables

Table 2.1: Comparison of vendor-provided characteristics of the Epson vs. Vidar scanner.....	15
Table 2.2: Batch numbers for films compared in this study .....	21
Table 2.3: Film response and standard deviation of the film response over 10 repeated scans on a single calibration film.....	24
Table 2.4: Film-to-film variation in film response as measured with the Vidar scanner system .....	25
Table 2.5: Film-to-film variation in film response as measured with the Epson scanner system .....	25
Table 2.6: Comparison of calibrated films taken from three different batches. The average film response ( $\mu$ ) is listed with the percent difference of the film responses of batches 2 and 3 from batch 1. ....	27
Table 2.7: Measurement of the effect of film orientation during scanning .....	29
Table 2.8: Effect of the Vidar scanner light on EBT film for film irradiated on Day 0. On each day, the average film response over ten scans performed on that day is reported. ....	31
Table 2.9: Measurement of the noise from the Vidar and Epson scanner systems .....	34
Table 3.1: Reproducibility of 4DCT coil endpoint selection by user for full-exhale phase (all values in cm).....	57
Table 3.2: Reproducibility of 4DCT coil endpoint selection by user for mid-exhale phase (all values are in cm).....	57
Table 3.3: Repeat ET Gating imaging of the positions of a stationary coil midpoint to test a user's ability to repeatedly identify the coil endpoints. Listed are the ExacTrac coordinates of the coil midpoint as calculated from the user-selected coil endpoints.....	59
Table 3.4: Repeat ET imaging of a coil undergoing 25mm sinusoidal motion at 50% amplitude. All values in mm.....	59
Table 3.5: Errors in 4DCT detected coil length over all phases for selected motion amplitudes. All values in mm. ....	60
Table 3.6 a-e: Comparison of 4DCT vs. ET Gating coil localization.....	63
Table 3.7a-e: Comparison of errors of the 4DCT vs. ET Gating system. The largest observed errors are highlighted for each data set.....	64
Table 4.1: The most likely direction of tumor motion from full-inhale to full-exhale taken from Chi, et al. ....	73



Table 4.2: Measured profile shifts on the superior and inferior side of the 5 mm motion profiles at 95% and 20% relative dose levels. ....	86
Table 4.3: Measured profile shifts on the superior and inferior side of the 10 mm motion profiles at 95% and 20% relative dose levels. ....	88
Table 4.4: Measured profile shifts on the superior and inferior side of the 15 mm motion profiles at 95% and 20% relative dose levels. ....	91
Table 4.5: Measured profile shifts on the superior and inferior side of the 20 mm motion profiles at 95% and 20% relative dose levels. ....	93
Table 4.6: Measured profile shifts on the superior and inferior side of the 25 mm motion profiles at 95% and 20% relative dose levels. ....	95
Table 4.7: Amount of overexpansion (in mm) beyond the static profile when expanding by the residual motion for the 20 mm motion plan delivered with 10, 20, 30 and 100% gating windows. ....	99
Table 4.8: Summary of the recommended internal margin expansion based on the size of the 95% under-dose on the inferior side of the gated profile. Gating windows which have a recommended internal margin expansion less than 3 mm for each target motion observed are marked in light green. Gating windows which have a recommended margin larger than 3 mm are marked in light red. ....	101
Table 4.9: Difference of recommended margin based on the 95% dose profile shift and the residual motion. ....	102
Table 4.10: Calculated dose volume data for a 30% gated delivery expanded to cover the CTV. ....	103
Table 4.11: Calculated dose volume data for a motion-encompassed (100% window level) delivery (20 mm) expanded to cover the CTV. ....	104
Table 4.12: Calculated dose volume data for a static phantom delivery. ....	104

## List of Figures

Figure 1.1: ICRU guidelines for delineating volumes for radiotherapy .....	4
Figure 1.2: Respiratory motion example diagram showing a respiration trace of the patient's external anterior-posterior motion and a sample gating sequence centered at the full-exhalation phase.....	6
Figure 2.1: Radiochromic EBT film irradiated under MBPCC calibration conditions showing the nine dose regions and corresponding doses measured for film analysis .....	16
Figure 2.2: Hurter-Driffield curve for the five calibration films scanned with the Vidar system .....	26
Figure 2.3: HD Curve for three batches of film as measured using the Vidar scanner. ....	28
Figure 2.4: Vertical profiles of a blank film as measured by the Vidar and Epson scanner systems.....	33
Figure 2.5: Horizontal profiles of a blank film as measured by the Vidar and Epson scanner systems.....	33
Figure 3.1: The Quasar Respiratory Motion phantom on the Novalis treatment couch and five reflective BrainLab bodymarkers used by the ExacTrac system to monitor the external chest wall/platform motion .....	40
Figure 3.2: Varian RPM system 4DCT infrared camera mounted at base of CT couch (left) and the Quasar respiratory phantom affixed with the RPM marker box (blue circle) as seen from the camera's point of view (right) .....	42
Figure 3.3: Conceptual picture of the ExacTrac kV orthogonal x-rays (courtesy of BrainLab).....	44
Figure 3.4: Picture of the ExacTrac amorphous silicon image detector mounted to the ceiling.....	44
Figure 3.5: Picture of covered kV x-ray housing panel in floor (left) and with cover removed (right) .....	45
Figure 3.6: The infrared camera system mounted in the Novalis room. The red circles indicate the infrared cameras used for monitoring the external BrainLab bodymarkers. The blue circle identifies as an optical-light camera for visual monitoring. ....	47
Figure 3.7: The ET Reference Star (circled in red) is shown mounted over a phantom on the Novalis treatment couch.....	47
Figure 3.8: Comparison of the DRR from the 4DCT (left) and a corresponding kV x-ray image from ExacTrac. The orange cross in the left image represents the planning isocenter. When the user identifies the location of the coil in the DRR and ExacTrac	

images, the system calculates the location of the planning isocenter to the machine isocenter .....	48
Figure 3.9: An example of the Visicoil inserted into the Quasar moving canister for imaging purposes. ....	51
Figure 3.10: MBPCC Respiratory period histogram from 34 patients scanned with clinical 4DCT protocol recorded by the Varian RPM system. ....	52
Figure 3.11: A pair of x-ray images obtained from the ExacTrac system used to identify the location of the implanted Visicoil. Coil is circled in red at the top left (left image) and top right (right image).....	55
Figure 4.1: Pinnacle TPS orthogonal views of the conformal radiotherapy plan delivered to Quasar phantom. The planning data set is the 50% phase (full-exhale). The top left view is an axial view, top right is sagittal, and the bottom left view is a coronal slice. All three views were through the CTV <sub>Plan</sub> isocenter. The bottom right view the nine beam arrangement placed around the CTV <sub>Plan</sub> isocenter. The canister/target motion is in the superior-inferior direction. ....	70
Figure 4.2: The Quasar phantom viewed from the gantry (left) and as viewed standing next to the foot of the couch (right). Labels denote the superior and inferior sides of the phantom.....	73
Figure 4.3: (a) Modification of the film insert canister for implanted coil (outlined in red) and (b) superior view of canister placement in Quasar phantom with coil (outlined in red) on anterior surface of the phantom's canister. ....	74
Figure 4.4: (a) Internal view of film canister with radiochromic EBT film in place and (b) sample film showing registration marks from Quasar film canister.....	75
Figure 4.5: The Vidar film guide used for scanning films irradiated in the Quasar film canister. ....	77
Figure 4.6: Gated delivery with 100% gating level and 20 mm target motion film (left) vs. static phantom plan delivery film (right) with black lines symbolizing the direction of target motion and analyzed profiles.....	78
Figure 4.7: RIT software horizontal profile analysis of 30% window level and 20 mm motion gated delivery (target) film registered to the (reference) alignment film. The target motion was perpendicular to the left profile and to the right in the right profile. ....	79
Figure 4.8: Example of 20 mm motion gated profile measurements in relation to static phantom irradiation. The gray arrow represents the direction of target motion from the reference gating level at full-exhale. Black horizontal lines demonstrate how the 100% gating window expands past the static phantom delivery profiles, while red lines indicate a contraction of the dose profile from the static delivery profile.....	81

Figure 4.9: Film measurements of three repeated stationary phantom plan delivery profiles. ....	84
Figure 4.10: 5 mm dose motion profiles for all measured gating windows. ....	86
Figure 4.11: Plot of 5 mm motion gated superior-side isodose shift. ....	87
Figure 4.12: Plot of 5 mm motion gated inferior-side profile shift. ....	87
Figure 4.13: 10 mm motion dose profiles for all measured gating windows. ....	88
Figure 4.14: Plot of 10 mm motion gated superior-side isodose shift. ....	89
Figure 4.15: Plot of 10 mm motion gated inferior-side isodose shift. ....	89
Figure 4.16: 15 mm motion dose profiles for all measured gating windows. ....	90
Figure 4.17: Plot of 15 mm motion gated superior-side profile shift. ....	91
Figure 4.18: Plot of 15 mm motion-gated inferior-side profile shift. ....	92
Figure 4.19: 20 mm motion dose profiles for all measured gating windows. ....	93
Figure 4.20: Plot of 20 mm motion gated superior-side profile shift. ....	94
Figure 4.21: Plot of 20 mm motion gated inferior-side profile shift. ....	94
Figure 4.22: 25 mm motion profiles for all measured gating windows. ....	95
Figure 4.23: Plot of 25 mm motion gated superior-side profile shift. ....	96
Figure 4.24: Plot of 25 mm motion gated inferior-side isodose shift. ....	96
Figure 4.25: 20 mm amplitude motion gated deliveries expanded in the direction of target motion by the residual motion during the gating window. ....	98
Figure 4.26: 95% dose shift expansion profiles for 30, 50, 80 & 100% gating windows compared to the static phantom delivery. ....	101
Figure 4.27: Calculated volumes receiving a range of dose levels shown for a comparison of a 30% window gated plan, motion-encompassed (100% gating window) plan, and a stationary phantom delivery with no expansion. ....	105

## **Abstract**

The purpose of this project was to investigate the interplay between gating window characteristics and target margin required to compensate for residual motion during the gating window. This project investigated the accuracy of ExacTrac and 4DCT imaging localizing an implanted coil at various phases of respiration. Radiochromic film measured delivered dose patterns for selected gating intervals over a variety of respiratory patterns. In order to establish accurate dosimetry, this project implemented and tested an EBT radiochromic film dosimetry system.

Film testing showed that the performance of a medical grade Vidar Dosimetry Pro radiographic film scanner and an Epson V700 Photo flatbed scanner were very similar. Both scanners showed nearly the same performance in terms of measurement repeatability, noise, vertical and horizontal uniformity over a range of doses from 11.5-511.9 cGy. The Vidar was selected for these studies due to clinical availability.

Even at the greatest coil velocities observed, ExacTrac coil localization agreed with calculated coil motion to within 0.8 mm. 4DCT showed errors up to 5.5 mm resolving coil position during large respiratory-induced velocities. 4DCT accurately measured the coil length within 1 mm of actual coil length at end expiration/inhalation. 4DCT can provide an accurate representation of the phantom at end-respiration for treatment planning purposes, and ExacTrac can accurately localize the coil to determine target motion in all phases

For patient treatments it is suggested that target margins should be set using the residual motion during gating. For patients without implanted coils, the residual motion can be computed based on the target motion measured from 4DCT and the size of the gating window. For patients with implanted coils, the ExacTrac system can be used to directly measure residual tumor motion during gating.

The hypothesis of this work was that gated delivery combined with 4DCT could limit internal margins to less than 3 mm while maintaining 95% prescription dose coverage of moving targets. The hypothesis was found to be true for gating windows of 10% and 20% for target motions up to 25 mm and was true with gating windows up to 50% for smaller motions (5 & 10 mm).

# **1 Introduction**

## **1.1 Statement of the Problem**

The American Cancer Society reports that in 2007, lung cancer accounted for 31% of all cancer deaths in the United States and an estimated 213,380 new cases were diagnosed (1.1). This report also states that the five-year survival rate for all stages of lung cancer combined is 16%. However, there is clinical evidence that tumor control can be increased with an increase in treatment dose (1.2, 1.3, 1.4). One limiting factor in dose escalation is the risk of lung complications, which has been shown to correlate with the average lung dose and similar surrogates such as the volume of lung receiving  $\geq 20$  Gy (1.5, 1.6). The need for normal tissue sparing becomes even more important when concurrent chemotherapy is used. Thus, there is clinical evidence that technologies that increase dose to the tumor while sparing healthy tissues will improve the clinical outcomes for lung cancer patients.

The goal of modern radiation therapy is to maximize the absorbed dose in a target volume while minimizing dose to normal, healthy tissue. Three-dimensional conformal radiation therapy (3DCRT) uses imaging studies such as computed tomography (CT) to define target volumes in three dimensions, and 3D treatment planning software to generate plans that conform the dose distribution as closely as possible to those volumes. Reductions in complications that result from irradiating healthy tissue can be achieved by limiting the dose delivered to normal tissue. With a relative reduction of dose to normal tissues comes the ability to escalate the dose delivered to the target to increase tumor control probability while maintaining acceptable levels of normal tissue complications.

One major limitation of conventional 3DCRT is the lack of compensation for respiration-induced organ motion. Current standard radiation therapy techniques treat a volume that encompasses the tumor at all potential positions within the respiratory cycle. While this

technique covers the tumor volume, it also dramatically increases the dose to surrounding normal tissues. Respiratory motion can potentially reduce the target localization accuracy of therapy delivered to tumor sites in the thorax and abdomen. Accurate knowledge of the tumor motion and adjustment of the radiation delivery to compensate for such motion will permit a reduction in the target volume and, therefore, doses to surrounding normal tissues.

Potential techniques for incorporating intrafractional respiratory motion into treatment planning/delivery include breath-hold, respiration-gating, and tumor-tracking. Breath-hold techniques either actively or passively suspend the patient's respiration for short intervals or deliver treatment during these intervals (1.7). However, patients with lung tumors may have compromised breathing capacity and performing stable, extended breath holds for treatment may not be feasible. Respiration-gating techniques periodically turn on the treatment beam when the patient's breathing parameters fall within a predefined range (such as near full-inhale or full-exhale phase of respiration) (1.8). Tumor-tracking, or four dimensional, methods propose to actively track the tumor with the radiation beam as the tumor moves during the respiratory cycle (1.9). Tumor-tracking four-dimensional techniques greatly increase the complexity of the treatment delivery. All of these techniques require some form of observation of the respiratory motion. Current measurement techniques include infrared external marker tracking, spirometry, strain gauges, video visual tracking, and fluoroscopic tracking of implanted fiducial markers.

The motion of a fiducial marker implanted into or near a tumor gives the best information about the motion of the tumor. However, the process of percutaneous or endoscopic implantation of fiducial markers is an invasive procedure, and fluoroscopic imaging of an implanted marker results in additional dose from the x-ray tube. External motion sensors are safer and non-invasive, but do not correlate as well to internal tumor motions. For patient use, constant



fluoroscopic tracking of an implanted fiducial is replaced by visually tracking the motion of external markers, whose motion has been correlated to that of the implanted fiducials.

This project investigated a free-breathing method of respiration gating using a combination of implanted fiducial markers for patient alignment and infrared monitoring of external infrared markers for gating the radiation treatment beam. By considering respiratory motion and utilizing techniques to deliver radiation via respiratory gating during free breathing, the traditional margins for intrafractional tumor motion can be reduced. This project investigated the margin reductions possible for a respiratory-gated treatment using a motion phantom as a surrogate for actual patient investigations.

## **1.2. Definition of Volumes**

International Commission on Radiation Units and Measurements (ICRU) Report 50 (1.10) sets guidelines for volumes in radiotherapy by defining the gross tumor volume (GTV), clinical target volume (CTV), and planning target volume (PTV). The GTV is defined as the gross palpable or visible/demonstrable extent and location of the malignant growth. The CTV is defined as a tissue volume that contains a GTV and/or subclinical microscopic malignant disease. The CTV is based on purely anatomic-topographic and biological considerations without regard to the movement of the tissues/patient or technical factors. The PTV is a geometrical region defined to select appropriate beam sizes and beam arrangements, taking into consideration the net effect of all the possible geometrical variations and uncertainties, in order to ensure that the prescribed dose is actually absorbed in the CTV where diseased tissue resides (1.11). Figure 1.1 shows the evolution of the target volume from the early ICRU 29 report to the most recent ICRU 62 report.

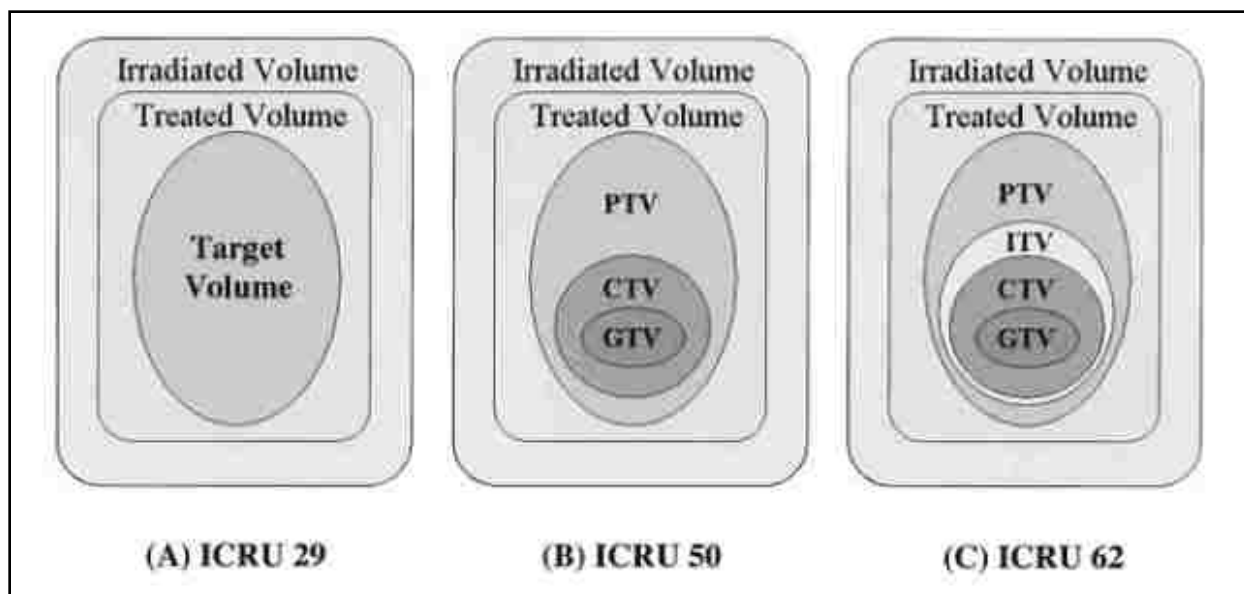


Figure 1.1: ICRU guidelines for delineating volumes for radiotherapy

ICRU Report 62 adds the concept of internal target volume (ITV), which is a region that encompasses the CTV with an internal margin (IM). The IM accounts for all movements and variations in the CTV size and shape both during treatment (intrafraction) and between treatment sessions (interfraction). The ITV is expanded into the PTV by adding a setup margin (SM) about the ITV. The SM takes into account uncertainties in the reproducibility of patient setup inherent in every treatment session. The major component of the ITV formation is the intrafractional movement of the CTV due to respiratory motion (1.11).

The region between the CTV and PTV includes normal, healthy tissue that receives the therapeutic dose. As previously stated, the volume of healthy tissue receiving high doses can be closely related to the incidence of adverse side effects, especially in the lungs (1.5). Thus, any reduction of the internal margin and setup margin used to construct the PTV would reduce dose received by normal tissue.

### **1.3 Definition of Respiration Characteristics**

In order to understand terms used throughout this paper, Figure 1.2 illustrates a sample breathing trace. A patient's chest wall fall and rises over the course of a respiratory period, as shown in the y-axis of Figure 1.2. Each respiratory period can be divided into percentages ranging from 0 to 99 percent. Full-inhale is considered to be occurring at 0% phase, while full-exhale is defined as 50% phase. This nomenclature is adopted from the CT scanner 4D reconstruction program. Full-exhale is considered to be 0% of the chest wall amplitude, as this is when the chest wall is at that lowest position in the anterior-posterior (AP) direction for a patient laying supine on the treatment table. Full-inhale would then be the 100% amplitude position of the chest well or patient external motion. For a sinusoidal curve, the phase and amplitude are mathematically correlated, but actual patient motion is not sinusoidal.

Figure 1.2 also shows a pink region of amplitude above a line called the reference gating level. The reference gating level is selected to be the level about which a window of either phase or amplitude is added, which is called the gating window. The gating window is shown as the red line on either side of the reference gating level. For the purposes of the work, the "gating window level" will refer to the amplitude level signified by the red line. At this location in time, the respiratory trace moves out of the gating window, and the treatment beam is gated off. The gating window is expressed as a percentage of the respiratory amplitude from full-exhale (0% amplitude) to the gating window level. By increasing the gating window level, the treatment beam is enabled for a larger portion of the respiratory cycle.

When the patient's respiratory motion is observed to be within the gating window, the beam is enabled for treatment. The bottom section of Figure 1.2 illustrates the beam enabling as the respiratory motion of the patient moves into the sample gating window. When the patient moves out of the gating window, the beam is disabled and radiation delivery is stopped. The

gating window can be increased or decreased, as indicated by the vertical arrows on Figure 1.2, which affects the amount of beam-on time in each respiratory period.

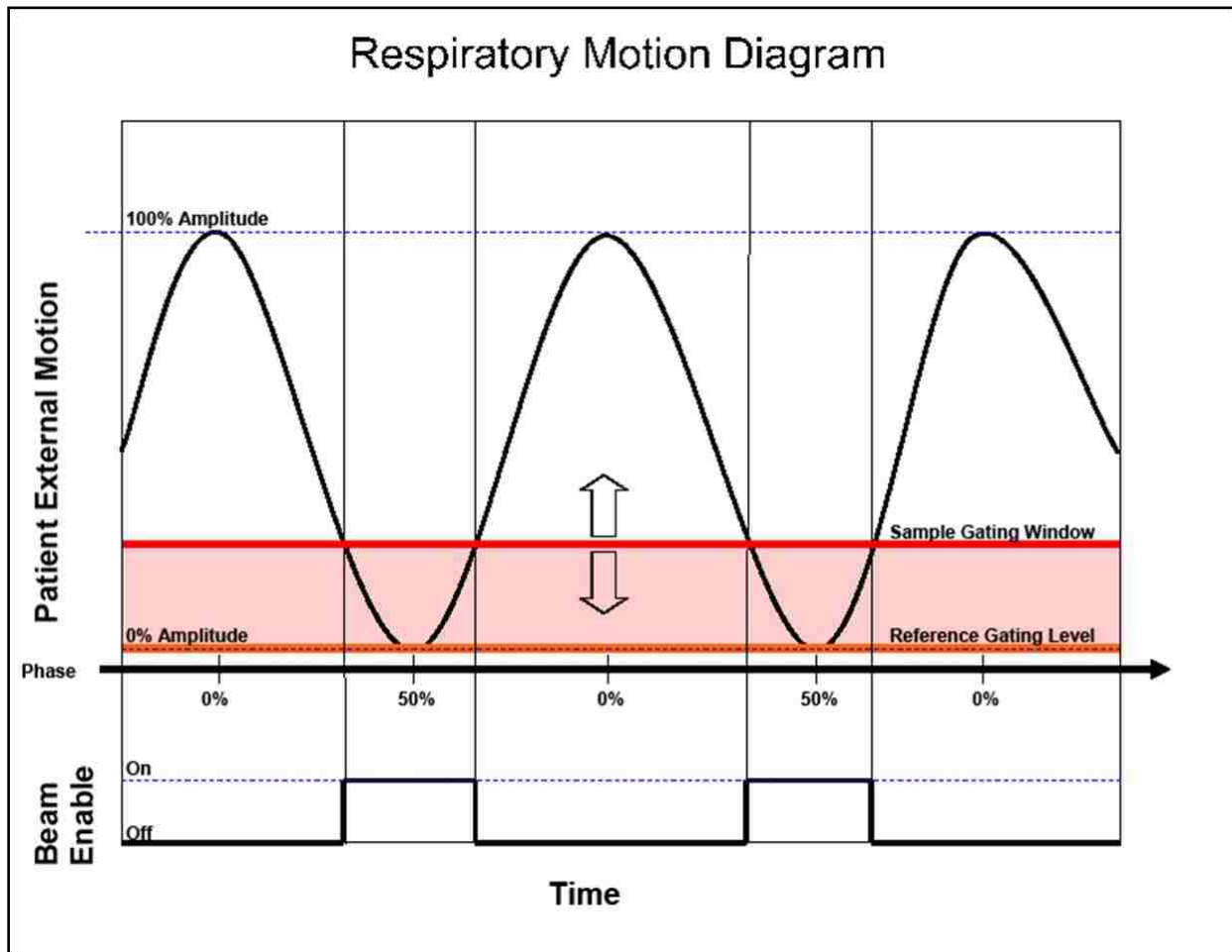


Figure 1.2: Respiratory motion example diagram showing a respiration trace of the patient's external anterior-posterior motion and a sample gating sequence centered at the full-exhalation phase.

As the gating window is decreased, the amount of time the beam is enabled is also decreased, the overall treatment time is increased, and the motion of the patient during the window is decreased. The target motion during the gating window is referred to as residual motion. When selecting the size of the gating window, the amount of residual motion and overall gated-treatment time must be considered

## **1.4 Respiratory Gating and Internal Margins**

In order to achieve the greatest benefit from respiratory gating, one must understand the relationship between ITV expansion margin (IM) and the width of the gating window used for treatment. In order to define an appropriate respiratory margin for a given tumor and treatment, the residual motion must be known for a given gating window and target motion amplitude. AAPM Task Group 76 (1.12) recommends the following steps for treatment planning:

1. Account for the distortion of the planning CT due to respiratory motion induced artifacts.
2. Correlate the internal tumor displacement and phase relationship with respect to with external markers used in gating.
3. Quantify the variation between respiratory cycles both intrafractionally and interfractionally and the resulting error in treatment margins.
4. If a patient-specific tumor-motion measurement is made, the information should be used in the CTV-to-PTV margin used for treatment planning.

This project addressed recommendation #1 by imaging a moving implanted metallic coil and comparing the image measurements to known coil length and position. Recommendation #2 was addressed by using an implanted marker as a surrogate for the internal patient motion to measure the internal tumor motion. Imaging an implanted fiducial allows the internal target motion to be correlated to observed external marker motion. Because this project used a respiratory phantom with predictable and stable motion, recommendation #3 was not considered. Recommendation #4 is prescriptive in recommending that patient-specific motion information be used in treatment planning. This project gives recommendations on how to incorporate such motion information.

## **1.5 Hypothesis**

The goal of this project was to investigate the relationship between internal target motion, gating window widths, and internal margin required to accurately cover the CTV. These

relationships were studied using radiochromic EBT film, four-dimensional (time-resolved) computer tomography (4DCT) and ExacTrac (BrainLab, Munich, Germany) x-ray imaging system.

The hypothesis of this work was that Novalis ExacTrac gating, combined with 4DCT, can be used to limit internal margin expansions to less than 3 mm while maintaining 95% prescription dose coverage of the CTV for tumors that are influenced by large (>5 mm) respiratory induced motions.

The specific aims were:

- Aim 1: Develop an accurate and efficient dosimetry system to measure dose distributions of respiratory-gated radiation therapy treatments using radiochromic film.
- Aim 2: Measure, compare, and evaluate the coil localization accuracy of 4DCT and ExacTrac gating for respiratory motion amplitudes greater than 5 mm over a typical respiratory period.
- Aim 3: Measure the spatial distribution of dose to a moving phantom using a variety of gating window levels and amplitudes for sinusoidal respiratory motion.

## 1.6 References

- 1.1 American Cancer Society, "Cancer Facts and Figures 2007," Available: <http://www.cancer.org/downloads/STT/caff2007PWSecured.pdf>
- 1.2 M. Machtay. "Higher BED is associated with improved local-regional control and survival for NSCLC treated with chemotherapy: An RTOG analysis." *Int. J. Radiat. Oncol. Biol. Phys.* 63(2), S66 (2005).
- 1.3 M. K. Martel, R. K. Ten Haken, M. B. Hazuka, M. L. Kessler, M. Strawderman, A. T. Turrisi, T. S. Lawrence, B. A. Fraas, and A. S. Lichter, "Estimation of tumor control probability model parameters from 3-D dose distributions of non-small cell lung cancer patients." *Lung Cancer* 24(1): 31-37 (1999).
- 1.4 J. M. Robertson, R. K. Ten Haken, M. B. Hazuka, A. T. Turrisi, M. K. Martel, A. T. Pu, J. F. Littles, F. J. Martinez, I. R. Francis, L. E. Quint, and A. S. Lichter, "Dose escalation

- for non-small cell lung cancer using conformal radiation therapy,” *Int. J. Radiat. Oncol. Biol. Phys.* 37, 1079-1085 (1997).
- 1.5 S. L. Kwa, J. V. Lebesque, J. C. Theuws, L. B. Marks, G. Bentel, D. Oetzel, U. Spahn, M. V. Graham, R. E. Drzymala, J. A. Purdy, A. S. Lichter, M. K. Martel, and R. K. Ten Haken, “Radiation pneumonitis as a function of mean lung dose: an analysis of pooled data of 540 patients.” *Int. J. Radiat. Oncol. Biol. Phys.* 42(1), 1-9 (1998).
  - 1.6 Y. J. Seppenwoolde, J. V. Lebesque, K. de Jaeger, J. S. A. Belderbos, L. J. Boersma, C. Schilstra, G. T. Henning, J. A. Hayman, M. K. Martel, and R. K. Ten Haken, “Comparing different NTCP models that predict the incidence of radiation pneumonitis,” *Int. J. Radiat. Biol. Phys.* 55(3), 724-735 (2003).
  - 1.7 K.E. Rosenweig, J. Hanley, D. Mah, G. Mageras, M. Hunt, S. Toner, C. Burman, C. C. Ling, B. Mychalczak, Z. Fuks, and S. A. Leibel., “The deep inspiration breath-hold technique in the treatment of inoperable non-small cell lung cancer,” *Int. J. Radiat. Oncol., Biol., Phys.* 48, 81-87 (2000).
  - 1.8 H.D. Kubo and B.C. Hill, “Respiration gated radiotherapy treatment: A technical study,” *Phys. Med. Biol.* 41, 83-91 (1996).
  - 1.9 C. Ozhasoglu and M.J. Murphy, “Issues in respiratory motion compensation during external-beam radiotherapy,” *Int. J. Radiat. Oncol., Biol., Phys.* 52, 1389-1399 (2002).
  - 1.10 International Commission on Radiation Units and Measurements (ICRU). Report #50, Prescribing, Recording and Reporting Photon Beam Therapy. Bethesda, MD: ICRU 1993.
  - 1.11 International Commission on Radiation Units and Measurements (ICRU). Report #62. Prescribing, Recording and Reporting Photon Beam Therapy (Supplement to ICRU Report 50). Bethesda, MD: ICRU 1999.
  - 1.12 P.J. Keall, G. S. Mageras, J. M. Butler, R. S. Emery, K. M. Forster, S. B. Jiang, J. M. Kapatoes, D. A. Low, M. J. Murphy, B. R. Murray, C. R. Ramsey, M. B. Van Herk, S. S. Vedam, J. W. Wong, E. Yorke, “The management of respiratory motion in radiation oncology report of AAPM Task Group 76,” *Med. Phys.* 33, 3874-3900 (2006).

## **2 Aim 1: Develop an Accurate and Efficient Dosimetry System to Measure Distributions of Respiratory-Gated Radiation Therapy Treatments Using Radiochromic Film**

### **2.1 Introduction**

Film dosimetry can be performed with both radiographic and radiochromic film. Silver-halide based radiographic films, such as Kodak EDR and Kodak XV-2, have been the standard of clinical dosimetry in the past. Limitations include a high effective Z due to the silver in the film, creating a non-water equivalent dosimetric response. Also, radiographic films require processing facilities (dark room, processor, etc.) and the chemical development process can influence the results of the film measurements. The EDR film has a dynamic range of 10-500 cGy, which includes doses used for a typical patient fraction. XV-2 film, on the other hand, saturates at a lower dose near 80 cGy, and is therefore more suitable for quality assurance measurements.

Radiochromic film has significant advantages over radiographic film for x-ray dosimetry. Radiochromic film is self-processing, removing the need for dedicated dark room facilities and expensive wet chemical processing. However, early types of radiochromic film, such as MD-55 had low sensitivity (0-10,000 cGy) and so were suitable to measure only high doses (2.1, 2.2). The newest radiochromic film, GafChromic EBT (International Specialty Products, Wayne, NJ), is been designed for the measurement of absorbed dose in the range of 1-800 cGy (2.3). Radiochromic EBT has also been reported to have minimal photon energy dependence (2.4) and radiochromic film in general has been shown to be nearly tissue equivalent (2.5).

Radiochromic film has been shown to be an excellent tool for two-dimensional film dosimetry provided that some precautions and corrections are taken into account (2.6, 2.7, 2.8, 2.9, 2.10). High spatial resolution, minimal energy dependence, and near tissue equivalence



make radiochromic film desirable for our film studies. When using a phantom that requires cut film pieces, the ability to handle film in room light greatly simplifies the setup process (EBT film is relatively insensitive to fluorescent room lighting). Because EBT is self-developing, the measurement variations due to wet chemical processing of radiographic film are eliminated (2.11). This may allow for a single film calibration to represent the response of an entire batch of film, further simplifying film dosimetry.

We investigated the film characteristics and processes necessary to measure dose distributions for gated radiation delivery to a moving respiratory phantom. Medical grade scanners are typically used in clinical settings to analyze radiographic films. However, radiochromic film users have suggested that a flatbed document scanner may be sufficient, and even possibly superior, to traditional medical scanners (2.12, 2.13). In this aim we also compared a widely-used medical grade scanner to a flatbed document scanner suggested in recent literature in order to decide which scanning system to use for this project, and for clinical use at Mary Bird Perkins Cancer Center.

## **2.2 Methods and Materials**

Conflicting literature reports necessitated our own investigations into the properties of each scanner when scanning EBT film (2.14, 2.15). The performance of each scanner was measured in terms of reproducibility, uniformity, noise, and accuracy. Reproducible methods of scanning were developed and verified for each scanner.

### **2.2.1 Epson V700 Scanner System**

An Epson Perfection V700 Photo scanner (Seiko Epson Corporation, Nagano, Japan) was purchased for testing as our radiochromic EBT film scanner at MBPCC. It is a flatbed document scanner designed for high quality photographic scanning. It can operate in both transmission and reflective mode, but for the purposes of medical film scanning, it should be used in the

transmission mode. The maximum scan area of the Epson scanner is 8.5" x 11.7". The standard radiochromic film is 8x10", but larger film sizes are available which would exceed the maximum scanner area. Due to the lack of FDA constraints in the manufacturing process of flatbed scanners like the Epson, scanner manufacturers can substitute components and firmware without notice, possibly resulting in significant changes in scanner characteristics (2.14).

Both systems have supported commercial software that interfaces with the scanner, but MBPCC does not possess software for analyzing films scanned with the Epson.

This scanner is considered to be a replacement for the discontinued Epson Expression 1680 scanner which is widely used for radiochromic film dosimetry, as reported in several publications (2.6, 2.7, 2.8, 2.9, 2.10, 2.12, 2.13). To date, there are no reports on the use of the Epson V700 scanner. The Epson 1680 and V700 both utilize a fluorescent light source with a broadband emission spectrum and a linear charge coupled device (CCD) array detector. The Epson manufacturer reports the scanner resolution can be set to upwards of 12800 dots per inch (dpi), or ~0.00198 mm/pixel; however the resolution for all Epson scans was set at 150 dpi to balance resolution with increasing file size and scan time. The Epson scanners can save scanned image data in a 48-bit red-green-blue (RGB) tagged image file format (TIFF). The ability to extract and analyze the red channel data is an attractive feature of Epson flatbed scanners for radiochromic film dosimetry.

The Epson has capabilities for repeat imaging, red channel extraction, and background subtraction. Repeat imaging capability refers to the ability to repeatedly image the same film without moving it. With repeat imaging capability, the user can take multiple scans of a film and average them in order to reduce noise or uncertainty. Red channel background subtraction refers to the fact that with a 48-bit RGB image, the 16-bit red channel can be extracted for dosimetric purposes. Red channel extraction is useful for radiochromic film because it responds most to red

light, so that the red component of the scanned image has the greatest sensitivity. The flexibility of the TIFF format allows the user to manipulate the image more than the Vidar .RV4 format, such as scan averaging or pre-irradiation film background subtraction. Background subtraction means that the film can be accurately placed in the scanner bed, allowing for a pre-irradiation scan of the film to be subtracted from the experimental film after exposure using programs such as MATLAB (Math Works, Natick, NJ). Background subtraction is also dependent on the positioning reproducibility of the film achievable in the Epson system.

Initial testing showed the response of the Epson V700 scanner at MBPCC to be similar to an Epson 1680 at the LSU Medical Physics office. Currently, the EBT manufacturer includes a pamphlet in each box of film that recommends using the Epson 10000XL scanner system, but this scanner cost is very high (~\$2500). This high cost of the 10000XL scanner offsets the cost efficiency of using a flatbed scanner if a user already owns a medical grade film scanner, such as the Vidar. The Epson V700 scanner currently retails for less than \$1000. Thus, we elected to evaluate the Epson V700 as the best flatbed candidate against the Vidar for analyzing radiochromic film at MBPCC.

### **2.2.2 Vidar Scanner System**

The VXR Dosimetry PRO Advantage Film Digitizer (Vidar Systems Corporation, Hendon, Virginia) has a fluorescent white light source with a spectral distribution ranging from 250 to 750 nm and a linear CCD system for measuring transmitted light. Radiographic film is currently being scanned at MBPCC using this scanner with the RIT V5.0 (Radiological Imaging Technology, Colorado Springs, CO) software. The RIT software was used to analyze all of the Vidar scans for this project. The Vidar scanner always produced a 16-bit grayscale image using the entire spectrum of the scanner light source.

The digitizer can scan films up to 14" wide. This larger scan area would be useful for scanning an entire sheet of larger EBT film (14x17"), now available from the film's manufacturer. Film is transported past the measurement apparatus, as opposed to the Epson scanner where the light source/detector system moves across a stationary film. The Vidar system can measure optical density in the range of 0.01 to 3.65. The physical resolution of Vidar scans can vary from 0.356 x 0.356 mm to 0.089 x 0.089 mm.

The FDA-approved Vidar scanner currently uses the established commercial RIT V5.0 software available at MBPCC and the scanner characteristics are well documented. RIT V5.0 currently has a feature that attempts to correct for film non-uniformity using a scanned blank film, but we are currently not using this module because it is not readily apparent what modifications this software module would perform on the film scans. This scanner currently costs over \$10,000 including the necessary software for analysis.

When the film moves through the Vidar scanner, the physical movement of the film does not allow for exact duplication of the film to the previous position in the scanner. The Vidar scanner can be left on at all times, and includes a forced self-calibrating routine to ensure that the light source is sufficiently warmed up and stable.

### **2.2.3 Summary of Scanner Characteristics**

Table 2.1 shows a side-by-side comparison of the physical characteristics of the two scanner systems. Some advantages of the Epson scanner include the flexibility of file formats, the ability to use the red light channel to analyze the film, and the fact the film remains stationary on the scanner bed. Some advantages of the Vidar scanner include the built-in self-calibration, the larger scan area, and the availability of the RIT software in the clinic to analyze the Vidar-produced images.

Table 2.1: Comparison of vendor-provided characteristics of the Epson vs. Vidar scanner.

Scanner Characteristics	Epson V700 red channel	Vidar Dosimetry Pro
Resolution	508 - 1.98 um	356, 178, 89 um
Repeat imaging capability	yes	no
Red channel extraction capability	yes	no
Background subtraction capability	yes	no
FDA approved	no	yes
Med. physics technical support	no	yes
Commercial software capability	FilmQA, not in clinic	RIT V5.0, currently in clinic
Output file format	.TIF .JPG .BMP	.RV4 (RIT proprietary)
Light source	fluorescent white light	fluorescent white light
Detector array	linear CCD array	linear CCD array
Maximum scan area	8.5 x 11.7 "	14 x 17 "
Color depth	48 bit RGB	16 bit grayscale
Relative scanner cost	< \$1000	> \$10,000

Of particular interest is that the Vidar scanner currently costs over \$10,000, while the Epson scanner retails for less than a tenth of this (<\$1000).

## 2.2.4 Calibration Film Exposure

Numerous films were exposed to a range of doses from 11.5 to 512 cGy on a Varian 6/18 EX linear accelerator using a clinical 8-box radiographic film calibration setup technique. The calibration technique involves placing the film perpendicular to a 6 megavoltage (MV) beam at 100 SAD and 10 cm depth in solid water, with 10 cm of solid water below the film for sufficient backscatter conditions. Radiation is delivered using predefined multileaf collimator sequence that creates two columns of four separate rows of  $3 \times 3 \text{ cm}^2$  regions on the film. Each region received a different known dose. An ion chamber was previously used to measure the dose under each of the eight dosed regions on the film as well as a low dose region receiving indirect scatter contribution in the center of the film. These measurements of each region account for not only dose directly from delivered to each field, but leakage and scatter contributions from the other

seven delivered fields. Figure 2.1 shows the eight visible dose regions labeled 1-8, and a region of scattered low dose labeled as region 0. Dose regions 0-8, as indicated in Figure 2.1, receive doses of 11.5, 67.3, 137.8, 199.8, 259.2, 320.4, 392.6, 453.8, and 511.9 cGy, respectively. These doses cover most of the manufacturer-specified dynamic range for EBT film (0-800 cGy).

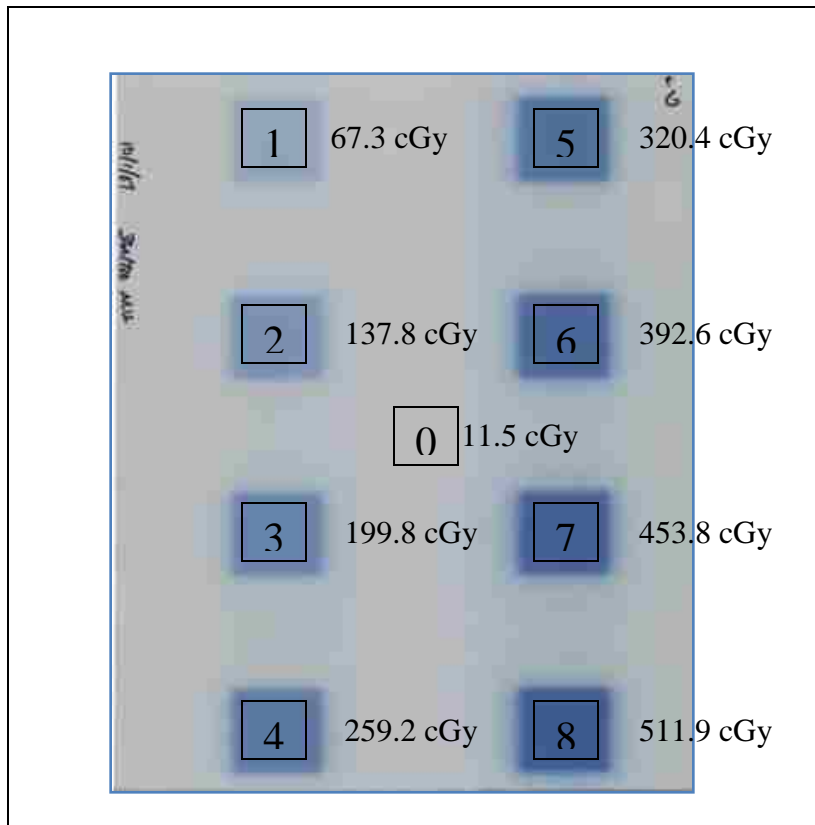


Figure 2.1: Radiochromic EBT film irradiated under MBPCC calibration conditions showing the nine dose regions and corresponding doses measured for film analysis

All films were irradiated under the same conditions, at the same time, and unless otherwise specified, were from the same batch of film. Film exposure to room lighting was minimized and relatively equal, thus neglected when comparing similar films. The films were labeled and stored back in the film box for a period of 24 hours before scanning. This was to ensure that all polymer changes within the film due to the irradiation had completed. All films were stored together before and after irradiation to keep all film thermal history the same. No special consideration was given to regulating the film environment beyond the room temperature

and humidity conditions maintained by the facility's air conditioner. Films were stored in opaque film protectors before and after readout to minimize room light exposure.

### **2.2.5 Film Scanning Procedures**

The experiment films (8x10") were smaller than the maximum scanner bed size for both scanners. Therefore, experiment films were placed in the center region of each scanner for scanning. Pixel size in both scanners was chosen to be similar: 178  $\mu\text{m}$  for the Vidar scanner and 169  $\mu\text{m}$  (150 dots/inch) for the Epson scanner. This was done in order to balance a small pixel size with an increasing scan time and overall size of the image files generated. Unless otherwise stated, all films were scanned 24 hours post-irradiation to allow sufficient time for all self-development to complete within the experimental film.

For all Vidar scans, the self-calibration process was completed at the start of every film scanning session. The Vidar light source requires the user to allow the light source to "warm-up" and stabilize before scanning any films. Also, before every film is scanned, the Vidar automatically repeats a shorter routine to ensure the light source is still sufficiently stable. After calibration completed, the film was placed by hand into the center of the scanner, and the RIT software completed the scanning process. The RIT software was used for all subsequent film analysis and measurement of Vidar-produced images.

The EBT manufacturer recommends and will provide a clear polyester sleeve to secure film pieces for transport through the Vidar system. We found these sleeves to be unacceptable due to circular Newton ring artifacts caused by reflecting interference at different thicknesses of the air layer between the sleeve surfaces. These rings were clearly visible to the eye and on the resulting scans in the Vidar scanner. We consider the use of such sleeves unsuitable for our film dosimetry system.

For all Epson scans, only the red channel data was analyzed for this project. All image enhancement features were turned off in the EpsonScan program. No background subtraction, uniformity correction, or other processing was used on these scans unless noted. The Epson scanner always created a 48-bit RGB file, but the 16-bit red channel was extracted and analyzed for all reported measurements. The ImageJ software package was used to analyze the pixel values for the 16-bit red channel images. ImageJ is a java-based image processing software program developed at the National Institutes of Health. ImageJ is capable of analyzing TIFF format images, and measuring mean and standard deviation values for selected regions of interest. ImageJ does not have the capabilities to perform film calibration or treatment planning import and comparison. Because no calibrated commercial step wedge is known to exist for radiochromic film, no conversions from pixel value (PV) to optical density were performed unless noted. All data are reported in terms of pixel values.

Paelinck, et al. recommends not using the first three scans from the 1680 model Epson scanner when beginning a new film scanning session (2.9). Epson scanners have no built in procedure to “warm-up” the light source before scanning. The user must simply acquire numerous unusable scans until the user feels the light source is sufficiently stable. For the purposes of this study, at least 30 minutes were allowed after turning on the Epson scanner before scanning, and at least 10 Epson scans without film in the scanner were taken before data collection. Paelinck reported on the warm-up characteristics, or short term drift, of the 1680 model Epson (2.9) but no one has reported on the short or long term stability of the V700 Epson model. The user cannot be sure when or if the Epson scanner light source is sufficiently stabilized, which is a major disadvantage with the Epson scanner.

For the Epson scanner, RIT 4.4 software was used during initial analysis of the TIFF images. A MATLAB routine was written in order to convert the Epson produced TIFF images



into a DICOM (Digital Imaging and Communications in Medicine) format which was acceptable for importation in the RIT software. In RIT V5.0, however, the software would no longer allow the DICOM files created from TIFF images to be calibrated, effectively prohibiting the use of the RIT software with the Epson scanner with this approach.

For reporting results, sometimes presenting the data in terms of optical density instead of PV may be more informative for the observer. It should be noted that the pixel value is actually the value returned by the scanner system's analog-to-digital converter, and is generally system dependant. Typically for radiographic film dosimetry in the RIT software system, a calibrated optical density step wedge is scanned into the system. The RIT software finds a mean PV over the central portions of each step and creates a curve relating the pixel value to optical density. This correlation is used to convert the pixel values measured by the RIT software system into optical density values. Because no calibrated step wedge exists for radiochromic film, measured pixel values cannot be converted into optical density. Therefore, when optical density is reported, it was calculated manually using the definition of optical density:

$$OD = -\log_{10} \left( \frac{I}{I_0} \right), \quad \text{eq. 1}$$

where  $I$  equals the intensity of the transmitted light beam, and  $I_0$  is the intensity of the incident light beam on the film. For a 16-bit gray-scale or red-scale image,  $I$  was taken as the reported pixel value and the incident beam,  $I_0$ , was assumed to have a pixel value of 65535 ( $2^{16}-1$ ). Unfortunately, the accuracies of the Epson and Vidar scanners cannot be assessed by comparison to a manual point densitometer because the light spectra are different and the transmission of radiochromic film is wavelength dependant. To avoid confusions about optical density, most data are presented in terms of unique raw pixel values that are reported by the scanner systems.

## **2.2.6 Film Testing**

Unless otherwise noted, for each film test, we report the mean of the central 1.5x1.5 cm<sup>2</sup> area of each dose region as the “film response” of that particular dose for the nine dose levels observed on each experimental film. For the region of low dose, a 1.5x1.5 cm<sup>2</sup> area was chosen in the center of the film to represent region 0. Regions 1-8 are as defined in Figure 2.1. All films were scanned 24 hours post-irradiation.

### **2.2.6.1 Scanner Constancy**

To test the repeatability of each scanner, a single calibration film was scanned 10 times in rapid succession on each system. The RIT software was used to measure the film response of each dose region. For all nine dose regions, the film response was calculated and the standard deviation of the ten scan measurements was computed.

### **2.2.6.2 Film-to-Film Variation**

To test film-to-film variations, five calibration films from a single batch were irradiated at the same time. Each film was assumed to have received the same dose in each of the corresponding dose regions. The average film response for each dose level was recorded for each film and standard deviation of the five measured film responses was calculated.

### **2.2.6.3 Batch-to-Batch Variation**

Manufacturing conditions may vary among different production batches. In order to study this effect, one film from each of three separate batches of EBT film was selected. The three films were irradiated under calibration conditions and analyzed at the same time. Table 2.2 provides the basic information on the three batches tested. Batches 1 and 2 came from film batches purchased and stored at MBPCC; batch 3 is a sheet from a batch at Louisiana State University used in previous film studies.

Each film was scanned three times in the Vidar system. The three measured film responses for each film were averaged for each of the nine dose regions. The percent differences of the film response of Batches 2 and 3 from Batch 1 were calculated. Batch 1 was selected as the comparison standard because the all other tests in this aim use films taken from Batch 1.

Table 2.2: Batch numbers for films compared in this study

Name	Lot	Exp Date	Location
Batch 1	35322-0021	Nov-07	MBPCC
Batch 2	36348-041	Dec-08	MBPCC
Batch 3	35322-0041	Nov-07	LSU

#### **2.2.6.4 Film Orientation Effects**

The optical density of EBT film may change substantially depending on the polarization of the analyzing scanner light relative to the orientation of the film. This effect has been attributed to the alignment of the radiochromic film polymer chains which form after irradiation (2.16). Zeidan et al. reported measurement of an effect with a 90 degree rotation of the film in the scanner where the measured optical density dropped by 50% for 50 cGy to 25% for 200 cGy (2.17). Because the scanners have different light source spectra and detector properties, it was necessary to measure film orientation effect in both scanning system

A single calibration film was scanned in both portrait and landscape orientations. The film responses of all dose regions in the portrait orientation were compared to the landscape orientation in terms of percent difference. Portrait orientation was defined as the long axis of the film being perpendicular to the linear scanner light source; landscape orientation was defined as the long axis of the film being parallel to the linear scanner light source. Although film scanning at any orientation is possible in the Epson scanner, only portrait and landscape orientations are

possible with the Vidar scanner. The bank of film rollers in the Vidar scanner require a straight, even film edge to grab.

### **2.2.6.5 Scanner Light Effect**

EBT film has a small response to light and, therefore, the scanning process itself could affect results. To characterize the effect, a calibration film was scanned 30 times and the change in film response measured after every 10 scans over a span of several days. Only the Vidar scanner was used for this test, but the Epson scanner has a similar fluorescent white light source, which would affect the film in the same manner.

The film was scanned 10 times in rapid succession 24 hours after irradiation. The initial average of the 10 measured film responses gave a baseline reading for each dose. After another period of 24 hours, the film was scanned again 10 times again in rapid succession. This measurement of the film response compared to the baseline response measured the effect of the light from the initial 10 scans. This process was repeated a third time after another 24 hours to quantify the effect of the 20 previous scans. Finally, after another 24 hour period, the film was scanned again to measure the effect of 30 scans of the film. Waiting 24 hours between scanning sessions allows any scanner light effects from the previous day to completely polymerize within the film.

### **2.2.6.6 Scanner Uniformity**

A single piece of blank, non-irradiated radiochromic film was scanned in portrait orientation using both systems. Horizontal and vertical profiles were taken through center of each film, and the resulting PV profiles were compared. This test assumed that the film was of uniform optical density over the entire sheet. The horizontal profile is indicative of how uniform the detectors are across the width of the central scanner bed in each system. The vertical profile is recorded by the same light/detector segment as the scanner operates. Thus, a vertical profile of

a blank film should show how uniform the same detector segment is over the course of scanning a film.

### **2.2.6.7 Measurement Noise**

A single calibration film was used to test the overall measurement noise. The central 1.5x1.5 cm<sup>2</sup> portion of each dose region was assumed to be uniform. The measurement noise of the scanner/film system was taken to be the measured standard deviation of all the pixels in the central 1.5x1.5 cm<sup>2</sup> of each dose region. This measurement was performed for both scanners. This noise measurement includes scanner, film, and irradiation variations, and gives an estimate of the precision of the film response measurement.

## **2.3 Results**

### **2.3.1 Scanner Constancy**

The scanner constancy results of both systems are shown in Table 2.3. The table shows the average of the ten measured film responses ( $\mu$ ), the standard deviation ( $\sigma$ ) of the measurements, and the standard deviation expressed as a percentage of the film response ( $\mu/\sigma$ ) at each dose. Each scanning system reported a different film response due to hardware differences and, especially, the use of the Epson red channel versus the white light of the Vidar scanner.

The largest standard deviation of the film response can be seen as 0.22% at 199.8 cGy for the Vidar, and 0.17% at 67.3 and 137.8 cGy for the Epson scanner. The maximum standard deviation for either scanner was less than 0.22% of the measured film response over the dose range tested.

Table 2.3: Film response and standard deviation of the film response over 10 repeated scans on a single calibration film.

Dose (cGy)	Vidar			Epson		
	$\mu$	$\sigma$	$\sigma/\mu$	$\mu$	$\sigma$	$\sigma/\mu$
11.5	45280	46	0.10%	47581	61	0.13%
67.3	36053	73	0.20%	37783	65	0.17%
137.8	29710	52	0.17%	31297	53	0.17%
199.8	25592	56	0.22%	27132	41	0.15%
259.2	22726	42	0.18%	24350	29	0.12%
320.4	20783	31	0.15%	21762	35	0.16%
392.6	18883	20	0.11%	19918	27	0.14%
453.8	17433	20	0.11%	18562	23	0.12%
511.9	16276	18	0.11%	17490	13	0.07%

### 2.3.2 Film-to-Film Variation

Table 2.4 shows the film response pixel values for all dose regions as measured with the Vidar system for the five different films scanned. The film responses of all dose regions are reported for all five films labeled A-E. The average film response of all five experiment films ( $\mu$ ), standard deviation ( $\sigma$ ) and standard deviation reported as a percentage of the mean ( $\sigma/\mu$ ) are also reported in Table 2.4. No more than 0.39% standard deviation is observed between different films of the same batch irradiated under identical conditions and given identical time (24 hours) to self-develop.

Table 2.5 shows data for the same five films as analyzed in the Epson scanner. The maximum standard deviation is 0.51%, only slightly larger than for the Vidar scanner. Figure 2.2 shows a Hurter–Driffield (HD) curve showing the optical density calculated using equation 1 from the pixel values as given in Table 2.4. Since HD curves are commonly displayed in terms of optical density, not pixel value, the calculated optical density was used for plotting purposes. For all five films, the resulting HD curves are nearly indistinguishable from each other.

Table 2.4: Film-to-film variation in film response as measured with the Vidar scanner system

Dose (cGy)	Film A	Film B	Film C	Film D	Film E		$\mu$	$\sigma$	$\sigma/\mu$
11.5	45690	45665	45719	45625	45760		45692	51	0.11%
67.3	36777	36582	36758	36448	36736		36660	142	0.39%
137.8	30272	30263	30282	30182	30387		30277	73	0.24%
199.8	26124	26098	26171	26067	26157		26123	42	0.16%
259.2	23340	23267	23267	23176	23276		23265	58	0.25%
320.4	21155	21078	21038	21096	21056		21085	45	0.21%
392.6	19095	19136	19125	19185	19288		19166	76	0.39%
453.8	17699	17718	17723	17674	17733		17709	23	0.13%
511.9	16470	16490	16469	16535	16526		16498	31	0.19%

Table 2.5: Film-to-film variation in film response as measured with the Epson scanner system

Dose (cGy)	Film A	Film B	Film C	Film D	Film E		$\mu$	$\sigma$	$\sigma/\mu$
11.5	46471	46538	46438	46320	46472		46448	80	0.17%
67.3	37482	37667	37696	37444	37279		37514	172	0.46%
137.8	31224	31238	31342	31217	31126		31229	77	0.25%
199.8	26962	26958	27146	27008	26970		27009	79	0.29%
259.2	24120	24171	24283	24245	24208		24205	63	0.26%
320.4	21870	22053	22014	21967	21780		21937	111	0.51%
392.6	20157	20162	20209	20121	19987		20127	84	0.42%
453.8	18562	18722	18636	18582	18494		18599	85	0.46%
511.9	17489	17532	17493	17424	17344		17456	74	0.42%

Thus, films from the same batch, given the same irradiation conditions and allowed to self-develop by the same amount of time, will be very uniform in response. From this we conclude that a single calibration would be sufficient for each batch of film.

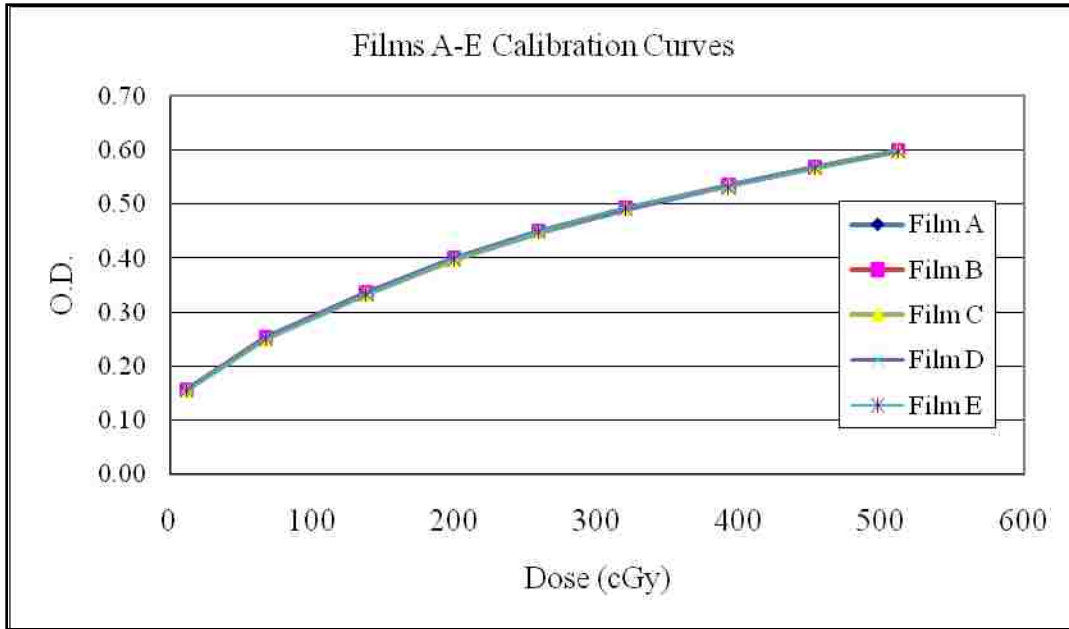


Figure 2.2: Hurter-Driffield curve for the five calibration films scanned with the Vidar system

### 2.3.3 Batch-to-Batch Variation

For an inter-comparison between batches of radiochromic film, calibration films from each of three different batches were analyzed using the Vidar scanner. Table 2.6 shows the average film response ( $\mu$ ) for three repeated scans of each dose region on the film from each batch.

Film from Batch 1 was used for all the other testing in this aim. The last two columns of Table 2.6 show the percent difference for each dose region of batches 2 and 3 with respect to batch 1. The equation used to calculate the percent difference from batch 1 was:

$$\%Diff = \frac{\mu_x - \mu_1}{\mu_1} \times 100, \quad \text{eq. 2}$$

where  $\mu_1$  and  $\mu_x$  are the mean values of corresponding dose regions between batches 1 ( $\mu_1$ ) and batches 2 or 3 ( $\mu_x$ ). The batch-to-batch variation is large when compared to the film-to-film variation. Batch 2 differs from batch 1 by up to -9.30% in the high dose regions, while batch 3 differs by 8.52% in the region of the film receiving low dose. In the regions 1-8, batch 3 differs



from batch 1 by less than 3.45% percent difference for all dose regions. Figure 2.3 shows the HD curve from the three films from different batches. The optical density values were calculated using equation 1.

Table 2.6: Comparison of calibrated films taken from three different batches. The average film response ( $\mu$ ) is listed with the percent difference of the film responses of batches 2 and 3 from batch 1.

Dose (cGy)	Batch 1 $\mu$	Batch 2 $\mu$	Batch 3 $\mu$		Batch 2 % Diff	Batch 3 % Diff
11.5	45336	48214	49198		6.35%	8.52%
67.3	36637	36817	37901		0.49%	3.45%
137.8	30218	29514	30866		-2.33%	2.15%
199.8	25959	24886	26084		-4.13%	0.48%
259.2	23105	21870	23276		-5.34%	0.74%
320.4	21234	19671	20872		-7.36%	-1.71%
392.6	19239	17795	18936		-7.51%	-1.57%
453.8	17560	16314	17294		-7.10%	-1.51%
511.9	16653	15105	16195		-9.30%	-2.75%

On each box of EBT film, a nine digit number is posted to identify the lot and batch number of the film within the box. It is interesting to note from Table 2.2 that the batches 1 and 3 have the same first five digits, and the same expiration date. Batch 2 was manufactured some time after batches 1 and 3 as evidenced by the expiration date on the box. For film batches 1 and 3, which were manufactured near the same time, the percent difference is less than the difference between batches 1 and 2. This would suggest that either slight changes to the manufacturing process or the overall age of the film have changed the film's response slightly.

For films from different batches, up to a 9.3% difference in film response was observed. While this is not as pronounced of an effect as previously observed in radiographic films, it is still a considerable difference. Therefore, care must be taken to generate a calibration for each batch of film.

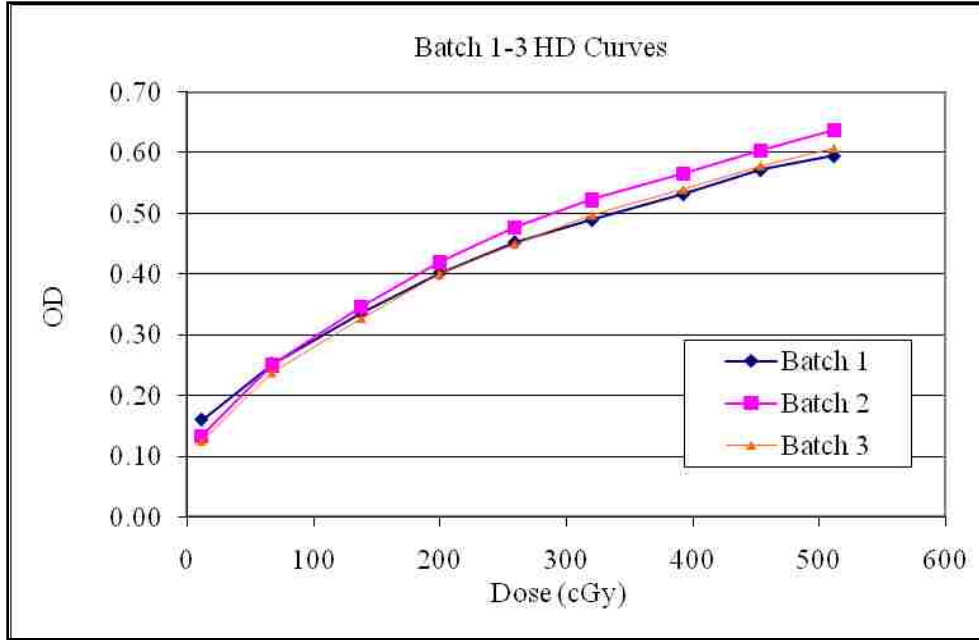


Figure 2.3: HD Curve for three batches of film as measured using the Vidar scanner.

### 2.3.4 Film Orientation Effects

The effects of film orientation are reported in Table 2.7. For each scanner system, the first column shows the measured PVs of a single film scanned in portrait orientation. The measured values in landscape orientation are given in the second column labeled “Land”. The third column shows the percent difference between the portrait and landscape orientations. The percent difference of the two orientations was defined as

$$\%Diff = \frac{\mu_{Land} - \mu_{Port}}{\mu_{Port}} \times 100, \quad \text{eq. 3}$$

where  $\mu_{Land}$  is the mean PV in the landscape orientation while  $\mu_{Port}$  is the mean PV in the portrait orientation.

As seen in the table, the measured pixel values showed a change between the two film orientations. The Epson scanner showed a larger variation between the two orientations, registering 17.40% percent difference between the portrait and landscape mean pixel values at

the 453.8 cGy dose region. The largest deviation observed by the Vidar was 5.27% at 392.6 cGy dose region. Thus, the Epson is more susceptible than the Vidar to orientation effects. The larger susceptibility of the Epson to orientation effects may be due to the Epson scanner's use of red light, which coincides with the absorption peak of the film, as opposed to the Vidar which observes the entire spectra emitted by the scanner lamp.

Table 2.7: Measurement of the effect of film orientation during scanning

Dose (cGy)	Epson				Vidar		
	Portrait	Land	% Diff		Portrait	Land	% Diff
11.5	47344	50132	5.89%		48052	48584	1.11%
67.3	37382	40716	8.92%		36617	36868	0.69%
137.8	30976	34501	11.38%		29265	29968	2.40%
199.8	26620	30092	13.04%		24422	25157	3.01%
259.2	23945	27012	12.81%		21526	22068	2.52%
320.4	21504	24901	15.80%		19419	20243	4.24%
392.6	19660	22966	16.82%		17431	18350	5.27%
453.8	18057	21199	17.40%		15820	16595	4.90%
511.9	17027	19806	16.32%		14638	15283	4.41%

### 2.3.5 Scanner Light Effect

Table 2.8 shows the effect of scanning on film darkening. It was assumed that over the 10 repeated scans on each day, that the scanner and room light would have negligible effects during the scans. Therefore, each day the scanner is measuring the additional darkening effects of the ten scans from the previous day. When the film was kept away from room light for 24 hours then rescanned, any additional darkening of the film is attributed to the effects of the room/scanner light on the film.

The original irradiation was considered to occur on Day 0. After 24 hours, on Day 1, all of the self development is complete from the initial irradiation. The Day 1 column shows the mean film response of ten scans that measured the effect of the radiation alone. On Day 2, the 10 scans measured the additional darkening caused by the scanning on Day 1. Similarly, each successive day's reading measured the increased darkening caused by the scanning of the previous day. For the scans conducted on Day 4, the measured pixel values included 30 scans worth of light exposure from the scanner. The percentage change from the original value, or percent error, of each day as compared to the original readings on Day 1 is given in the three columns to the right. The equation used to calculate the percent error is:

$$\%Error = \frac{\mu_i - \mu_{initial}}{\mu_{initial}} \times 100 \quad , \quad \text{eq. 4}$$

where  $\mu_i$  is the average film response after a certain number of scans, and  $\mu_{initial}$  is the baseline film response.

Exposure to light should some cause film darkening and corresponding decreases in pixel value. Thus, the percent differences should be negative, as seen in Table 2.8, and also become larger in magnitude as the light from more scans affect the film. On average over all nine dose regions, a 1.56% decrease in pixel value was measured after 30 scans are taken of the film. The largest decrease in pixel value after 30 scans was less than 2% observed at 259.2 cGy. For clinical measurements, the film would be scanned no more than a few times. Thus, the effect of the scanner light should be a negligible. Even if a single film was used for calibration per batch, there are only 25 sheet of film per box. Thus, even if a single calibration film were used per box, and scanned each time a single film measurement was taken every day, the calibration film would be scanned 24 times at most, introducing an error due to additional scanner light <2%.

Table 2.8: Effect of the Vidar scanner light on EBT film for film irradiated on Day 0. On each day, the average film response over ten scans performed on that day is reported.

Dose (cGy)	Day 1	Day 2	Day 3	Day 4	% Change from Initial		
	Initial	10 Scans	20 Scans	30 Scans	10 Scans	20 Scans	30 Scans
11.5	45538	45279	45232	45235	-0.57%	-0.67%	-0.67%
67.3	36301	36052	35972	35880	-0.69%	-0.91%	-1.16%
137.8	30020	29710	29573	29561	-1.03%	-1.49%	-1.53%
199.8	25878	25591	25520	25460	-1.11%	-1.38%	-1.61%
259.2	23030	22726	22633	22578	-1.32%	-1.73%	-1.96%
320.4	20990	20783	20671	20615	-0.99%	-1.52%	-1.79%
392.6	19080	18882	18789	18741	-1.03%	-1.52%	-1.78%
453.8	17613	17433	17357	17327	-1.03%	-1.46%	-1.62%
511.9	16446	16275	16182	16135	-1.04%	-1.61%	-1.89%

The average darkening of a film exposed to 10 scans was less than one percent. Therefore, on average, for the first ten scans of a film each scan should only decrease the pixel value by 0.1% if given 24 hours to complete any further self-development. This measurement shows that the effect of the scanner light is negligible; even when the film is given ample time to further self-develop from any scanner light exposure and limited handling in room light during scans.

### 2.3.6 Scanner Uniformity

Uniformity of scanner response was measured by scanning the central axis of a blank film along both the vertical and horizontal axes. Figures 2.4 and 2.5 show profile comparisons of the Vidar and Epson scanners in the vertical and horizontal axes, respectively.

As seen in the figures, the Vidar scanner registers higher pixel values for the blank film than does the Epson scanner. This is due to differences in the analog-to-digital converters, and the fact the Epson profile is taken from the red light channel. Important non-uniformities are seen in the first and last inch of the Vidar vertical profile that are not observed in the Epson vertical scan. This can be attributed to the Vidar film transport mechanism, as reported by Wilcox, et al. (2.15).

Ignoring the leading and trailing inches of film, the Vidar vertical profile has a mean value of 50653 and a standard deviation of 174 or 0.34% of the mean. The Epson scanner vertical profile has a mean value of 49060 and a standard deviation of 160, or 0.33% of the mean. Thus, when the roller artifacts are ignored in the Vidar system, both systems have similar horizontal response uniformity. In the horizontal direction, no artifacts are noted in either system. The Vidar scanner registers a mean value of 50464 and a standard deviation of 353, or 0.70% of the mean, over the horizontal profile of the blank film. The Epson scanner gives a similar result with a mean of 48646 and a standard deviation of 298, or 0.61% of the mean. Both systems show small systematic errors that probably account for the increased non-uniformity.

In the vertical profile, the measurement shows the response of a single detector along the film. If we consider this detector to be stable, the variation measured in the vertical profile gives us a measure of the variation across the film. This variation is smaller than the variation as seen over the horizontal profile which shows the response of all the detectors across the film at a single instance of time. The horizontal profile gives us a measure of the variation across not only the film, but across all of the detectors that the film passed through during measurement.

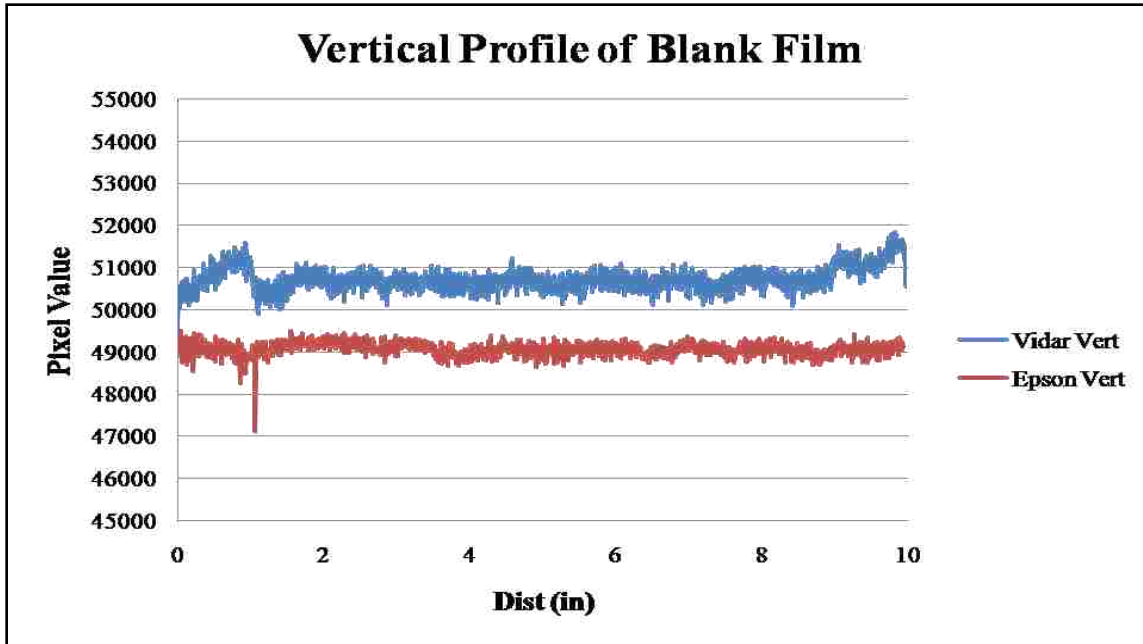


Figure 2.4: Vertical profiles of a blank film as measured by the Vidar and Epson scanner systems

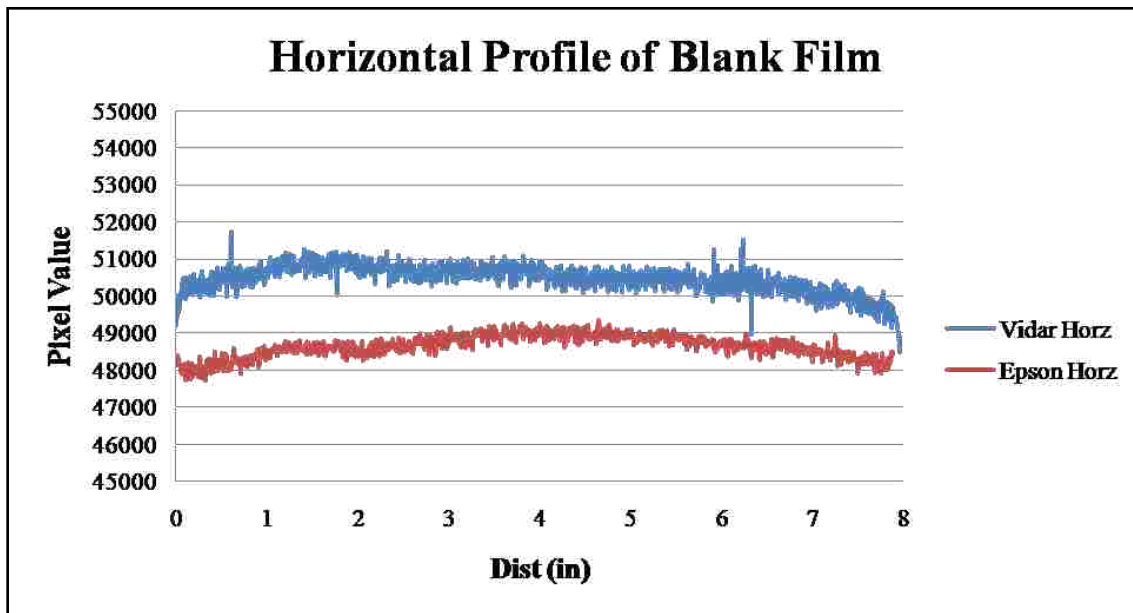


Figure 2.5: Horizontal profiles of a blank film as measured by the Vidar and Epson scanner systems

### 2.3.7 Measurement Noise

Table 2.9 shows, for each scanner, the measurement noise at each dose level. For each dose level, transmission values were measured at all pixels in a 1.5x1.5 cm<sup>2</sup> area. The standard deviation of those values is interpreted to be the overall measurement noise, and includes scanner, film, and irradiation variations. The table gives the mean pixel value (PV), the standard deviation ( $\sigma$ ), and standard deviation expressed as a percentage of the mean ( $\sigma$ /PV).

The absolute standard deviation at each dose was approximately the same for both systems, but because the Vidar registered slightly lower mean pixel values, the standard deviation expressed as a percent of the mean was slightly higher. For both systems, the measurement noise was less than 1.15% for all doses. The largest observed noise occurred in both systems at the 453 cGy dose level. For doses less than 400 cGy, scanner noise was less than one percent in both scanner systems.

Table 2.9: Measurement of the noise from the Vidar and Epson scanner systems

Dose (cGy)	Vidar			Epson		
	PV	$\sigma$	$\sigma$ /PV	PV	$\sigma$	$\sigma$ /PV
0	50709	157	0.31%	49061	145	0.29%
11.5	47800	187	0.39%	46838	172	0.37%
67.3	36742	186	0.51%	37469	166	0.44%
137.8	29435	180	0.61%	30932	151	0.49%
199.8	24895	175	0.70%	26646	180	0.68%
259.2	21995	171	0.78%	23875	172	0.72%
320.4	19727	168	0.85%	21819	141	0.65%
392.6	17658	170	0.96%	20106	161	0.80%
453.8	16192	185	1.14%	18655	186	1.00%
511.9	15074	163	1.08%	17550	144	0.82%



## 2.4 Conclusions

We found that film-to-film variations within a single batch were very low with standard deviations of less than 0.39% for the Vidar scanner and less than 0.51% for the Epson scanner. However, batch-to-batch variations were significant, up to 9.3% in one case. We conclude that for a single batch of film, a single calibration is adequate for all experimental films in that batch, but that each batch of film must be individually calibrated.

Both scanners showed nearly the same performance in terms of measurement repeatability, uniformity, and overall measurement noise. Surprisingly, the cheaper, commercial flat bed scanner even slightly out-performed the medical grade Vidar scanner in a few categories such as scanner noise and scanner uniformity.

If the film has been cut into squares, the original orientation of the film from which the piece was cut should be clearly marked. It is clear that in it is not acceptable to rotate the film by 90 degrees in either scanner. Care must be taken when using radiochromic film in order to maintain the same orientation of the film from calibration to analysis of experimental films. For all subsequent film studies in this project, the portrait orientation of the film was maintained in all scans.

No corrections were used to correct for any non-uniformity in the detector response. This is due to the low variation of  $<0.70\%$  SD from the mean over the horizontal profile of a blank film as measured in both scanners.

One significant problem in using the Epson scanner is the lack of support by the Epson Corporation for radiochromic film applications. Users of Epson scanners for medical film analysis constitute a tiny fraction of Epson scanner users, and that is unlikely to change in the future. Customer support, technical specifications, and software development are all geared to the majority of the scanner's customer base. With the large customer base of Epson scanner not

conducting medical grade film scanning, it is unlikely that much help in these categories will be provided to the tiny segment of users interested in radiochromic film scanning. Due to the lack of FDA constraints in the manufacturing process, graphic arts scanner manufacturers like Epson can substitute components and firmware without notice, possibly resulting in significant differences between scanners (2.14)

Another significant issue with the Epson scanner is the fact that no self-calibration of light source or warm-up tests exist. The user must simply take many preview scans with the Epson scanner and assume the scanner is adequately warmed up. In this testing, no drift was observed during repeated film scanning, but there is no guarantee that the Epson light source is sufficiently warmed up.

In contrast to the Epson scanner, the Vidar scanner has a forced self-calibrating routine at the start of every run of film analysis. However, an issue did arise with the Vidar scanner on the leading and trailing edges of a scanned film. This has been reported by Wilcox, et al. (2.15) and was confirmed in our testing. The leading and trailing edge of the film profile perpendicular to the light source measured a 3% increase in pixel value. The artifacts can be avoided by ignoring the leading and trailing inch of film in a film scan, or by affixing a piece of film to a larger film guide for transportation through the Vidar scanner.

The EBT manufacturer's recommendation of using polyester sleeves with the Vidar scanner was determined to be unacceptable due to artifacts caused by light reflection from the air between the sleeves. For all subsequent film investigations with cut film pieces, film was scanned by affixing the cut film edges to a larger film for transportation past the measurement slit in the Vidar scanner, and will be discussed later.

Both film scanners proved to be reliable and accurate for film dosimetry. Therefore, the next concern was the ease of use and availability of the scanner software. In our clinic, the lack

of commercially available software for using the Epson scanner was a major disadvantage. The commercial RIT 5.0 software system has proven useful enough to warrant not developing or purchasing software for using the Epson scanner. If an institution already has a working Vidar scanner system, we cannot see a clear reason to adopt an Epson scanner system. If an institution does not have a medical film scanner similar to Vidar, the Epson scanner may be an attractive alternate to purchasing a Vidar scanner just for radiochromic film dosimetry.

Because our clinic already has the RIT software on site and all the tools and experience necessary for film dosimetry with the Vidar scanner, it was decided to use the Vidar system and RIT software for the remainder of this research.

## 2.5 References

- 2.1. N. Klassen, L. Zwan, and J. Cygler, "GafChromic MD-55: Investigated as a precision dosimeter," *Med. Phys.* 24, 1924-1934 (1997).
- 2.2. G. R. Gluckman and L. E. Reinstein, "Comparison of three high resolution digitizers for radiochromic film dosimetry," *Med. Phys* 29, 1839-1846 (2002).
- 2.3. International Speciality Products (ISP), "GAFCHROMIC EBT white paper," <https://www.ispcorp.com/products/dosimetry/index.html>
- 2.4. S. T. Chiu-Tsao, Y. Ho, R. Schankar, L. Wang, and L. B. Harrison, "Energy dependence of response of new high sensitivity radiochromic films for megavoltage and kilovoltage radiation energies," *Med. Phys.* 32, 3350-3354 (2005).
- 2.5. A. Niroomand-Rad, C. R. Blackwell, B. M. Coursey, K. P. Gall, J. M. Galvin, W. L. McLaughlin, A. S. Meigooni, R. Nath, J. E. Rodger, and C. G. Soares, "Radiochromic film dosimetry: Recommendations of AAPM Radiation Therapy Committee Task Group 55," *Med. Phys.* 25, 2093-2115 (1998).
- 2.6. L. J. Van Battum, D. Hoffmans, H. Piersma, and S. Heukelom, "Accurate dosimetry with GafChromic EBT film of a 6MV photon beam in water: What level is achievable?" *Med. Phys.* 35, 704-716 (2008).
- 2.7. C. Fiandra, U. Ricardi, R. Ragona, S. Anglesio, F. R. Giglioli, E. Calamia, and F. Lucio., "Clinical use of EBT model GafChromic film in radiotherapy," *Med. Phys.*, 33, 4314-4319 (2006).

- 2.8. B. D. Lynch, J. Kozelka, M. K. Ranade, J. G. Li, W. E. Simon, and J. F. Dempsey., “Important considerations for radiochromic film dosimetry with flatbed CCD scanners and EBT GAFCHROMIC film” *Med. Phys.* 33, 4551-4556 (2006).
- 2.9. L. Paelinck, W. De Neve, and C. De Wagner, “Precautions and strategies in using a commercial flatbed scanner for radiochromic film dosimetry,” *Phys. Med. Biol.* 52, 213-242 (2007).
- 2.10. E. E. Wilcox, and G. M. Daskalov, “Evaluation of GAFCHROMIC EBT film for Cyberknife dosimetry,” *Med. Phys.* 34, 1967-1974 (2007).
- 2.11. S. Pai, I. J. Das, J. F. Dempsey, K. L. Lam, T. J. LoSasso, A. J. Olch, J. R. Palta, L. E. Reinstein, and E. Wilcox, “TG-69: Radiographic film for megavoltage beam dosimetry,” *Med. Phys.* 34, 2228-2258 (2007).
- 2.12. S. Devic, J. Seuntjens, G. Hegyi, E. B. Podgorsak, C. G. Soares, A. S. Kirov, I. Ali, J. F. Williamson, and A. Elizondo, “Dosimetric properties of improved GafChromic films for seven different digitizers,” *Med. Phys.* 31, 2392-2401 (2004).
- 2.13. S. Devic, J. Seuntjens, E. Sham, E.B. Podgorsak, C.R. Schmidlein, A.S. Lirov, and C.G. Soares, “Precise radiochromic film dosimetry using a flat-bed document scanner” *Med. Phys.* 32, 2245-2253 (2005).
- 2.14. D.M. Ritt, G.H. Pierce, M.L. Whitaker, R.S. Poling, “Repeatability and calibration results of GAFchromic EBT film with flatbed and medical scanners,” [http://radimage.org/downloads/repeatability\\_ebt.pdf](http://radimage.org/downloads/repeatability_ebt.pdf)
- 2.15. E. Wilcox, G. Daskalov and L. Nedialkova, “Comparison of the Epson 1680 flatbed and the Vidar VXR-16 Dosimetry PRO film scanners for use in IMRT dosimetry using Gafchromic and radiographic film,” *Med. Phys.*, 34, 41-48 (2007).
- 2.16. A. Rink, I. A. Vitkin, and D. A. Jaffray, “Characterization and real-time optical measurements of the ionizing radiation dose response for a new radiochromic medium,” *Med. Phys.* 32, 2510-2516 (2005).
- 2.17. O. A. Zeidan, S. A. L. Stephenson, S. L Meeks, T. H. Wagner, T. R. Willoughby, P. A. Kupelian, and K. M. Langen, “Characterization and use of EBT radiochromic film for IMRT dose verification,” *Med. Phys.* 33, 4064-4072 (2006).

### **3 Aim 2: Measure, Compare, and Evaluate the Coil Localization Accuracy of 4DCT and ExacTrac Gating for Respiratory Motion Amplitudes Greater than 5 mm over a Typical Respiratory Period.**

#### **3.1 Introduction**

This aim will track an implantable coil imbedded into the Quasar phantom to determine the coil localization accuracy of both the ExacTrac (ET) and the 4DCT system. The ability of each system to track the moving implanted fiducial provides data on how well each system can track a moving tumor. Should a coil be implanted into a patient, it is necessary to know the accuracy of each system to resolve and track the coil over all phases of respiration.

##### **3.1.1 The Quasar Respiratory Phantom**

The Quasar respiratory motion phantom (Modus Medical Devices, Ontario, Canada) is a device which simulates one-dimensional patient respiratory motion. A cylindrical canister moves horizontally in the superior-inferior direction to simulate internal lung motion, while a platform moves vertically (anterior-posterior) to simulate the patient's external chest wall motion. The phantom produces one-dimensional sinusoidal motion with the canister and platform driven by a rotating ovoid cam. The chest wall platform amplitude is fixed at 10 mm, while the canister amplitude can be manually adjusted from 0 to 50 mm motion amplitude. Figure 3.1 shows the Quasar phantom setup on the Novalis treatment table.

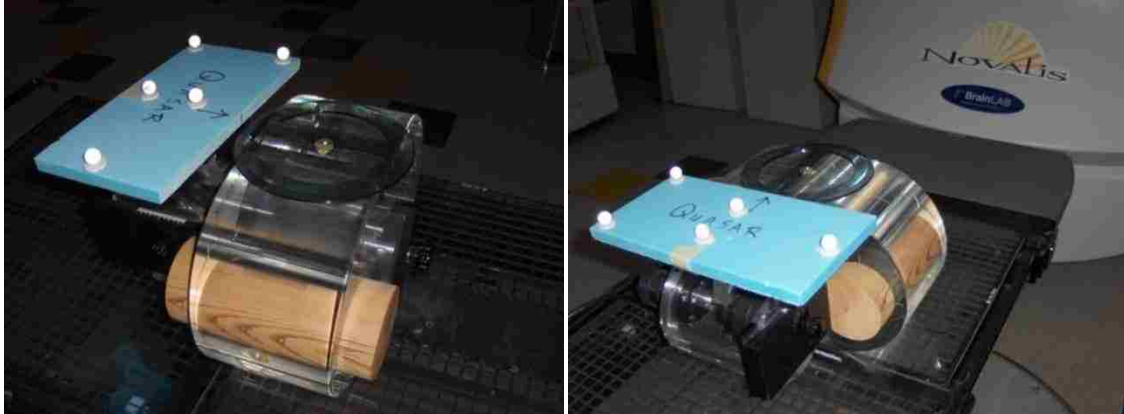


Figure 3.1: The Quasar Respiratory Motion phantom on the Novalis treatment couch and five reflective BrainLab bodymarkers used by the ExacTrac system to monitor the external chest wall/platform motion

### 3.1.2 Implanted Markers

Due to the lack of radiographic contrast in tissues such as lung, surrogates are commonly used to measure internal tumor motion. The chest wall and diaphragm are commonly used motion surrogates, and their motions are strongly correlated (3.1). The diaphragm motion may correlate well with the vertical motion of the abdomen, but lung is a non-rigid tissue that may move and deform differently (3.2). To accurately track an internal tumor, an implanted fiducial marker gives more accurate information than just external patient monitoring.

To properly gate a treatment beam using external patient markers, the internal patient respiratory motion must be correlated with the external chest wall motion observed by the gating system. Ionascu et al. report that some patients should not be treated using only external markers as surrogates for internal motion (3.3). This is due to an occasionally observed phase shift in the external and internal motion correlation of some patients. Some systems, such as the Varian RPM gating system, utilize a method of tracking external markers to gate the treatment beam without correlation to the position of the internal target (3.4). One way of gating without using an external surrogate as a monitor of the patient's internal movement involves fluoroscopic tracking

of the target, but this can result in unnecessary patient dose and may suffer from low target contrast with the surrounding tissues.

An implanted fiducial marker, such as a metallic coil, is desirable for imaging using the ExacTrac kV x-ray system to provide better contrast with surrounding patient anatomy, and better correlation to the tumor motion than using solely external markers. After the coil is implanted, the relation between the coil location and the tumor or target location can be verified using 4DCT. If the coil is placed close enough to the tumor, then the coil can provide an excellent internal surrogate to image instead of the tumor because some tumors (e.g. lung or liver) may be difficult to detect on x-ray images. Willoughby et al. have shown that the fiducial coil implants into lung tissue did not migrate over the course of their study (3.5). Nelson et al. reported that smaller implanted spherical and cylindrical markers either dislodged completely or remained in place throughout their study (3.2). The study by Yan et al. concluded the ExacTrac implanted marker registration and setup showed a higher degree of accuracy over the using an anatomical image fusion method (3.6).

By utilizing the x-ray system to image the implanted coil, the user can ensure the internal target is at the planned treatment position using the relation of the implanted coil to the tumor location. The ET imaging system allows for a correlation of external infrared-reflecting markers (Bodymarkers) to internal target position as defined in relation to the implanted coil.

### **3.1.3 4DCT Acquisition**

By determining the most accurate and stable 4DCT respiratory dataset, this project can recommend which breathing phase to use as the reference breathing phase, about which the beam is gated within a predefined phase window. This project anticipates this to be the full-exhale (50%) phase of respiration. Studies have shown that the exhale phases of respiration last longer than the inhalation phases of respiration, thus a patient spends more time at exhale than at inhale

(3.1, 3.7). Exhalation is reported in these studies to be the most stable and reproducible position for patients.

4DCT data are acquired at MBPCC using the GE Advantage 4DCT v1.6 software on a GE Lightspeed RT multi-slice scanner (General Electric Company, Waukesha, WI). The Varian Real-Time Positioning Management (RPM) System (Varian Oncology Systems, Palo Alto, CA) is used as the external monitoring device. The patient's abdominal motion is monitored by the RPM camera system shown in Figure 3.2. An infrared (IR) camera mounted at the foot of the CT couch emits IR light that is reflected back to the camera via two markers on a plastic box affixed inferior to the patient's xiphoid process. As the patient breathes the RPM marker box moves with the chest wall motion. The time-dependant motion of the box is recorded by the camera system, and each image is identified with a time stamp. Thus, the position of the patient's chest wall as a function of time is saved as a RPM system file.



Figure 3.2: Varian RPM system 4DCT infrared camera mounted at base of CT couch (left) and the Quasar respiratory phantom affixed with the RPM marker box (blue circle) as seen from the camera's point of view (right)

In 4DCT acquisition, a cine CT is acquired, where the couch remains stationary during data acquisition, then indexes to the next couch position until desired field-of-view is imaged. Once the scan is completed, the cine CT scan data and the RPM chest wall motion data are sent to the GE Advantage computer for sorting. The sorting program takes the cine scan data, and



correlates the timestamp on each projection image to the RPM file to determine the relative chest wall amplitude level for each projection. Then the projection data images are sorted by the computer into 10 distinct phases ranging from full inhale (0% phase) to full exhale (50% phase) and back to inhale using the relative chest wall amplitude. The technical aspects of the acquisition and reconstruction of the 4DCT images are discussed elsewhere in literature (3.8, 3.9, 3.10). The phase-sorted projection images are recombined to create a unique CT data set for each phase. Additionally, the computer uses the entire cine scan to produce a maximum-intensity projection (MIP), minimum-intensity (Min-IP) dataset, and an average intensity (Avg-IP) data set. The sorting computer creates the MIP by examining each pixel and assigning each pixel the highest value observed at that location over all ten phase-sorted images. Similarly, the Avg-IP and Min-IP data sets show the average and minimum pixel value, respectively, observed over all ten phases. The MIP is particularly important since as a solid tumor moves, the MIP shows the extent of tumor motion over all phases of respiration. Currently, the MIP is used to establish the extent of tumor respiratory motion to design the radiation beams that fully encompass the tumor motion.

### **3.1.4 ExacTrac System**

The ExacTrac (ET) Gating system was developed by BrainLab (Munich, Germany) to allow image guidance and respiratory gating on the Novalis linear accelerator. This system combines two kilo-voltage (kV) x-ray tubes, two amorphous silicon image detector panels, an infrared optical camera system, and an interface to the linear accelerator. Figure 3.3 shows a conceptual picture of how the kV x-ray tubes project through the patient onto the detector panels. Figure 3.4 shows the flat panel detectors and Figure 3.5 is a picture of the floor mounted x-ray tube with and without covers.

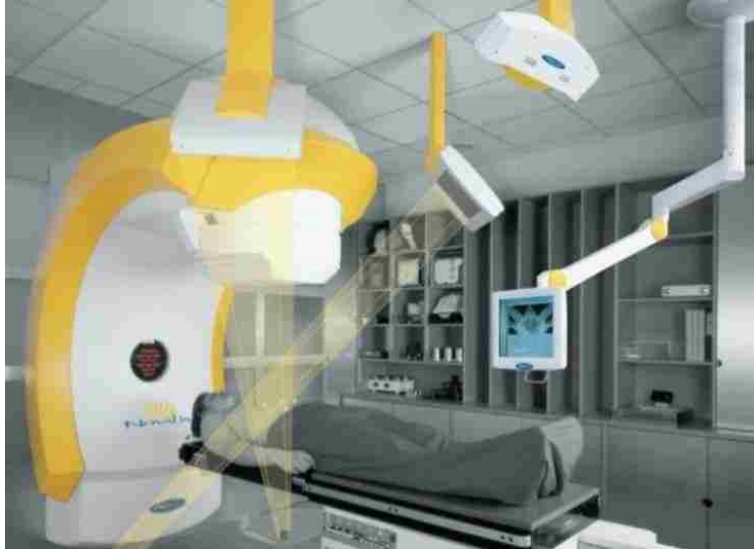


Figure 3.3: Conceptual picture of the ExacTrac kV orthogonal x-rays (courtesy of BrainLab).



Figure 3.4: Picture of the ExacTrac amorphous silicon image detector mounted to the ceiling.



Figure 3.5: Picture of covered kV x-ray housing panel in floor (left) and with cover removed (right)

This system is installed on a Novalis (BrainLab, Munich, Germany) therapy machine, which is a 6 MV linear accelerator with a BrainLab M3 micro-multileaf collimator. The ET gating software monitors external bodymarkers (seen in Figure 3.1) and only allows radiation delivery when the markers are within a predetermined window of respiratory amplitude. Radiation output constancy has been reported to be better than 0.5% when the radiation beam was gated in situations with many beam interruptions, as compared to a non-gated delivery (3.5).

The ET gating system uses a combination of infrared/optical and x-ray tracking to setup and monitor the patient and, ultimately, to deliver the gated treatment. The breathing signal tracked by the ExacTrac system is based on the vertical movement of infrared reflecting bodymarkers attached to the patient/phantom as seen by the infrared camera. The camera system consists of two independently mounted infrared cameras along with a video camera for visual monitoring on a rail above the foot of the treatment couch, as seen in Figure 3.6. To eliminate the influence of any couch movement on the observed breathing trace, a stationary reference object is also monitored by the cameras. As a stable reference object, BrainLab has developed the “Reference Star” which consists of 4 infrared reflecting pads held in a known trapezoidal configuration supported by an arm mounted to the side of the treatment couch. The Reference

Star is shown in Figure 3.7 mounted over a phantom on the Novalis treatment couch. The ET system illuminates and observes the moving patient-mounted bodymarkers as well as the 4 reflecting pads of the Reference Star. The breathing motion is calculated from the relative positions of the external patient bodymarkers as compared to the stationary markers on the Reference Star. Yan et al. provides a description of how the ExacTrac system resolves the three dimensional position of the markers from the two dimensional camera information (3.6)

First, the user selects the reference gating level in the ExacTrac system. At this point in the respiratory cycle, the target isocenter will be placed at the machine isocenter. When the patient's chest wall amplitude, as monitored by the ET Bodymarkers, matches the reference gating level (near full-exhale for our studies), ExacTrac acquires an image from an x-ray imaging panel. A subsequent image is taken on another respiration but at the same point of the respiratory trace with the other x-ray tube after the user has confirmed the first image is acceptable. Once both images are accepted, digitally reconstructed radiographs (DRR) corresponding to the x-ray tube/flat panel imager orientations are calculated from the planning CT dataset by ExacTrac and compared to the ExacTrac x-ray images. Figure 3.8 shows an example of a DRR created from the 4DCT dataset compared to a corresponding image from the ExacTrac x-ray imaging system. ExacTrac calculates a position shift corresponding to the difference of the current ExacTrac setup and planned target location by correlating the DRR from the CT and daily setup x-rays (using anatomy, implanted fiducials, etc.).

The patient/phantom is repositioned so that the target is at the isocenter of the beam when the breathing trace intersects the gating reference level. The shift to reposition the patient is calculated by the ExacTrac software. When using implanted fiducial alignment, the user-defined position of the coil in planning CT dataset is used to align the position of the coil as calculated from the imaged coil position from the kV x-ray panels.



Figure 3.6: The infrared camera system mounted in the Novalis room. The red circles indicate the infrared cameras used for monitoring the external BrainLab bodymarkers. The blue circle identifies as an optical-light camera for visual monitoring.

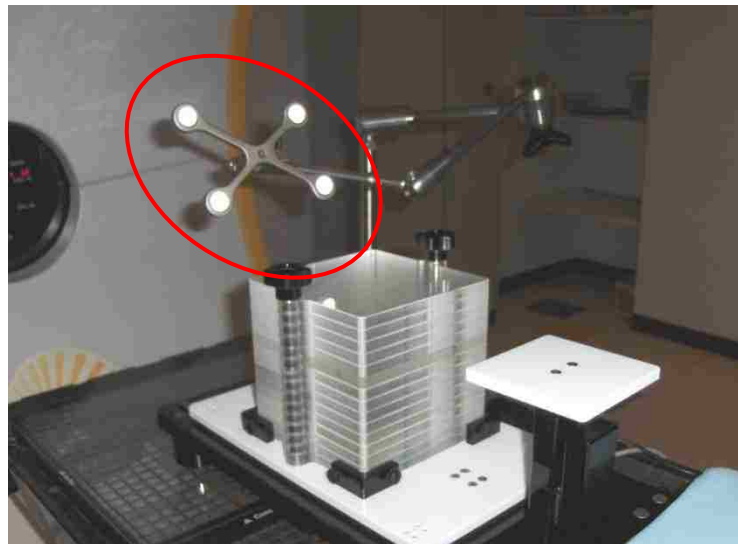


Figure 3.7: The ET Reference Star (circled in red) is shown mounted over a phantom on the Novalis treatment couch.

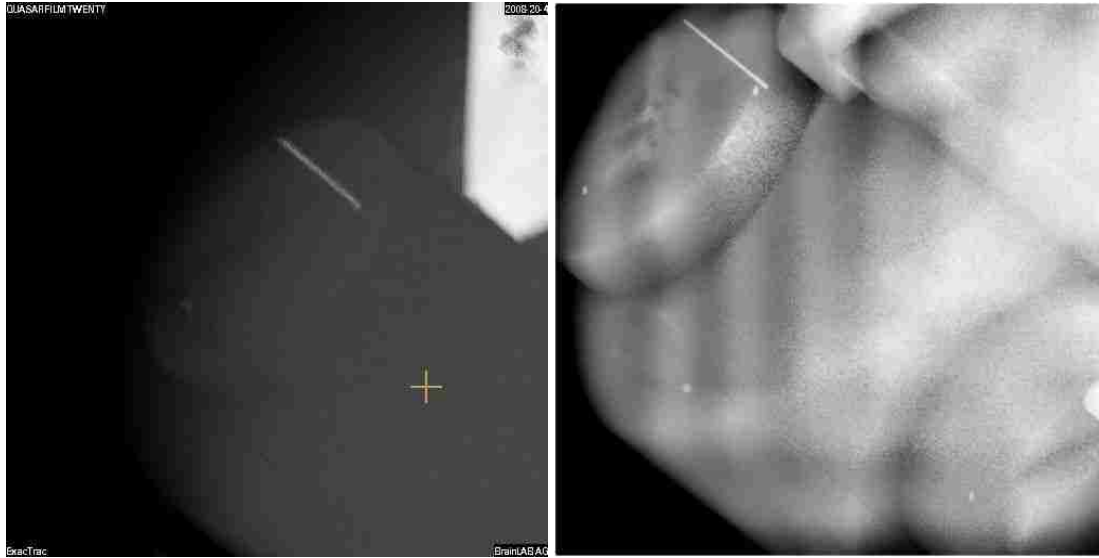


Figure 3.8: Comparison of the DRR from the 4DCT (left) and a corresponding kV x-ray image from ExacTrac. The orange cross in the left image represents the planning isocenter. When the user identifies the location of the coil in the DRR and ExacTrac images, the system calculates the location of the planning isocenter to the machine isocenter

The right panel of Figure 3.8 shows the coil is displaced from the DRR constructed from the planning CT dataset (left). The ExacTrac will calculate a 3-dimensional shift to place the coil at the same position as seen the planning CT dataset.

Images at respiration levels other than the gating reference level can be taken as well, allowing the user the ability to determine coil/tumor motion/position at other amplitude levels. Once the imaging is complete and the patient is aligned, treatment is enabled. The treatment beam is then gated on for a percentage of the relative respiratory trace centered about the gating reference level.

To image at a pre-selected respiratory amplitude level, the ExacTrac software takes several factors into account. The ET software extrapolates the breathing motion from the external markers and estimates when the measured breathing amplitude will match the desired imaging amplitude. The imaging panels must be continuously read out to remove charge that may have

built-up on the pixel electrode due to dark current. The software must manage the readout to ensure a “clean” detector panel is ready to acquire an x-ray exposure, and to time the mid-point of the acquisition to be at the anticipated moment the breathing amplitude matches the imaging amplitude. The software must time the start of the exposure to occur at half of the exposure time before the desired time of exposure. When imaging a moving target such as the coil inside the ET phantom, we are actually measuring the accuracy of the predictive algorithm to acquire the x-ray image when it anticipates the target to be in the requested imaging amplitude.

The ExacTrac predictive breathing algorithm for x-ray acquisition only cues off the patient’s respiratory motion from full inhale (0% Phase, 100% Amplitude) to full exhale (50% Phase, 0% Amplitude). Thus, ExacTrac can only produce images which would correspond to 4DCT phase images from 0% to 50%.

The size of the gating window should be determined based on the desired additional margins used for treatment planning, or vice versa. By restricting the gating window to a very narrow range of chest wall amplitudes during respiration, the target movement during the beam-on time will be reduced. However, the overall treatment time will be expanded due to the limited beam-on time. Once the patient is correctly positioned and target position is verified at the gating reference level, ExacTrac gates the treatment delivery from the linear accelerator when the respiratory markers are observed to be within the gating window. At any time during the treatment, the user can acquire additional x-ray images to ensure that proper patient positioning is maintained, even if changes in the patient’s respiratory characteristics are suspected.

## **3.2 Methods and Materials**

To determine the coil localization accuracy of the ET Gating system in comparison to the 4DCT, this aim acquired 4DCT scans using the Quasar respiratory phantom with a preselected assortment of respiratory amplitudes (5-25 mm) utilizing sinusoidal one-dimensional motion.

The 4DCT data was sorted by the GE 4DAdvantage software and files were prepared for import into Pinnacle<sup>3</sup> (Philips Medical Systems, Bothell, WA) treatment planning system (TPS) version 8.0, hereafter referred to as the Pinnacle TPS. In Pinnacle, the user identified the endpoints of the implanted coil in each respiratory phase. The identified coil endpoint data from each phase was extracted to determine the overall coil motion from phase to phase for the 4DCT data.

With identical phantom motion parameters, ExacTrac images were acquired at each phase investigated on the 4DCT dataset. The software reported the locations of the coil midpoints in the ExacTrac coordinate system. The measured coil motions in the ExacTrac and 4DCT systems were compared to the expected coil displacements over the tracked phases of respiration. Because the Quasar phantom motion moves with sinusoidal motion with specified amplitude and period, the overall motion of the coil is known for all phases of respiration.

### **3.2.1 The Quasar Motion Phantom**

The Quasar phantom was shown in Figure 3.1 with a wooden canister insert designed to simulate a patient's lung. The canister was modified to accept a Visicoil by scoring the anterior outer surface of the cylinder. The coil was secured in the wooden insert so that it would not move during phantom motion.

For our studies, the solid blue piece of foam affixed to the platform represents the patient chest wall, which moves in the anterior-posterior (AP) direction. The blue foam board was added to provide a wider chest platform that could be removed from the phantom if needed. This setup gives the external chest markers uniform motion amplitude in the AP direction. The ExacTrac Gating system triggers the radiation delivery based on the marker motion detected by the cameras. The bodymarkers shown in Figure 3.1 reflect the infrared (IR) light back to the camera system mounted above the foot of the couch, previously seen in Figure 3.6.



The Quasar phantom was tracked by the ExacTrac infrared camera system, observing the motion of the reflecting bodymarkers for an extended period of time (~10 minutes). The relative position of the markers was recorded by the ExacTrac system. The Quasar phantom's marker motion matched a sinusoidal curve. The Quasar phantom was observed to be sinusoidal, stable, and repetitive.

### 3.2.2 Implanted Markers

An internal marker (Visicoil; RadioMed Corporation, Tyngsboro, MA) was used as a surrogate for internal tumor motion. Figure 3.9 shows a sample Visicoil imbedded in plastic. The Visicoil markers used for this project measured 30.8 mm in length, and 0.8 mm in diameter.



Figure 3.9: An example of the Visicoil inserted into the Quasar moving canister for imaging purposes.

### 3.2.3 Phantom Motion Criteria

In order to evaluate the 4DCT and ExacTrac systems independently, it was necessary to standardize the phantom characteristics that will be measured in each system. First, it was determined what overall tumor motion to replicate with our phantom. AAPM Report 91 (3.11) recommends that respiratory gating should be considered only when tumor respiratory motion exceeds 5 mm. Ionascu et al. reports that, for most patients, a superior-inferior tumor movement

over 20 mm is relatively uncommon (3.3). Thus, this work restricted the phantom respiratory motions to amplitudes of 5, 10, 15, 20 and 25 mm motion in the SI direction.

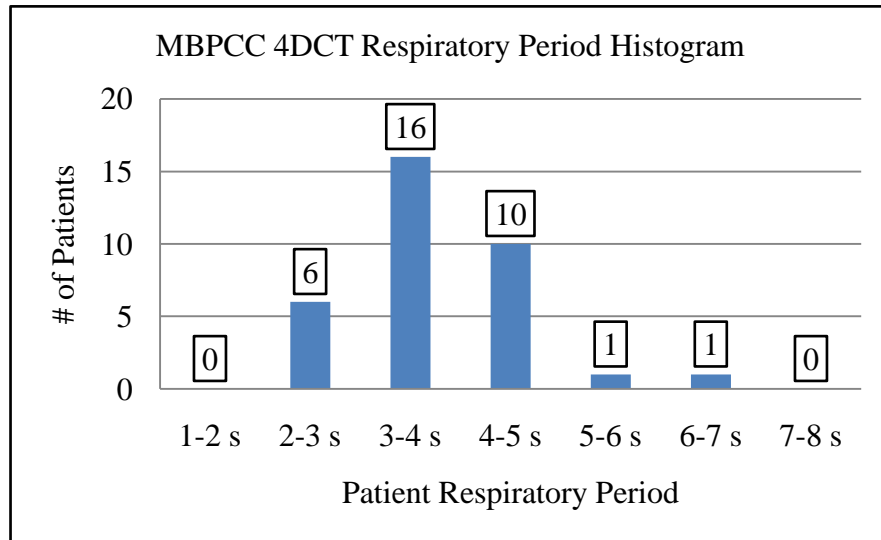


Figure 3.10: MBPCC Respiratory period histogram from 34 patients scanned with clinical 4DCT protocol recorded by the Varian RPM system.

The patient chest wall motion is mimicked by the marker platform of the Quasar phantom. This project looked at patient data from the Varian RPM system to determine a value for the phantom respiratory period settings. 4DCT patient data were analyzed to obtain an average respiratory period. Of 50 patients with RPM files, only 34 had reproducible and sustained breathing traces recorded. Most of the 34 patients had respiratory periods of 3-5 seconds (Figure 3.10). The average for all 34 patients was  $3.7 \pm 0.8$  seconds. This correlates well with findings by Seppenwoolde that report an average respiratory period of  $3.6 \pm 0.8$  seconds (3.12).

Also of interest is that the RPM system records the length of time the patient spent in exhale phases and inhale phases. For the 34 patients studied, an average exhalation length of 2.1 seconds was observed compared to an average inhalation length of 1.5 seconds. This agrees with the observations reported in literature (3.12). Thus, a treatment that places a gating window

about the exhalation phases of respiration would have a larger percentage of time with the beam enabled, resulting in a relative decrease in the treatment time.

### **3.2.4 4DCT Methods**

All 4DCT scans taken during this project utilized the current clinical protocols. A slice thickness of 2.5 mm for four slices per cine was used so that at each couch position, the coverage is 10 mm in the cranial-caudal direction. X-ray tube settings of 120 kV and 440 mA were used. The phantom was scanned at 1.0 second per revolution gantry speed rotation. The current clinical protocols recommend a cine duration time equal to the breathing period of the patient plus 2.0 seconds, so cine duration was set to 6.0 seconds.

The phase-sorted datasets were reconstructed and sent to the Pinnacle TPS. Due to current limitations in the Pinnacle planning software, the description field containing the phase information cannot be viewed when importing the datasets into a plan. Thus, the user cannot identify the phase-sorted datasets. Connel Chu, M.S. at MBPCC has developed a program which pulls the phase-sorted datasets from the Pinnacle import directory, appends the image dataset name with the description field, and replaces the old files with the new renamed files. Then, the user can identify the phase value for each image set when importing the data into Pinnacle. Once all 10 phase-sorted datasets were imported, along with the 3 intensity projection images, and possibly a helical scan, up to 14 datasets were associated with each plan.

### **3.2.5 4DCT Coil Motion Study**

In order to evaluate the effects of respiratory motion on the 4DCT images of the implanted coil, the 4DCT process was repeated five times on the Quasar phantom for amplitudes of 5, 10, 15, 20 and 25 mm. Separate phantom-based patients were created where all phase-sorted datasets were imported for each of the scanned amplitudes. Utilizing a bone-optimized viewing window in the Pinnacle TPS, both the superior and inferior ends of the implanted coil

were identified on each phase. Each point was assigned as a point-of-interest (POI) in Pinnacle. This information was exported to Excel to calculate the overall detected coil length. This was compared to the known physical coil length to determine error in imaging the coil length in each phase.

The actual distance the coil endpoints moved between phases was also determined from the programmed sinusoidal motion of the phantom. The measured motion of the coil endpoints was then compared to the actual motion of the coil to determine the accuracy of the 4DCT in localizing a coil over all respiratory phases.

### **3.2.6 ExacTrac Coil Motion Study**

Three tests were conducted for this study. First, since the user must select the coil endpoints on each x-ray image from the ExacTrac system, the reproducibility of the user's coil selection was investigated on a non-moving phantom. Next, with a moving phantom/coil, the repeatability of the ExacTrac in imaging the coil at the same location was tested. In the final test, the moving phantom was imaged over a subset of amplitude levels. The measured coil displacements were compared to the expected coil displacements for a coil moving with sinusoidal motion.

In the first test, the stationary phantom was repeatedly imaged by the ExacTrac system, and the coil endpoints were identified on each image. Since the coil was stationary, the only variation in the system was the user identifying the coil endpoints. Figure 3.11 shows a sample pair of x-rays taken from the Quasar phantom showing the implanted coil. The ExacTrac system calculated the three-dimensional position of the coil from each set of images.

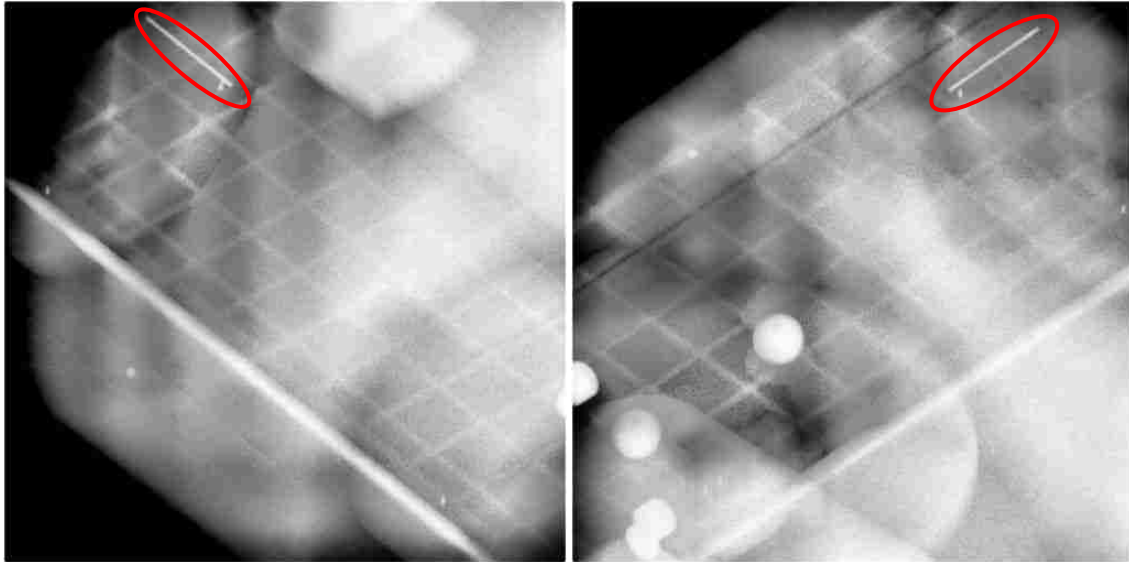


Figure 3.11: A pair of x-ray images obtained from the ExacTrac system used to identify the location of the implanted Visicoil. Coil is circled in red at the top left (left image) and top right (right image)

The second test involved moving the phantom at the maximum target motion amplitude used during this study (25 mm). This is a test to measure the maximum error in target localization. At the 50% amplitude of the sinusoidal motion, the coil is moving at the fastest velocity. At 50% amplitude of a 25 mm target motion, the phantom was imaged repeatedly to determine the variation in coil localization.

The third test measured the overall accuracy in the ExacTrac system to identify the position of the moving coil. To test the coil localization accuracy, the phantom's amplitude was set at 5, 10, 15, 20 or 25 mm target motion and imaged at amplitude levels that correspond to phases (0, 10, 20, 30, 40 and 50%) imaged in the 4DCT study. The relative motion of the coil in each phase was compared to the actual motion of the sinusoidal phantom for each respiratory amplitude/phase combination over all five motion amplitudes. Once images at all selected levels were obtained, the positions of the implanted coil endpoints were identified. Then, the ExacTrac system calculated the locations of the coil endpoints. For each imaging panel, x-ray settings of

100 kV and 200 mA were used, as this gave a clear image of the implanted coil. For every image, the ExacTrac gating system requires the x-ray duration equal 100 milliseconds.

Because the Quasar phantom moved in a consistent sinusoidal motion, the ET software should be able to extrapolate the breathing signal with minimal error. Relative amplitude levels of 0, 9.5, 34.5, 65.5, 90.5 and 100 percent correspond to respiratory phases of 50, 40, 30, 20, 10, and 0 percent, respectively, for a sinusoidal curve. These amplitude levels were the same, no matter what coil motion amplitude was selected. The imaging amplitude levels were set as defined above, and an image was acquired from each x-ray panel.

### **3.3 Results**

#### **3.3.1 4DCT Coil Endpoint Selection Accuracy**

The user errors in identifying coil ends in 4DCT images are shown in Table 3.1 for 50% (full-exhale) phase and in Table 3.2 for mid-exhale phase (20%). The variation of in user identification has a maximum standard deviation of 0.5 mm. The results demonstrate that the user's ability to repeatedly select the coil endpoints is not affected by the phase dataset observed. We can assume a user can localize the same coil endpoints on any phase-sorted CT dataset to within half a millimeter for the purposes of this project. In the Pinnacle coordinate system, the z-axis is the direction of coil motion, therefore we would expect the error in that direction to be slightly larger since the coil distortion and blurring would be in the z-direction. The z-direction is also in the direction of slice thickness, which has a lower spatial resolution than the other two axes.

Table 3.1: Reproducibility of 4DCT coil endpoint selection by user for full-exhale phase (all values in cm)

50% Phase (full exhale)						
	Superior Endpoint Coordinates			Inferior Endpoint Coordinates		
	<u>X (cm)</u>	<u>Y (cm)</u>	<u>Z (cm)</u>	<u>X (cm)</u>	<u>Y (cm)</u>	<u>Z (cm)</u>
attempt 1	10.03	-46.33	0.64	10.11	-46.31	3.83
attempt 2	10.04	-46.33	0.68	10.13	-46.31	3.85
attempt 3	10.03	-46.33	0.66	10.13	-46.32	3.82
attempt 4	10.05	-46.33	0.76	10.11	-46.31	3.81
attempt 5	10.08	-46.33	0.70	10.09	-46.30	3.85
1 $\sigma$	0.02	0.00	0.05	0.02	0.01	0.02

Table 3.2: Reproducibility of 4DCT coil endpoint selection by user for mid-exhale phase (all values are in cm)

20% Phase (mid-exhale)						
	Superior Endpoint Coordinates			Inferior Endpoint Coordinates		
	<u>X (cm)</u>	<u>Y (cm)</u>	<u>Z (cm)</u>	<u>X (cm)</u>	<u>Y (cm)</u>	<u>Z (cm)</u>
attempt 1	10.02	-46.33	-1.29	10.11	-46.33	2.83
attempt 2	10.02	-46.31	-1.28	10.11	-46.36	2.90
attempt 3	10.02	-46.34	-1.34	10.12	-46.36	2.86
attempt 4	10.03	-46.31	-1.34	10.11	-46.33	2.81
attempt 5	10.01	-46.33	-1.33	10.11	-46.31	2.94
1 $\sigma$	0.01	0.01	0.03	0.00	0.02	0.05

### **3.3.2 ET Coil Endpoint Selection Accuracy**

Table 3.3 shows, for 11 repeat acquisitions in the ET Gating system, the coordinate locations of the coil with respect to machine isocenter as determined by the kV x-ray imaging system. The first entry is at the origin of the coordinate system because the ExacTrac x-ray setup was used to position the stationary phantom such that the coil was at machine isocenter. On subsequent imaging sessions, the system should register no correction shift. For each following test in Table 3.3, the correction shift in all three axes was recorded. The results in Table 3.3 show that the user can select a non-moving coil's endpoints with an accuracy of less than a tenth of a millimeter (<0.06 mm).

To quantify the overall reproducibility of the ET Gating system, the Quasar phantom was set to 25 mm respiratory motion, to simulate the largest amplitude we would expect to see clinically. The ET Gating system was used to image the 50% relative amplitude level of the moving coil. The results are shown in Table 3.4. The coordinate set is the coil location with respect to machine isocenter established during attempt #1. The variation of the ExacTrac system in repeatedly imaging the fast moving coil is less than 0.2 mm at one standard deviation in the direction of motion.

In summary, the position of a stationary coil can be identified to within 0.5 mm in 4DCT images and to within 0.1mm in ExacTrac images. A moving coil could be located to within 0.2 mm in the direction of motion in the ET system.



Table 3.3: Repeat ET Gating imaging of the positions of a stationary coil midpoint to test a user’s ability to repeatedly identify the coil endpoints. Listed are the ExacTrac coordinates of the coil midpoint as calculated from the user-selected coil endpoints.

	<u>X (mm)</u>	<u>Y (mm)</u>	<u>Z (mm)</u>
Attempt 1	0.00	0.00	0.00
Attempt 2	-0.01	-0.13	-0.06
Attempt 3	-0.02	0.00	-0.05
Attempt 4	-0.05	-0.07	-0.08
Attempt 5	0.03	-0.09	-0.03
Attempt 6	-0.13	0.06	-0.07
Attempt 7	0.09	-0.05	-0.06
Attempt 8	0.07	0.00	-0.09
Attempt 9	0.00	-0.03	-0.04
Attempt 10	0.01	-0.06	-0.09
Attempt 11	0.04	-0.09	-0.07
Average	0.00	-0.04	-0.06
1 $\sigma$	0.06	0.05	0.03

Table 3.4: Repeat ET imaging of a coil undergoing 25mm sinusoidal motion at 50% amplitude. All values in mm.

	<u>X (mm)</u>	<u>Y (mm)</u>	<u>Z (mm)</u>
Attempt 1	0.00	0.00	0.00
Attempt 2	0.04	-0.22	0.16
Attempt 3	0.06	-0.13	0.15
Attempt 4	0.08	-0.20	0.13
Attempt 5	0.08	0.06	0.09
Attempt 6	0.08	0.13	0.19
Attempt 7	0.02	0.25	0.01
Attempt 8	0.08	-0.07	0.32
Attempt 9	-0.04	-0.23	0.09
Attempt 10	0.01	-0.11	0.00
Attempt 11	0.01	-0.22	0.13
Average	0.04	-0.07	0.12
1 $\sigma$	0.04	0.16	0.09

### 3.3.3 4DCT Coil Motion Distortion Results

Initial results from the 4DCT showed that motion artifacts are minimal at end-inhalation and exhalation respiratory phases (0 and 50% phase respectively). At intermediate phases, the coil is moving with velocity dependant on the phase of the sinusoidal motion observed. Table 3.5 shows the error (in millimeters) of the measured coil length for all 10 phases of respiration for all five amplitudes observed. Measured coil length was determined by calculating the distance in space between the two coil endpoints as identified by the user in the Pinnacle coordinate system. The actual physical length of the coil was 30.8 mm.

Table 3.5: Errors in 4DCT detected coil length over all phases for selected motion amplitudes. All values in mm.

Phase	5 mm	10 mm	15 mm	20 mm	25 mm
0%	0.0	0.5	0.7	0.7	0.4
10%	0.7	0.1	1.1	1.1	0.6
20%	0.6	1.1	1.6	1.2	8.1
30%	0.6	1.0	0.5	1.2	8.3
40%	0.4	1.0	1.4	0.9	1.5
50%	0.2	0.3	0.8	0.1	0.7
60%	0.0	0.1	1.4	0.8	0.6
70%	0.3	1.1	1.9	3.4	2.9
80%	0.3	1.6	1.3	1.5	3.4
90%	0.5	0.8	0.0	2.2	1.3

For the 0 and 50 percent phases (full-inhale and full-exhale, respectively) in which the coil was moving the least, the error in the measured coil length was the least. At these phases, the maximum measured distortion in the coil length was 0.8 mm at the 50% phase of the 15 mm motion profile. When the coil was moving the fastest, at mid-inhale for example, the errors in the

coil length grew larger as the overall coil displacement grew, as was expected. At 25% and 75% phases (corresponding to 50% amplitude of the sine curve), the coil had the highest velocity, thus the 20, 30, 70, 80% phases should show the most coil distortion. At 25 mm respiratory amplitude, 8.1 and 8.3 mm errors in the coil length were observed at 20 and 30% phase, while at end respiration phases, the coil length distortions were minimal (0.7 and 0.4 mm). Thus, coil distortion was minimized on full-exhale and full-inhale phase datasets. If one assumes the detected coil distortion to reproduce the distortion of any moving tumor volume, then the errors in detecting both the coil and target tumor volume would be minimized by selecting the end-exhalation or inspiration datasets. In general motion artifacts in the 4DCT datasets are minimized at phases where the coil motion is minimized, corresponding to full-exhale and full-inhale of the respiratory cycle. For treatment planning purposes, this study suggests using the full-exhale (50%) phase for all patients to minimize motion-induced distortion on the planning dataset.

### **3.3.4 Coil Localization Results**

For each phase of the sinusoidal respiratory motion of the Quasar phantom, the displacement of the coil in each phase was calculated. This calculated shift was compared to the shifts observed in the 4DCT datasets and with the ET Gating system. The data for both the superior and inferior points of the coil can be compared to the expected displacement from the previous phase.

In Table 3.6 the results of the coil localization comparison of the ET gating system to the 4DCT are given in millimeters. For reference, the 4DCT phase is correlated to the matching ExacTrac amplitude of the sinusoidal motion of the phantom in the first two columns. The CT Sup and CT Inf columns refer to the superior and inferior coil endpoints in the 4DCT data, respectively. To compare these two different systems with different coordinate system origins, the 50% phase data set was taken to be the origin of the coordinate system used to display the

data. From this origin, the relative displacement of the 4DCT derived coil endpoints are given in CT Sup and CT Inf. In the next two columns, ET 1 and ET 2 refer to two separate measurements of the ET Gating software where the coil was imaged at the ET amplitude given in the first column. The ET system does not give the user the location of the coil endpoints, but a “center of mass” of the coil points. This coil center displacement can be tracked throughout all of the amplitudes which correspond to the 4DCT phases measured in third and fourth columns. Two ExacTrac measurements were performed to provide additional displacement data to contrast with the two endpoint displacement studies from the 4DCT.

Finally, the “Calc Dist” column of Table 3.6a-e uses the overall measured phantom motion to mathematically calculate the displacement of a point moving with the measured sinusoidal motion. This column is a mathematical calculation from of the displacement of a sine curve at the phases observed (0-50%). The measured displacement of the coil as measured by the ExacTrac and 4DCT systems should match that of the calculated distance.

For a better illustration of the errors encountered in either system, Table 3.7 expresses the data above in terms of error from the Calc Dist column. As seen in the table, the maximum errors in the ET Gating systems are 0.7 and 0.8 mm, respectively, for the two ExacTrac trials. The maximum error in the 4DCT displacement was 5.5 mm. As the amplitude decreases, the 4DCT shows better accuracy in localizing the coil. In the ET Gating system, a similar increase in accuracy is noted when the coil motion amplitude is decreased. However, at larger amplitudes, the ET Gating system can still localize the coil to sub-millimeter accuracy.

Table 3.6 a-e: Comparison of 4DCT vs. ET Gating coil localization

a. Quasar 5 mm Motion Results (mm)						
<u>ExacTrac</u>	<u>CT Phase</u>	<u>CT Sup</u>	<u>CT Inf</u>	<u>ET 1</u>	<u>ET 2</u>	<u>Calc Dist</u>
0.0%	50%	-	-	-	-	0.0
9.5%	40%	0.7	0.9	0.5	0.4	0.5
34.5%	30%	1.3	1.7	2.1	2.0	1.9
65.5%	20%	4.1	4.5	3.7	3.8	3.6
90.5%	10%	4.8	5.3	5.1	5.2	5.0
100.0%	0%	6.1	5.9	5.5	5.6	5.5

b. Quasar 10 mm Motion Results (mm)						
<u>ExacTrac</u>	<u>CT Phase</u>	<u>CT Sup</u>	<u>CT Inf</u>	<u>ET 1</u>	<u>ET 2</u>	<u>Calc Dist</u>
0.0%	50%	-	-	-	-	0.0
9.5%	40%	1.1	0.4	1.0	0.7	1.0
34.5%	30%	2.7	2.0	3.7	3.7	3.5
65.5%	20%	6.8	6.0	6.9	6.9	6.6
90.5%	10%	8.9	9.1	9.2	9.3	9.1
100.0%	0%	10.0	9.8	10.3	10.1	10.0

c. Quasar 15 mm Motion Results (mm)						
<u>ExacTrac</u>	<u>CT Phase</u>	<u>CT Sup</u>	<u>CT Inf</u>	<u>ET 1</u>	<u>ET 2</u>	<u>Calc Dist</u>
0.0%	50%	-	-	-	-	0.0
9.5%	40%	1.0	0.4	1.8	1.6	1.4
34.5%	30%	1.7	3.0	5.8	5.9	5.2
65.5%	20%	6.7	5.9	10.5	10.6	9.8
90.5%	10%	11.5	13.4	13.8	14.1	13.6
100.0%	0%	13.8	13.9	15.4	15.5	15.0

d. Quasar 20 mm Motion Results (mm)						
<u>ExacTrac</u>	<u>CT Phase</u>	<u>CT Sup</u>	<u>CT Inf</u>	<u>ET 1</u>	<u>ET 2</u>	<u>Calc Dist</u>
0.0%	50%	-	-	-	-	0.0
9.5%	40%	1.0	0.2	1.6	1.8	1.9
34.5%	30%	7.5	6.4	7.6	7.2	6.9
65.5%	20%	11.9	10.8	13.4	13.5	13.1
90.5%	10%	16.6	17.8	18.1	17.9	18.1
100.0%	0%	18.9	18.3	20.2	19.9	20.0

(Table 3.6 cont.)

e. Quasar 25 mm Motion Results (mm)						
<u>ExacTrac</u>	<u>CT Phase</u>	<u>CT Sup</u>	<u>CT Inf</u>	<u>ET 1</u>	<u>ET 2</u>	<u>Calc Dist</u>
0.0%	50%	-	-	-	-	0.0
9.5%	40%	2.8	2.0	2.3	2.7	2.4
34.5%	30%	12.1	4.5	9.2	9.4	8.8
65.5%	20%	18.6	11.2	17.3	17.4	16.7
90.5%	10%	22.3	23.6	23.1	23.3	23.1
100.0%	0%	24.4	24.7	25.4	25.2	25.5

Table 3.7a-e: Comparison of errors of the 4DCT vs. ET Gating system. The largest observed errors are highlighted for each data set.

a. Quasar 5 mm Motion Results (mm)					
<u>ExacTrac</u>	<u>CT Phase</u>	<u>CT Sup</u>	<u>CT Inf</u>	<u>ET 1</u>	<u>ET 2</u>
0.0%	50%	-	-	-	-
9.5%	40%	0.2	0.4	0.0	-0.1
34.5%	30%	-0.6	-0.2	0.2	0.1
65.5%	20%	0.5	0.9	0.1	0.2
90.5%	10%	-0.2	0.3	0.1	0.2
100.0%	0%	0.6	0.4	0.0	0.1

b. Quasar 10 mm Coil Localization Errors (mm)					
<u>ExacTrac</u>	<u>CT Phase</u>	<u>CT Sup</u>	<u>CT Inf</u>	<u>ET 1</u>	<u>ET 2</u>
0.0%	50%	-	-	-	-
9.5%	40%	0.1	-0.6	0.0	-0.3
34.5%	30%	-0.8	-1.5	0.2	0.2
65.5%	20%	0.2	-0.6	0.3	0.3
90.5%	10%	-0.2	0.0	0.1	0.2
100.0%	0%	0.0	-0.2	0.3	0.1

c. Quasar 15 mm Localization Errors (mm)					
<u>ExacTrac</u>	<u>CT Phase</u>	<u>CT Sup</u>	<u>CT Inf</u>	<u>ET 1</u>	<u>ET 2</u>
0.0%	50%	-	-	-	-
9.5%	40%	-0.4	-1.0	0.4	0.2
34.5%	30%	-3.5	-2.2	0.6	0.7
65.5%	20%	-3.1	-3.9	0.7	0.8
90.5%	10%	-2.1	-0.2	0.2	0.5
100.0%	0%	-1.2	-1.1	0.4	0.5

(Table 3.7 cont.)

d. Quasar 20 mm Localization Errors (mm)					
<u>ExacTrac</u>	<u>CT Phase</u>	<u>CT Sup</u>	<u>CT Inf</u>	<u>ET 1</u>	<u>ET 2</u>
0.0%	50%	-	-	-	-
9.5%	40%	-0.9	-1.7	-0.3	-0.1
34.5%	30%	0.6	-0.5	0.7	0.3
65.5%	20%	-1.2	-2.3	0.3	0.4
90.5%	10%	-1.5	-0.3	0.0	-0.2
100.0%	0%	-1.1	-1.7	0.2	-0.1

e. Quasar 25 mm Localization Errors (mm)					
<u>ExacTrac</u>	<u>CT Phase</u>	<u>CT Sup</u>	<u>CT Inf</u>	<u>ET 1</u>	<u>ET 2</u>
0.0%	50%	-	-	-	-
9.5%	40%	0.4	-0.4	-0.1	0.3
34.5%	30%	3.3	-4.3	0.4	0.6
65.5%	20%	1.9	-5.5	0.6	0.7
90.5%	10%	-0.8	0.5	0.0	0.2
100.0%	0%	-1.1	-0.8	-0.1	-0.3

### 3.4 Conclusions

This work concludes that when identifying a coil on phase-sorted 4DCT datasets taken with our clinical protocols, a user can locate the coil endpoints with a variation less than 0.5 mm. From 4DCT studies of the measured coil length, it was determined that at full-exhale and full-inhale phases of respiration, motion-induced artifacts of a coil are less than a millimeter. The 4DCT phase-sorted datasets corresponding to full-exhale and full-inhale provide the most accurate image of the moving phantom or patient. Due to the mechanics of breathing, exhalation phases in patients are more stable and reproducible than inhalation phases. This project recommends using a full-exhale dataset for treatment planning system calculations and gating the radiation treatment about the full-exhale (50%) phase of respiration.

When determining the extent of a patient's respiratory motion with an implanted surrogate such as a coil, the ExacTrac system performs better than 4DCT at coil localization.

With the ExacTrac system's ability to localize a coil to sub-millimeter accuracy, it is reasonable to expect ExacTrac to be able to localize a moving coil in a patient with well-behaved (no coughing or gasping) chest wall motion. To accurately determine the direction and extent of patient's internal respiratory motion after coil implantation, this aim recommends using the ExacTrac system.

### **3.5 References**

- 3.1. S.S. Vedam, V.R. Kini, P.J. Keall, V. Ramakrishnan, H. Mostafavi, R. Mohan, "Quantifying the predictability of diaphragm motion during respiration with a non-invasive external marker," *Med. Phys.* 30, 505-513 (2003).
- 3.2. C. Nelson, G. Starkshall, P. Balter, R. C. Morice, C. W. Stevens and J. Y. Chang, "Assessment of lung tumor motion and setup uncertainties using implanted fiducials," *Int. J. Radiat. Onc. Biol. Phys.* 67, 915-923 (2007).
- 3.3. D Ionascu, S.B. Jiang, S. Nishioka, H. Shirato, R.I. Berbeco, "Internal-external correlation of respiratory induced motion in lung tumors," *Med. Phys.* 34, 3893-3903 (2007).
- 3.4. S. S. Vedam, P. J. Keall, V. R. Kini, and R. Mohan, "Determining parameters for respiration-gated radiotherapy," *Med. Phys.* 28, 2139-2146 (2001).
- 3.5. T.R. Willoughby, A. R. Forbes, D. Buchholz, K. M. Langen, T. H. Wagner, O. A. Zeidan, P. A. Kupelian, and S. L. Meeks, "Evaluation of an infrared camera and x-ray system using implanted fiducials in patients with lung tumors for gated radiation therapy," *Int. J. Radiat. Oncol., Biol., Phys.* 66, 568-575 (2006).
- 3.6. H. Yan, F.F. Yin, and J.H. Kim, "A phantom study on the positioning accuracy of the Novalis Body system," *Med. Phys.* 30, 3052-3060 (2003).
- 3.7. H. D. Kubo, P. M. Len, S. Minohara, and H. Mostafavi, "Breathing-synchronized radiotherapy program at the University of California Davis Cancer Center," *Med. Phys.* 27, 346-353 (2000).
- 3.8. T. Pan, T.Y. Lee, E. Rietzel, G.T. Chen, "4D-CT imaging of a volume influenced by respiratory motion on multi-slice CT," *Med. Phys.* 31, 333-340 (2004).
- 3.9. E. Rietzel, T. Pan, G.T. Chen, "Four-dimensional computed tomography: Image formation and clinical protocol," *Med. Phys.* 32, 874-889 (2005).
- 3.10. T. Pan, X. Sun, and D. Luo, "Improvement of the cine-CT based 4DCT imaging," *Med. Phys.* 34, 4499-4503 (2007).



- 3.11. P.J. Keall, G. S. Mageras, J. M. Butler, R. S. Emery, K. M. Forster, S. B. Jiang, J. M. Kapatoes, D. A. Low, M. J. Murphy, B. R. Murray, C. R. Ramsey, M. B. Van Herk, S. S. Vedam, J. W. Wong, E. Yorke, "The management of respiratory motion in radiation oncology report of AAPM Task Group 76," *Med. Phys.* 33, 3874-3900 (2006).
- 3.12. Y. Seppenwoolde, H. Shirato, K. Kitamura, S. Shimazu, M. van Herk, J. V. Lebesque, and K. Miyasaka, "Precise and real-time measurements of 3D tumor motion in the lung due to breathing and heartbeat, measured during radiotherapy," *Int. J. Radiat. Oncol. Biol. Phys.* 53(4), 822-834 (2002).

## **4 Aim 3: Measure the Spatial Distribution of Dose to a Moving Phantom Using a Variety of Gating Window Levels and Amplitudes for Sinusoidal Motion.**

### **4.1 Introduction**

This aim studied ITV margins for various target motions and gating window levels such that gated delivery produced the same 95% therapeutic dose coverage as delivery to a stationary phantom. With any target motion and gating window level used, it may be expected that expanding the field size in the direction of motion by the total amplitude of the motion during the gating window (residual motion) would fully re-achieve the target coverage as observed in the static phantom delivery. The residual motion is dependent on the direction of motion, the magnitude of motion, and the percent amplitude of the respiratory cycle gating window level covers. This aim will investigate if expansion by the residual motion is adequate to maintain target coverage in the respiratory phantom.

This aim also determined which gating window levels limited ITV expansions to less than 3mm for target motions less than 25 mm. Recommendation for ITV expansions were developed for delivery to the Quasar respiratory phantom. Finally, dose-volume differences between gated and a non-gated delivery were estimated.

### **4.2 Methods and Materials**

A standardized treatment plan was created and delivered to the Quasar phantom. Gated delivery to the Quasar phantom in motion was compared to non-gated treatment delivery to the stationary phantom using radiochromic film measurements.

#### **4.2.1 Pinnacle Treatment Planning**

A 4DCT scan of the Quasar phantom with the film canister in place and moving with 20 mm amplitude was taken using the same cine CT scan conditions as outlined in Aim 2 (2.5 mm

slice thickness, 120 kV, 440 mA, 6 second cine duration.) The CT dataset at 50% phase (full exhale) was extracted. This phase shows the implanted coil with the least distortion over all phases, as measured in Aim #2. Full exhale was used as the reference gating level for all treatments in this study.

A 3-cm long by 3-cm diameter cylindrical region of interest (ROI) was created in the center of the film canister with the long axis of the ROI cylinder coinciding with the long axis of the canister. This region of interest was considered to be the planning CTV ( $CTV_{Plan}$ ) solely for placing the treatment beams and optimizing the beam weights. The plane containing the radiochromic film corresponded to a coronal slice through the phantom and passed through the center of the cylindrical  $CTV_{Plan}$ .

Nine co-planar beams were placed at 40 degree intervals around an isocenter located in the center of the  $CTV_{Plan}$ . This selection of a cylindrical  $CTV_{Plan}$  and a coplanar beam arrangement simplified the shape of the treatment beams because from all nine beam's eye views the  $CTV_{Plan}$  appeared as a  $3 \times 3 \text{ cm}^2$  square. The collimator of the linear accelerator was rotated such that the multi-leaf collimator leaves moved in the direction of target motion, allowing for continuous margin expansions in the direction of motion. This orientation was chosen because expansions perpendicular to leaf motion would have to be discrete steps of distance equal to the leaf widths. All beams were opened to a  $3.6 \times 3.6 \text{ cm}^2$  leaf-defined field size in order to cover the  $CTV_{Plan}$  with the prescription dose. The Novalis linac is capable of 6 MV photon beam output only, and the plan was designed accordingly.

The prescription dose was set at 400 cGy in order to reach the middle of the dynamic range of radiochromic EBT film. The Pinnacle system optimized the monitor units (MU) for each beam to attempt to provide a uniform dose of 400 cGy to the  $CTV_{Plan}$ .

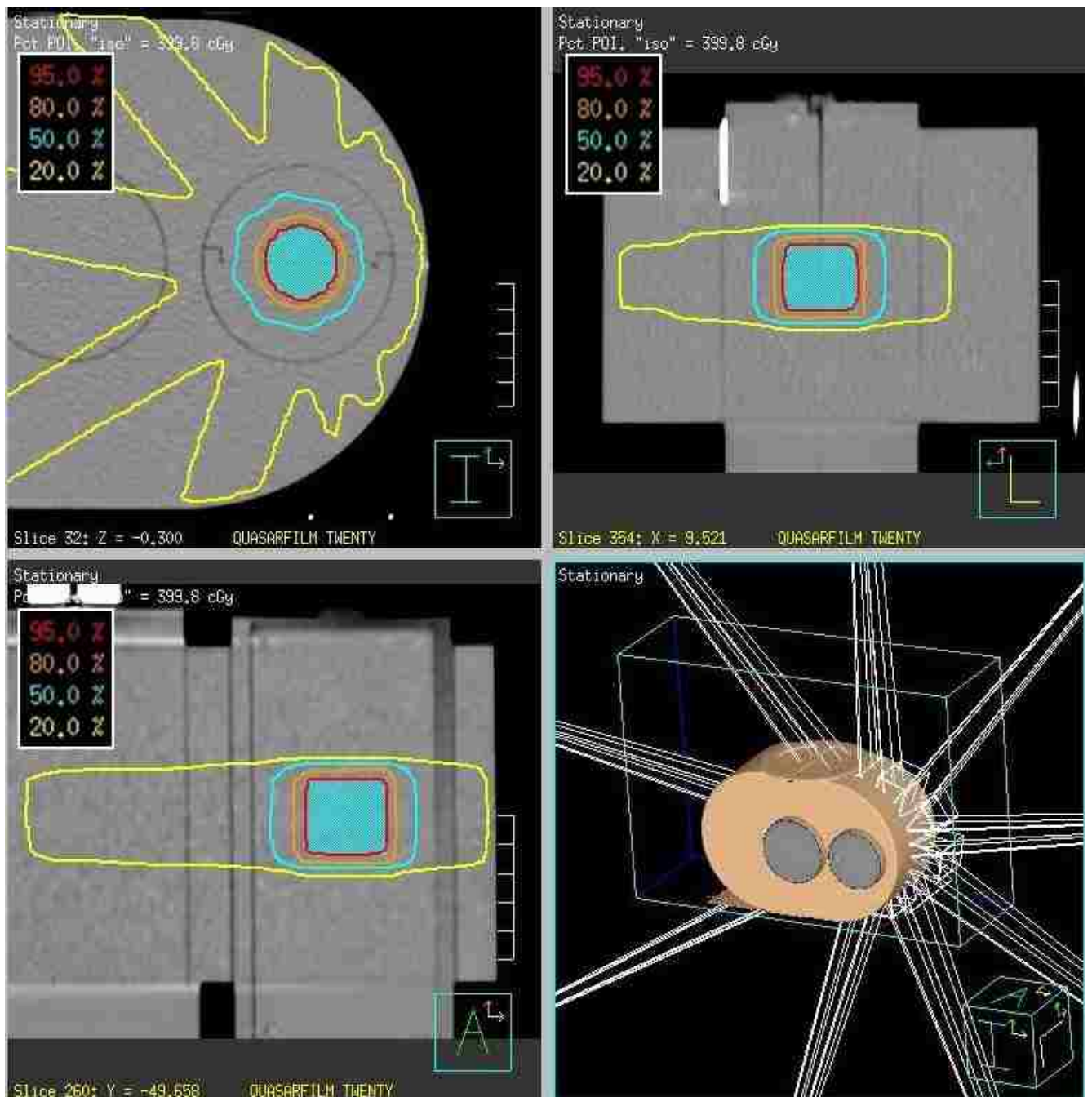


Figure 4.1: Pinnacle TPS orthogonal views of the conformal radiotherapy plan delivered to Quasar phantom. The planning data set is the 50% phase (full-exhale). The top left view is an axial view, top right is sagittal, and the bottom left view is a coronal slice. All three views were through the  $CTV_{Plan}$  isocenter. The bottom right view the nine beam arrangement placed around the  $CTV_{Plan}$  isocenter. The canister/target motion is in the superior-inferior direction.

Figure 4.1 shows a screenshot from the Pinnacle TPS containing three orthogonal views of the treatment plan on the 50% phase dataset and a 3D rendering of the phantom and beam

arrangements. The light blue region in Figure 4.1 is the  $CTV_{Plan}$ , and the dark red line signifies the 95% isodose line. The goal of the TPS beam weighting optimization was to uniformly cover the  $CTV_{Plan}$  with 400 cGy dose, and the 380 cGy dose was considered to be the 95% therapeutic dose. The  $CTV_{Plan}$  had a mean dose of 392.6, a minimum dose of 358.6 cGy, and maximum dose of 400.9 cGy. The isocenter dose of this plan was observed to be 399.9 cGy with 94% of the  $CTV_{Plan}$  receiving the therapeutic (95%) level of dose. We defined the volume that receives the 95% dose level to be the treatment CTV ( $CTV_T$ ), which is the area encompassed by the red 95% isodose lines in Figure 4.1. By definition, the  $CTV_T$  is completely covered by the 95% dose level, and still measures 3 centimeters wide in the direction of motion. For the remainder of this work, the  $CTV_T$  will be referred to as the CTV.

The plan was exported to the Novalis control station for plan delivery and to the ExacTrac control station for imaging setup and gating control.

### **4.2.2 Ion Chamber Measurements**

Ion chamber measurements were taken to provide an independent check of the actual dose delivered to the CTV. The Quasar phantom also includes an acrylic ion chamber insert canister machined to accept an Exradin model A16 micro ion-chamber (Standard Imaging, Middleton, WI) with a collecting volume of  $0.007 \text{ cm}^3$ . A MK602 electrometer (CNMC Company, Nashville, TN) recorded the charge measured by the chamber. The ion chamber canister replaces the film insert canister. This canister was modified to insert an imaging coil, so that the ExacTrac x-ray setup using implanted fiducials was available. The phantom was positioned using the room lasers so that the collecting volume of the chamber was at the machine isocenter when inserted into the ion chamber canister. Two ion chamber measurements were taken. The phantom was not moving during treatment for the two ion chamber measurements.

The ion chamber was calibrated assuming the Novalis machine output was 1 cGy/MU at reference conditions. Reference conditions are at 100 SSD at the depth of maximum dose (1.5 cm for the 6 MV beam of the Novalis accelerator) in a 30x30x2 cm<sup>2</sup> sheet of solid water with an additional 5 cm of backscatter using a 10x10 cm<sup>2</sup> field size. The chamber was irradiated with 500 MU (equal to 500 cGy in this calibration setup) in order to calculate the charge collected per unit of cGy. Experiment readings were divided by the charge collected per cGy to give the corresponding doses.

### **4.2.3 Radiochromic Film Phantom Measurements**

The Quasar phantom system also includes an acrylic insert canister for film dosimetry as shown in Figure 4.2. Using the treatment planning software, the density of the film canister insert was found to be the same as the acrylic used in the chest wall of the phantom. It provides a homogenous material to simplify the treatment planning calculations because the accuracy of the TPS heterogeneity correction is irrelevant to this study.

Figure 4.2 shows views of the Quasar phantom and film canister from the gantry and from the foot of the table. This study defines the superior end of the canister and phantom as the side towards the foot of the couch. This nomenclature was chosen to provide a comparative basis to motion expected in a patient. As a patient moves from full-exhale and begins to inhale, the diaphragm is expected to move inferiorly in order to expand the lungs for air intake. Tumors that are located in the lungs may have motion strongly influenced by the diaphragm, and the diaphragm motion has been shown to be strongly correlated to external markers (4.1). Therefore, the motions of external markers are correlated to internal diaphragm motion.



Figure 4.2: The Quasar phantom viewed from the gantry (left) and as viewed standing next to the foot of the couch (right). Labels denote the superior and inferior sides of the phantom.

Because we have decided to gate at full-exhale, the target would be at its most superior position in a patient and motion of the tumor would likely be in the inferior direction. Table 4.1 is taken from Chi, et al. (4.2) and summarizes the expected motion of a tumor from full-inhale (0% phase) to full-exhale (50% phase). By considering the motion of the phantom’s chest platform compared to the motion of the film canister, the phantom’s respiratory motion is that expected of a patient laying supine with feet towards the gantry.

Table 4.1: The most likely direction of tumor motion from full-inhale to full-exhale taken from Chi, et al.

TABLE 1. Definition of 0% and 50% based on the most likely direction of tumor motion. (S-I, superior-inferior anatomic direction; A-P, anterior-posterior anatomic direction; LAT, lateral anatomic direction; ROI, region of interest.)					
Percentage	Abdominal motion observed by RPM	Chest wall motion	Tumor motion		
			S-I	A-P	LAT
0	Highest amplitude (end inspiration)	Largest average CT number in ROI	Tumor at most inferior position	Tumor at most anterior position	Tumor farthest from mediastinum
50	Lowest amplitude (end expiration)	Smallest average CT number in ROI	Tumor at most superior position	Tumor at most posterior position	Tumor closest to mediastinum

The film canister was modified by milling a small channel into its anterior surface and attaching a coil identical to that used in Aim 2. The coil was inserted in the same orientation and

location as in Aim 2. Figure 4.3 shows the outer surface of the canister with the coil in place and its position in the phantom.

Figure 4.4a shows the open film canister with a cut piece of radiochromic EBT film in place. The internal surface of the canister contains five pins to facilitate film registration. In Figure 4.4b, the registration marks can be seen on the scanned image of a film as dots in the corners of the film. The bottom left corner of the canister contains two pins in order to record the orientation of the film.

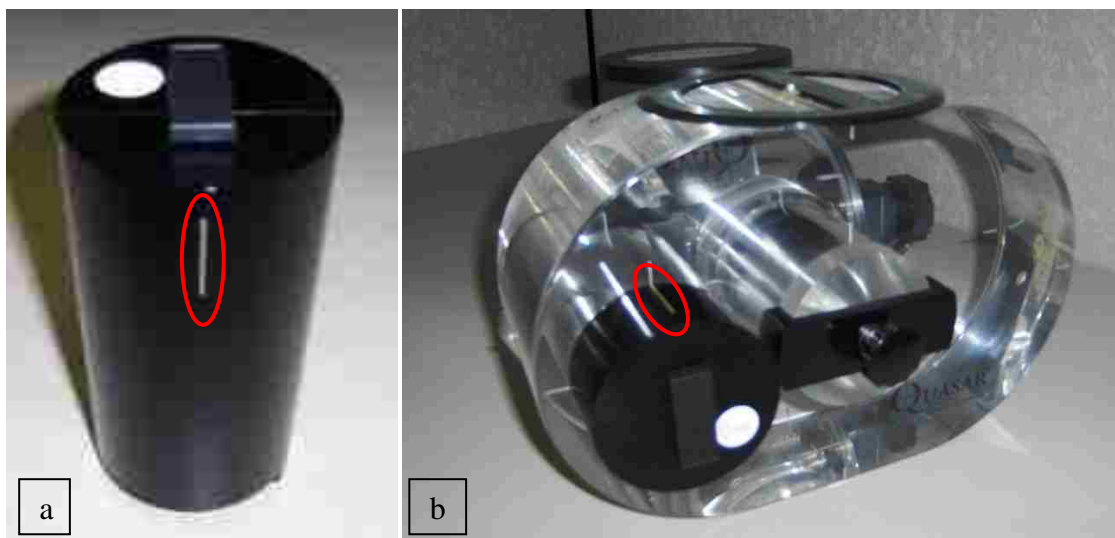


Figure 4.3: (a) Modification of the film insert canister for implanted coil (outlined in red) and (b) superior view of canister placement in Quasar phantom with coil (outlined in red) on anterior surface of the phantom's canister.

Three plan deliveries were performed and measured with film in the stationary phantom in order to establish the repeatability of the phantom setup and irradiation. After each delivery, the phantom was moved and the ET system implanted fiducial setup was used to position the phantom. For gated treatment delivery, the phantom was set up using the ET software. The phantom was positioned on the treatment couch and the motion was set to the desired target amplitude.





Figure 4.4: (a) Internal view of film canister with radiochromic EBT film in place and (b) sample film showing registration marks from Quasar film canister.

The ET system captured an image from each x-ray tube at the reference gating level, which was set at full-exhale. The user identified the coil endpoints in each image and the ET software reconstructed the three-dimensional location of the coil. The ET software then calculated a shift to place the treatment isocenter at the machine isocenter. Each time the phantom was handled, moved, or changed in any way other than removing the film canister, the ET implanted fiducial setup was repeated in order to insure the phantom was properly positioned.

Gated deliveries of the same treatment plan were performed with a variety of target motion amplitudes and gating window levels. The only change from the stationary delivery was that the ET software would turn the beam off when the external bodymarkers fell outside the gating window. The same treatment plan was delivered every time regardless of the target motion or gating window width studied. It was observed that at the smallest gating window of 10%, no less than 11 MU were delivered during each beam-on segment. A report by Ramsey et al. states that machine output, flatness and symmetry do not vary by more than 0.8% in gating

sequences when greater than 5 MU are delivered per gate (4.3). However, this was a machine-dependant test, and must be verified on any machine being commissioned for gated treatment.

Experiments were performed with target motion amplitudes of 5, 10, 15, 20, and 25 mm and with gating window levels of 10, 20, 30, 50, 80 and 100%. Clinics could potentially use 10-30% as a gating window width for a patient treatment. Gating windows 50% and 80% were selected to show extreme gating window effects. The 100% gating window is essentially a non-gated delivery with target motion since the beam never turns off, and it demonstrates how neglecting the effects of motion affects the delivered dose. In addition to the gated plan deliveries, the phantom motion was stopped at full-exhale, and the treatment plan was again delivered to the stationary phantom. This resulted in seven separate plan deliveries for each of the five amplitude settings. After each nine beam treatment plan was delivered, the film canister was removed, and the irradiated film was marked for identification purposes. The film was placed in an opaque film jacket inside the film box to allow for 24 hours of self-development before scanning and analysis.

#### **4.2.4 Film Analysis**

For scanning, experiment films were taped to a 14x17" sheet of non-irradiated, processed radiographic film to ensure that the experiment films transported smoothly through the Vidar film rollers (Figure 4.5). The large film guide also ensured that the experiment films were all scanned at the same location in the central portion of the scanner. One experiment film scan was selected as a template for aligning and rotating the scans of all the experimental films scans. In this alignment image, the registration marks were vertically aligned.

The RIT V5.0 software package was used to analyze the scanned films. On each film, a vertical profile was taken along the center of the film. A vertical profile corresponds to the direction of motion of the phantom. Any changes to the dose distribution due to phantom motion

would be manifested in the vertical direction on the film. The black arrows in Figure 4.6 demonstrate the direction of the vertical profile recorded for each film.



Figure 4.5: The Vidar film guide used for scanning films irradiated in the Quasar film canister.

Figure 4.6 shows the effect of respiratory motion on delivered dose. The film on the left was treated with a 100% gating window (a non-gated delivery) to a target with 20 mm motion amplitude. The film on the right was treated without motion and represents the ideal dose distribution achievable by the plan delivery.

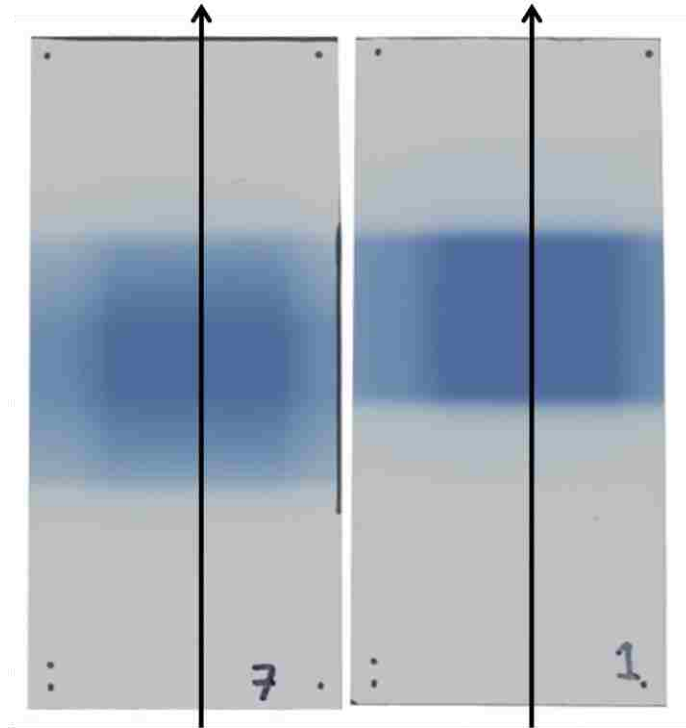


Figure 4.6: Gated delivery with 100% gating level and 20 mm target motion film (left) vs. static phantom plan delivery film (right) with black lines symbolizing the direction of target motion and analyzed profiles.

The RIT IMRT analysis software was used to measure profiles through both the reference alignment and each experimental film. An example of the analysis is shown in Figure 4.7. The green line is an experiment film profile, compared to the red profile which is from the reference film where the registration marks were used as a template to align all the experiment films. The blue line seen in the profiles measures the difference between the two profiles. The dose of the reference film was irrelevant and was discarded. The reference film image was only used for alignment purposes for all experimental films. The large needle-like spike seen in the blue colored difference profile corresponds to the slight change in the edge of the tape used to affix the film into the film guide for scanning.

Note that the profile is the horizontal profile through the film (perpendicular to the direction of phantom motion). There is relatively no change between the profiles, even though

the dotted red line is from a 30% gated delivery, and the solid green line is from a static phantom delivery with no motion involved.

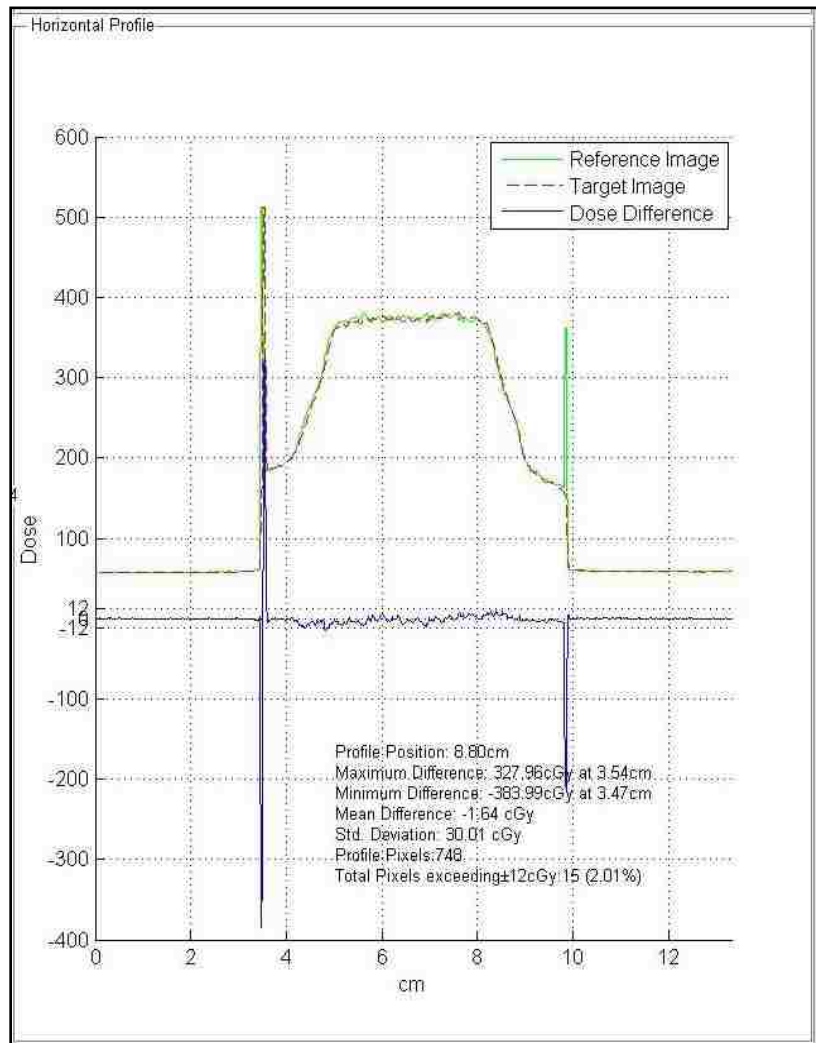


Figure 4.7: RIT software horizontal profile analysis of 30% window level and 20 mm motion gated delivery (target) film registered to the (reference) alignment film. The target motion was perpendicular to the left profile and to the right in the right profile.

First, the three separate stationary phantom plan deliveries were compared to ensure that the registration methods outlined above were correct. If the profiles had the same shape and the same location, then the treatment delivery and film analysis methods would be repeatable.

Vertical dose profiles films from all six gating window deliveries were compared to each other and to the stationary phantom delivery for all five target amplitudes. Vertical profiles were

exported into Microsoft Excel for plotting purposes. All motion profiles were compared to the stationary phantom delivery in terms of displacements of the therapeutic dose (95% dose) levels as well as a low dose (20% dose) level expansion. Figure 4.8 shows a sample set of profiles with marks to identify the measurements taken from each profile. The black lines at 95% and 20% on the left-hand side of the profile indicate an expansion of the gated profiles past the stationary profile. This results in increased normal tissue dose. On the right-hand side of the profile, the red lines at 95% and 20% indicate that the gated profiles are inside those of the static delivery, and the target is being underdosed due to the motion within the gating window. Of the greatest importance is the shift in the 95% isodose location that signifies an under-dose delivered to the CTV. As previously mentioned, the CTV is the central 3 cm ( $\pm 1.5$  cm) that is being covered by the 95% relative dose level from stationary phantom delivery profile. Respiratory motion of the phantom is towards the right-hand side direction in the profile plots, as shown by the gray arrow in Figure 4.8. The left hand of the profile is the superior side of the profile and the right-hand side is the inferior side, as per our definition of a patient breathing with feet towards the gantry breathing with the movements described in Table 4.1.

The black profile in Figure 4.8 is from the static phantom irradiation, which is the ideal CTV coverage. The addition of motion shows obvious deviations from the stationary profile. As the size of the gating window decreases, the profiles more closely match the static phantom delivery. This is due to the beam being on for a smaller portion of time based around on the full exhale position of the phantom. The larger gating windows include more residual motion during the time the beam is turned on, so an increasing amount of the CTV is outside the radiation beam for a larger amount of time.

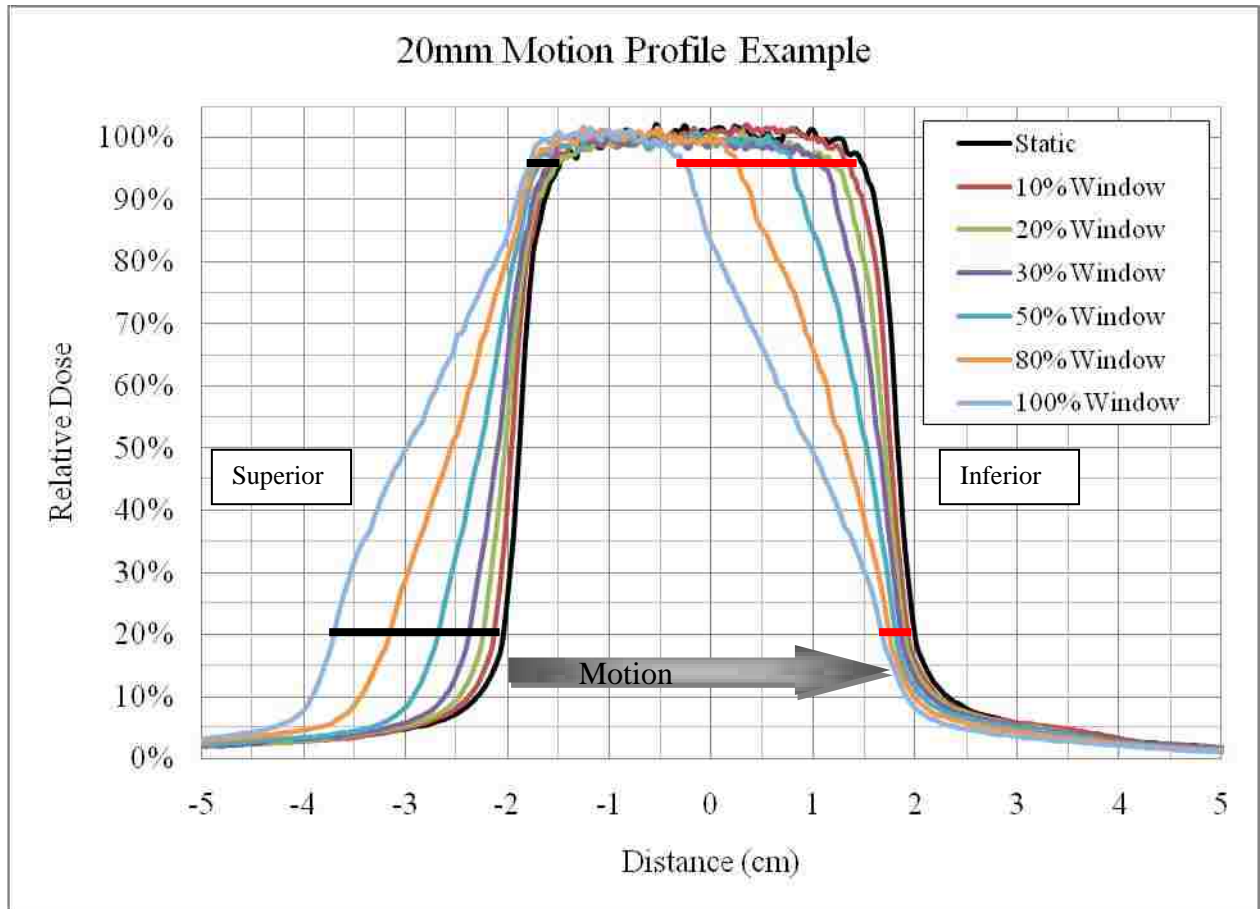


Figure 4.8: Example of 20 mm motion gated profile measurements in relation to static phantom irradiation. The gray arrow represents the direction of target motion from the reference gating level at full-exhale. Black horizontal lines demonstrate how the 100% gating window expands past the static phantom delivery profiles, while red lines indicate a contraction of the dose profile from the static delivery profile.

#### 4.2.5 Margin Expansion Measurements

In this research, target motion was uniform, and therefore, the residual motion of the target during the gating window was known. As shown in Aim 2, the motion of the coil can be tracked to within 0.8 mm of the actual location using the ExacTrac system. The ExacTrac offers one way to directly measure the displacement of the implanted fiducial moves during a fraction of the breathing cycle.

As an initial recommendation, this work evaluated the use of the residual motion during the gating window as an internal margin expansion. A 20 mm amplitude motion was selected for this test because large deviations from the stationary delivery were observed (Figure 4.19), and because treatments with such large respiratory motion would benefit the most gated delivery with optimum margin expansions. The Quasar phantom was set up with reference gating level at full-exhale and 20 mm target respiratory motion. The residual motion was measured during gating window levels of 10, 20, 30 and 100%. Then, for all nine beams, the treatment field size was expanded in the direction of target motion by the expected residual motion for a 10% gating window level (2 mm), a 20% window level (4 mm), a 30% window level (6 mm), and a 100% gating window level (20 mm). These values were calculated from percentage of respiratory amplitude that the gating window covers. For example, if the target is moving with a 20 mm motion and given a 50% gating window, the target will have a residual motion of 10 mm while the beam is on.

#### **4.2.6 Dose-Volume Calculation**

A dose-volume calculation was performed for a gated plan using a 30% window and compared to a plan that does not gate the beam (100% gating window) by encompassing the motion of the target. This evaluation used the 20 mm target motion amplitude and the profile data from the previous section. The profile expansions for a subset of dose levels (10, 20, 30, 40, 50, 60, 70, 80, 90 and 95% relative dose) were measured in the direction of motion. Because the target motion is parallel to the long axis of the CTV (superior-inferior direction of the phantom), the dose distribution in the axial plane will not change significantly. Pinnacle TPS was used to find an average area per unit length for various dose levels. Pinnacle TPS was used because the experimental film was not wide enough (only 6 cm across) to directly measure the lateral dose distribution. Using the measured profile expansions from the previous section, and the dose area



per unit length, we calculated the volumes contained by the selected isodose surfaces. The differences in volumes between the gated plan and the non-gated plan will be used to evaluate the benefit of using respiratory gating when large (20 mm) respiratory motion is considered.

### **4.3 Results**

The Exradin A16 micro ion-chamber measured composite doses of 390 and 396 cGy on the two separate deliveries of the nine-beam plan to the stationary Quasar phantom. The three repeated stationary phantom plan deliveries to film showed an average dose of 390 cGy across the flat, central 3 cm of the profile, which was considered the planning CTV. The ion chamber and film measurements were within 3 cGy or 1% of the mean planning CTV dose (392.6 cGy) calculated by Pinnacle.

For all 9 beams delivered to the phantom in each delivery, no single gated beam took longer than 1 minute to deliver, even with a narrow 10% gating window. The actual treatment time to deliver a gated treatment was not significantly increased over a non-gated delivery. However, the phantom does not take into account any short-term respiratory irregularities of an actual patient, such as coughing, or long term respiratory deviations such a muscle relaxation that might lengthen actual treatment times.

The vertical profiles taken down the central portion of the three stationary phantom delivery films are shown in Figure 4.9. For plotting purposes, the center of the each profile was considered to be at zero distance. The center was determined by measuring the locations of the 50% relative dose level and calculating the mean of the two positions. The 95% dose level occurs at  $\pm 1.5$  cm, corresponding to the desired coverage of the 3-cm wide CTV along this profile as seen in Figure 4.9. Each film was normalized to the average dose of all the profiles from -1.5 to 1.5 cm, which was  $390 \pm 2$  cGy. Doses were normalized to 390 cGy for all films, unless otherwise noted.

The profiles are displayed in terms of relative dose instead of absolute dose to aid in the identification of the 95% therapeutic dose level.

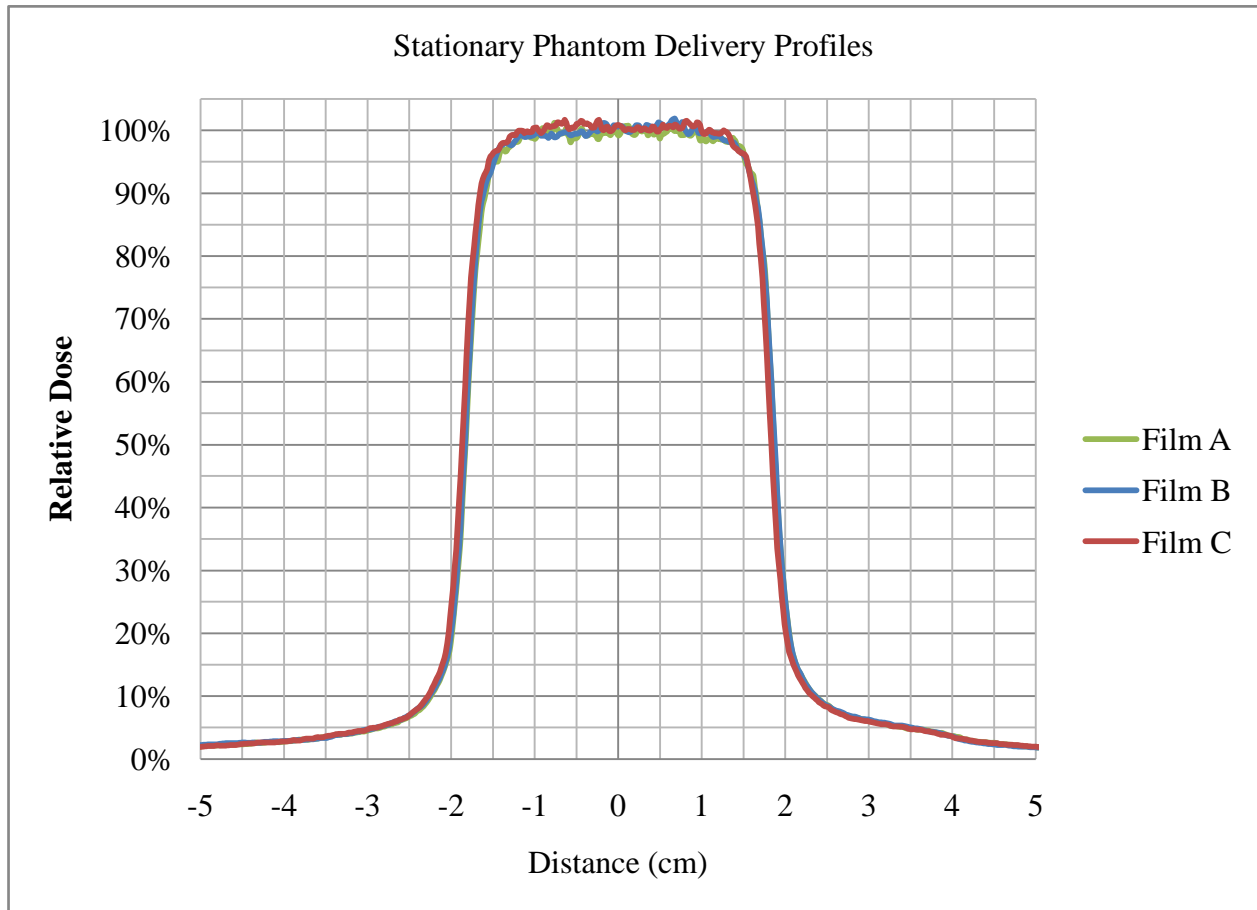


Figure 4.9: Film measurements of three repeated stationary phantom plan delivery profiles.

As measured from the data in Figure 4.9, the horizontal location of the 95% and 20% dose levels from films B and C are within 0.5 mm of the 95% and 20% locations from Film A. This result shows that repeated treatments are accurate to within half of a millimeter. This includes all errors from phantom alignment using the x-ray setup process, from treatment delivery, and from film registration and scanning.

### **4.3.1 5 mm Motion Data**

The profiles resulting from the 5 mm motion measurements are given in Figure 4.10. Table 4.2 shows, for all gating window levels, the measured shift of the profile at the 95% and 20% relative dose levels. Figure 4.11 and 4.12 are plots of the superior-side and inferior-side profile data from Table 4.2. Of particular interest is the 95% dose shift measured on the inferior side, where the CTV does not receive the 95% therapeutic dose level.

For a 5 mm target motion, and small gating windows ( $\leq 30\%$ ) there is almost no difference ( $\leq 1$  mm) from the stationary phantom irradiation profile. From a dosimetric standpoint, gating the beam with a tight gating window ( $\leq 30\%$ ) achieved nearly the same dose profile as the static phantom delivery.

It should be noted, however, that even when gating is not used (100% window), the overall deviation from the static profile is relatively small, due to the small motion of the phantom. As noted in AAPM Report 91 (4.4), it may not be necessary for a clinic to perform gating on a patient when the respiratory motion is only  $\sim 5$  mm. It may be easier to simply expand the CTV appropriately and to not consider gating. Gating windows of 10-50% resulted in CTV under-dose lengths (inferior 95% dose position) of less than 3 mm.

### **4.3.2 10 mm Motion Data**

Figure 4.13 shows the profiles measured with 10 mm of motion for the Quasar phantom. The data show the same trends that were exhibited with 5 mm target motion but larger in magnitude. Table 4.3 lists the measured shifts in the superior and inferior side of the profiles. Figure 4.14 and 4.15 display the isodose shifts from the superior and inferior sides of the profiles. Table 4.3 shows that 8.2 mm of the CTV are under-dosed in the 100% gating window profile.

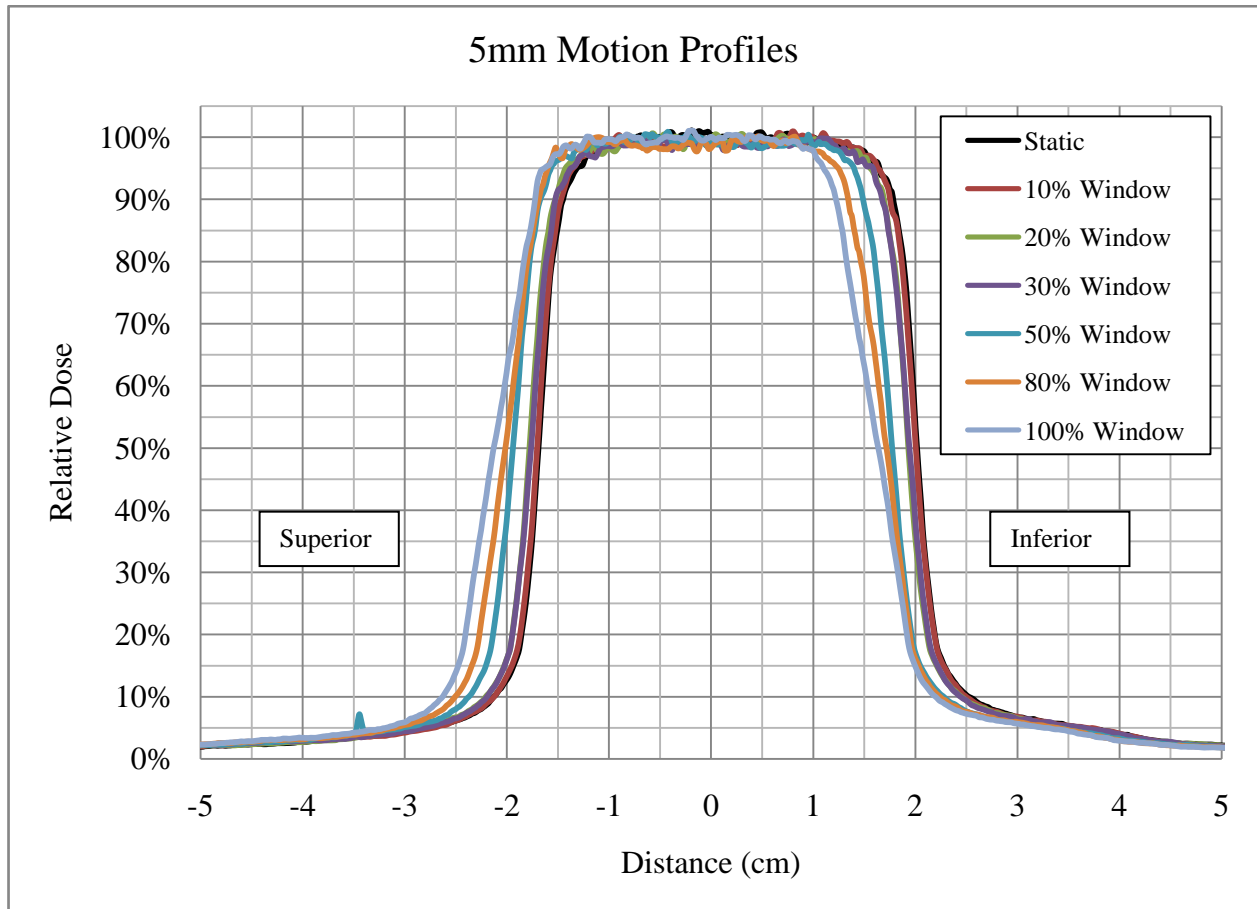


Figure 4.10: 5 mm dose motion profiles for all measured gating windows.

Table 4.2: Measured profile shifts on the superior and inferior side of the 5 mm motion profiles at 95% and 20% relative dose levels.

5 mm Window	Superior Profile Shift (mm)		Inferior Profile Shift (mm)	
	95%	20%	95%	20%
10%	0.3	0.3	-0.1	-0.1
20%	1.0	0.8	-0.8	-0.8
30%	0.4	1.0	-0.6	-0.6
50%	2.4	2.7	-2.4	-2.2
80%	2.7	4.2	-4.0	-2.4
100%	3.1	5.6	-5.4	-2.7

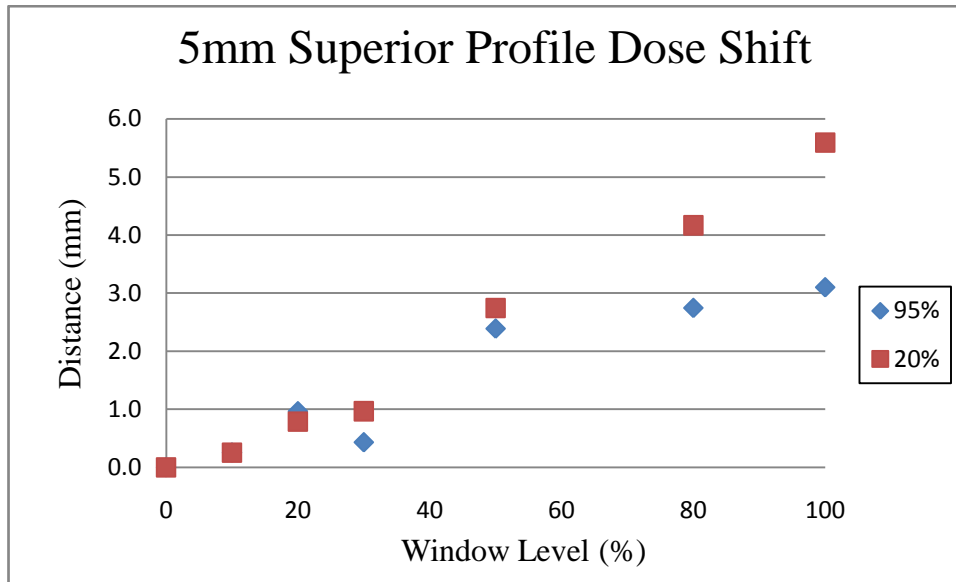


Figure 4.11: Plot of 5 mm motion gated superior-side isodose shift.

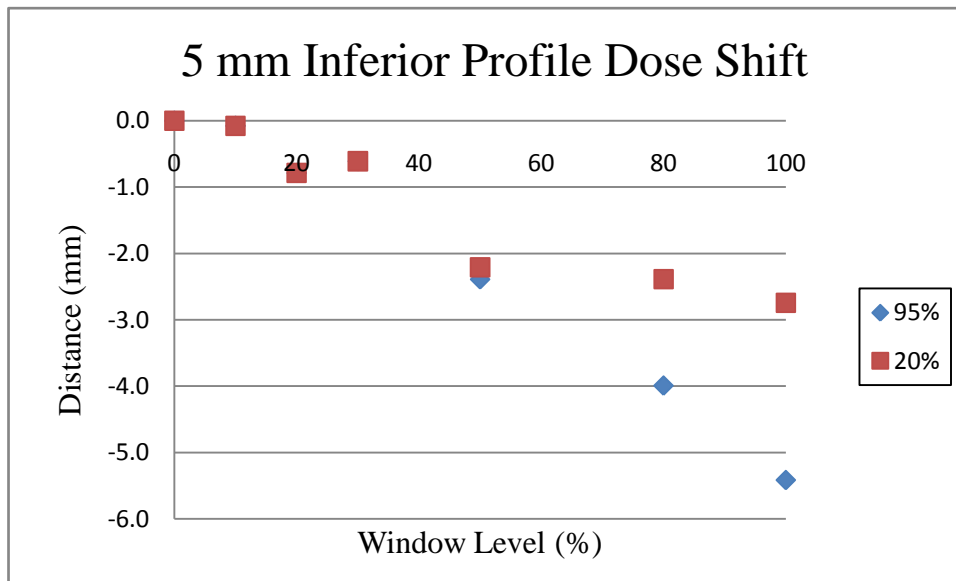


Figure 4.12: Plot of 5 mm motion gated inferior-side profile shift.

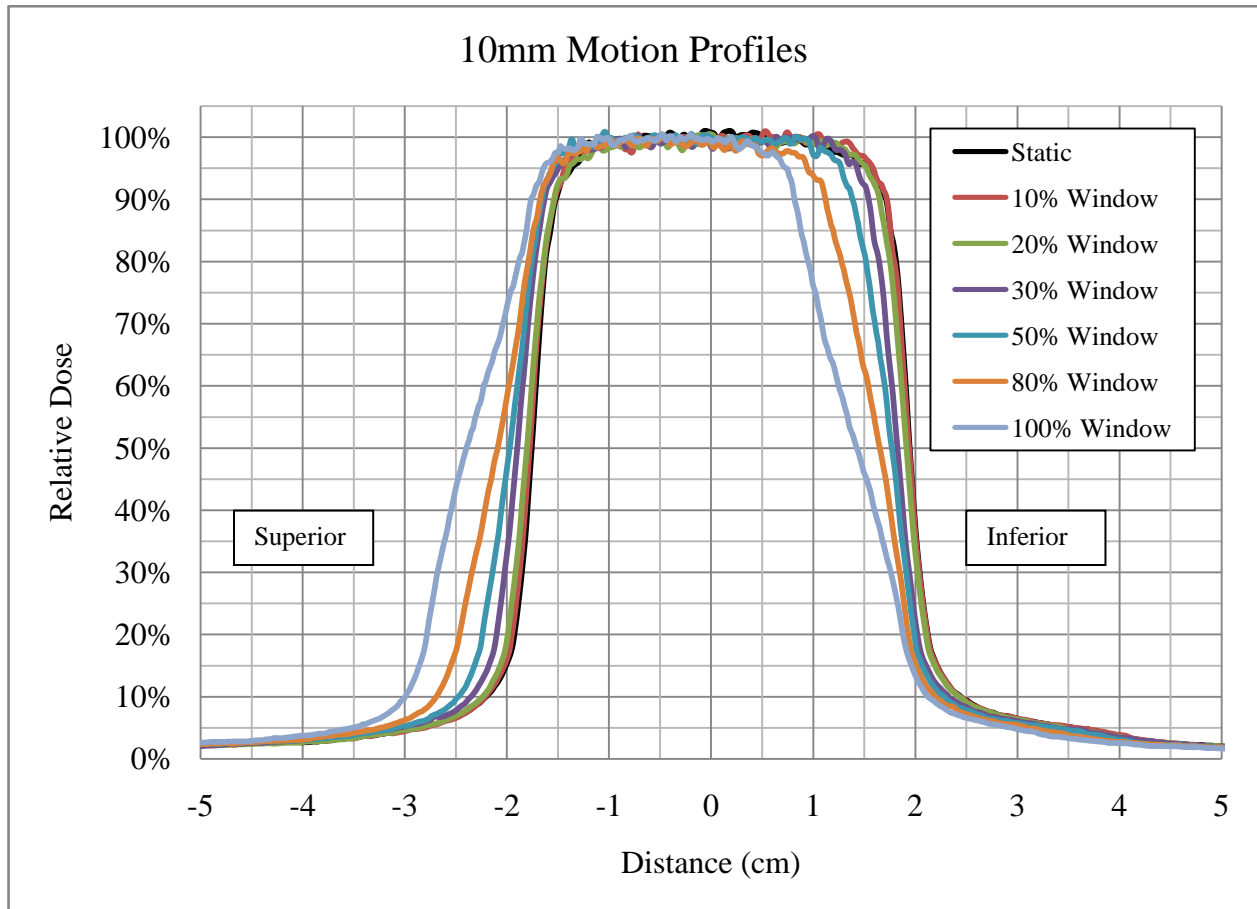


Figure 4.13: 10 mm motion dose profiles for all measured gating windows.

Table 4.3: Measured profile shifts on the superior and inferior side of the 10 mm motion profiles at 95% and 20% relative dose levels.

10 mm Window	Superior Profile Shift (mm)		Inferior Profile Shift (mm)	
	95%	20%	95%	20%
10%	0.7	0.4	0.5	0.0
20%	0.4	0.7	-0.2	-0.2
30%	1.4	1.8	-1.2	-1.1
50%	2.0	3.2	-2.7	-1.2
80%	2.0	5.3	-6.1	-2.0
100%	2.8	8.5	-8.2	-2.5

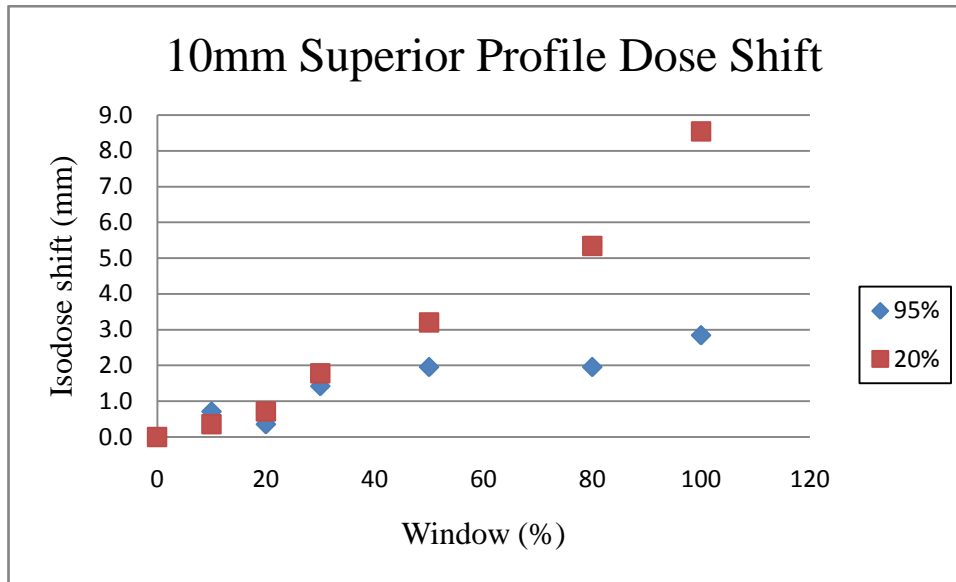


Figure 4.14: Plot of 10 mm motion gated superior-side isodose shift.

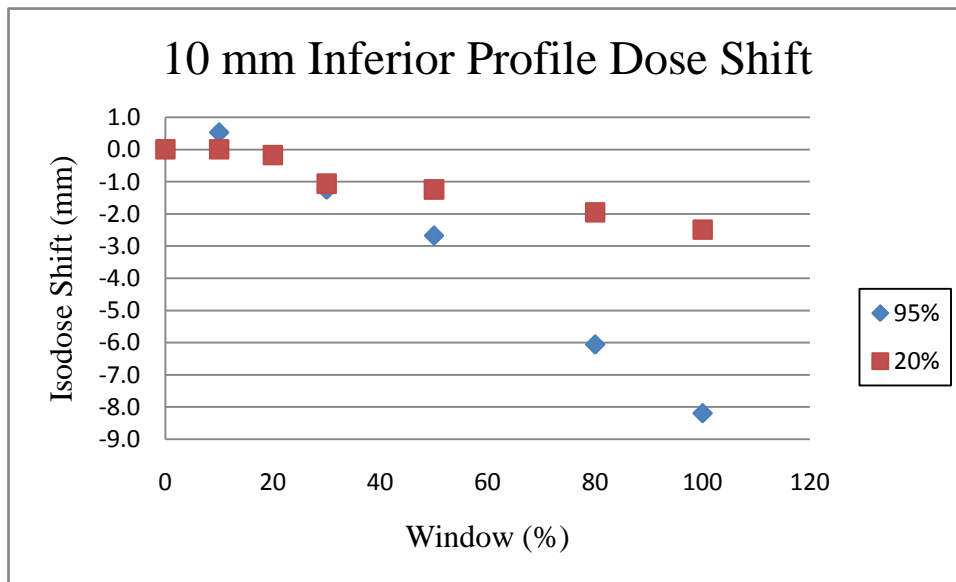


Figure 4.15: Plot of 10 mm motion gated inferior-side isodose shift.

### 4.3.3 15 mm Motion Data

Figure 4.16 shows the profiles measured for the gated delivery using various gating window widths as compared to a static phantom irradiation with an identical delivery. Table 4.4 lists the measured expansions of the gated profiles in comparison to the static profile for the superior and inferior side of the target. Figure 4.17 4.18 give graphic representations of the superior-side and inferior-side data from Table 4.4. As previously noted, the effect of the gating window is more pronounced at larger target amplitudes. However, the shift of the inferior 95% isodose line is still less than 3 mm at the smaller gating windows of 10, 20 and 30%.

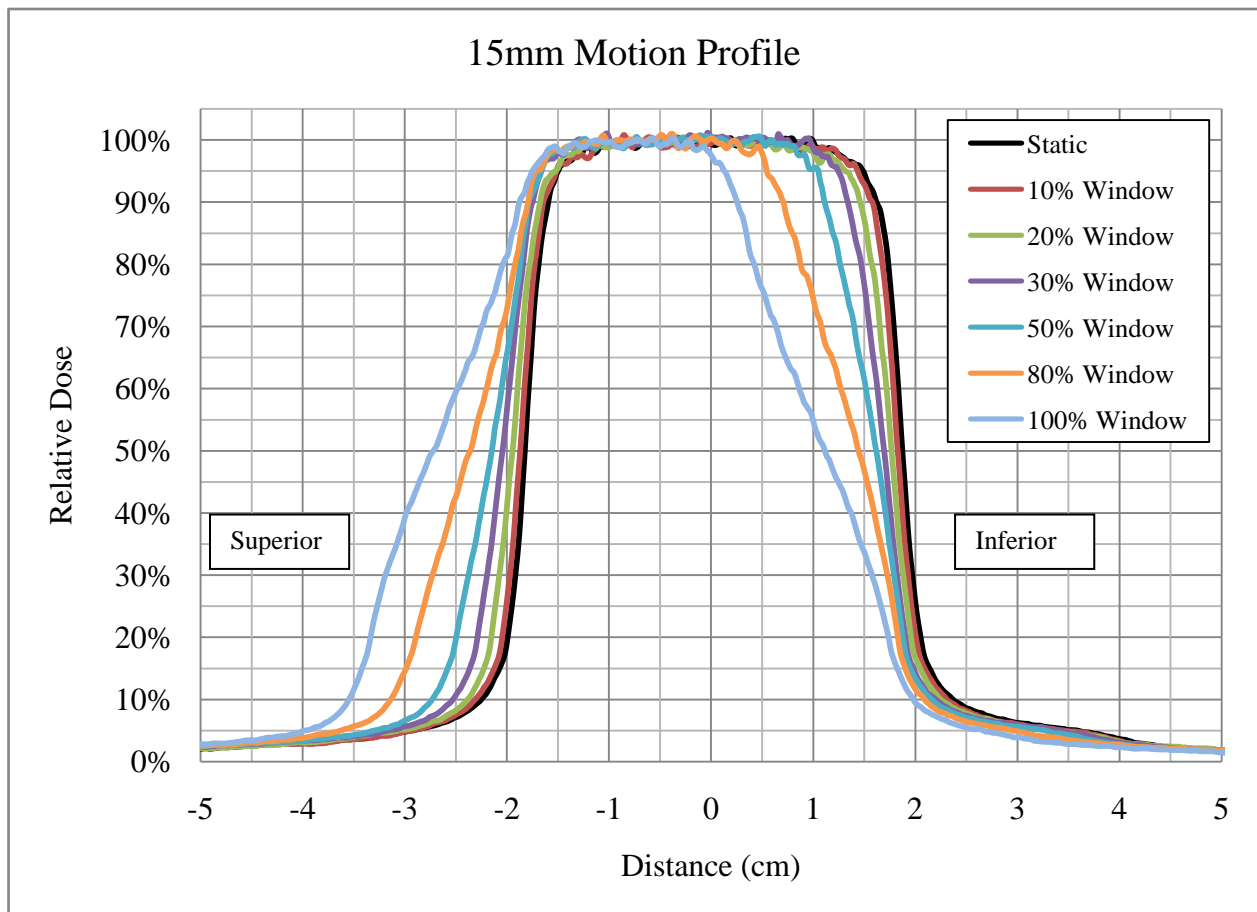


Figure 4.16: 15 mm motion dose profiles for all measured gating windows.



Table 4.4: Measured profile shifts on the superior and inferior side of the 15 mm motion profiles at 95% and 20% relative dose levels.

15 mm <u>Window</u>	Superior Profile Shift (mm)		Inferior Profile Shift (mm)	
	<u>95%</u>	<u>20%</u>	<u>95%</u>	<u>20%</u>
10%	0.2	0.5	-0.5	-0.4
20%	0.4	1.6	-1.6	-0.9
30%	1.6	2.8	-2.3	-1.4
50%	1.6	5.0	-4.3	-1.6
80%	2.1	8.9	-9.3	-2.1
100%	2.5	13.4	-13.5	-3.0

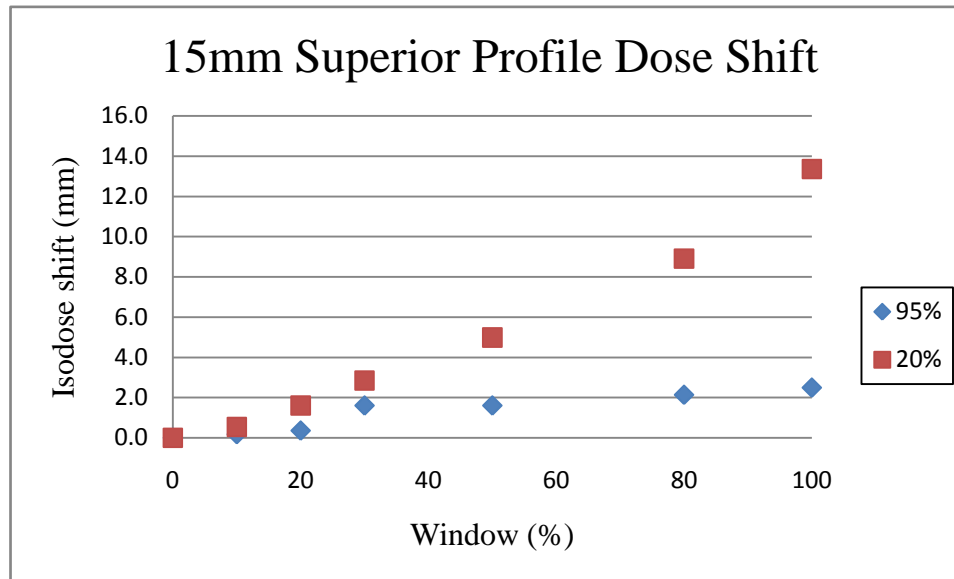


Figure 4.17: Plot of 15 mm motion gated superior-side profile shift.

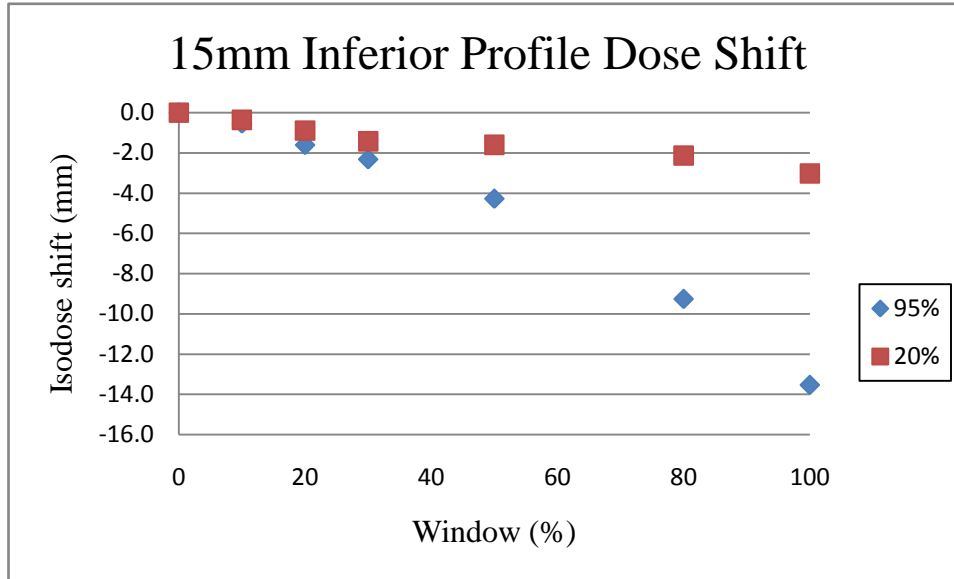


Figure 4.18: Plot of 15 mm motion-gated inferior-side profile shift.

#### 4.3.4 20 mm Motion Data

Figure 4.19 displays the six measured gated-delivery dose profiles compared to the static phantom irradiation. Table 4.5 lists the measured shifts in the superior and inferior sides of the profile. At gating windows of 10-30%, the expansion of the 95% dose level past the static profile is less than 1 mm. Figure 4.20 and 4.21 plot the measured shifts on the superior and inferior sides of the target. As seen in Figure 4.19, the location of the 95% dose level is dramatically shifted with the larger gating windows.

#### 4.3.5 25 mm Motion Data

Figure 4.22 shows the gated profiles in comparison to the static phantom profile for the extreme case of 25 mm target respiratory motion. Using the non-gated (100% window) delivery, only a fraction of the CTV, which was defined from  $\pm 1.5$ cm, receives the therapeutic dose (95%). Table 4.6 lists the profile expansions measured on the superior and inferior side of the

gating profiles. Figure 4.23 and 4.24 give graphic representations of the superior and inferior profile shifts.

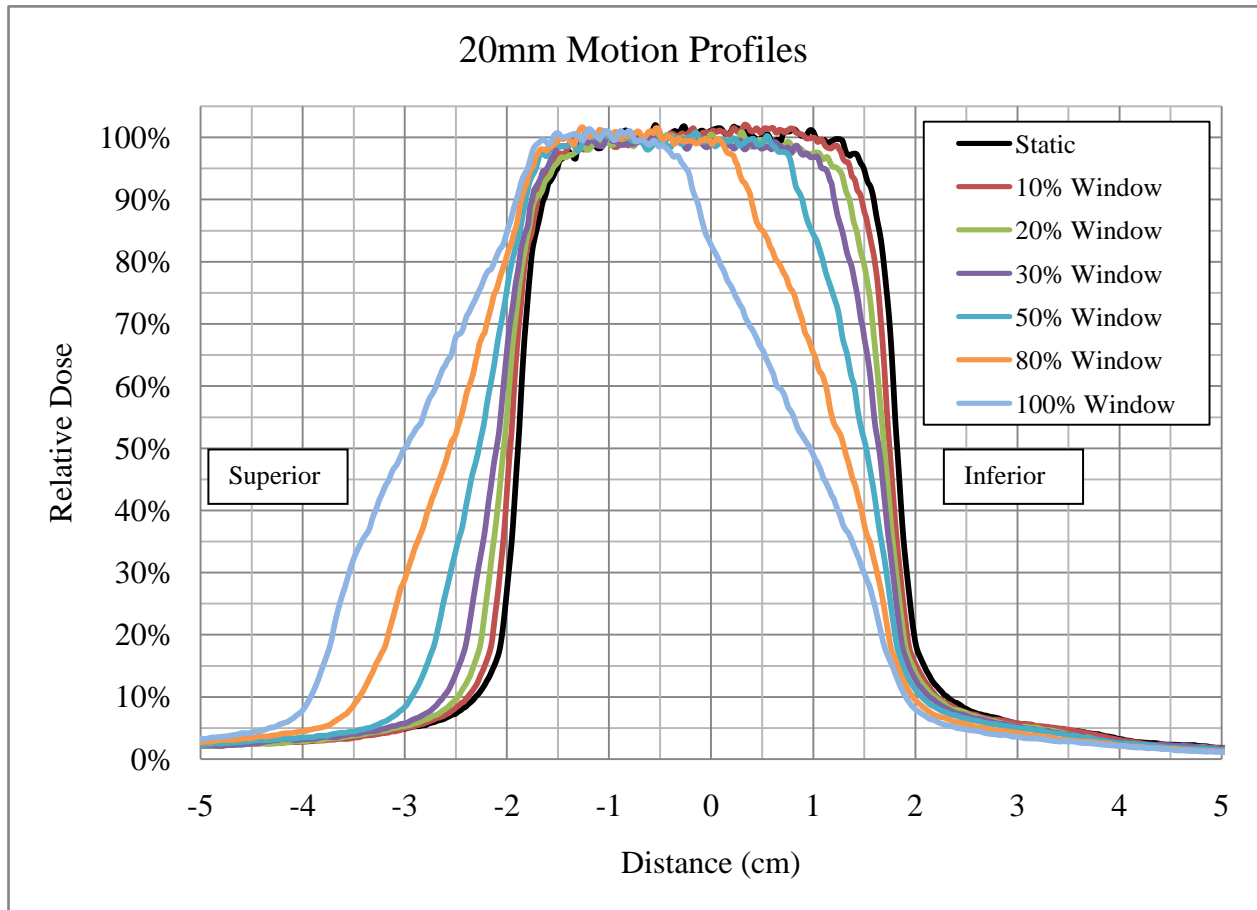


Figure 4.19: 20 mm motion dose profiles for all measured gating windows.

Table 4.5: Measured profile shifts on the superior and inferior side of the 20 mm motion profiles at 95% and 20% relative dose levels.

20 mm Window	Superior Profile Shift (mm)		Inferior Profile Shift (mm)	
	95%	20%	95%	20%
10%	0.7	0.9	-1.2	-0.5
20%	0.4	2.1	-2.5	-0.9
30%	0.9	3.4	-3.9	-1.2
50%	2.0	6.4	-6.9	-1.8
80%	2.5	11.2	-12.3	-2.5
100%	2.8	16.7	-17.4	-3.2

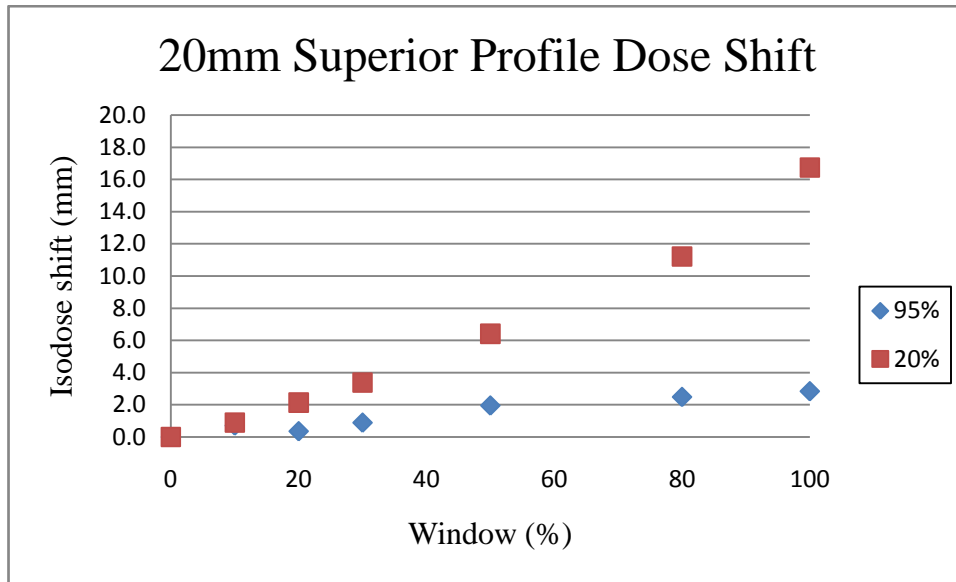


Figure 4.20: Plot of 20 mm motion gated superior-side profile shift.

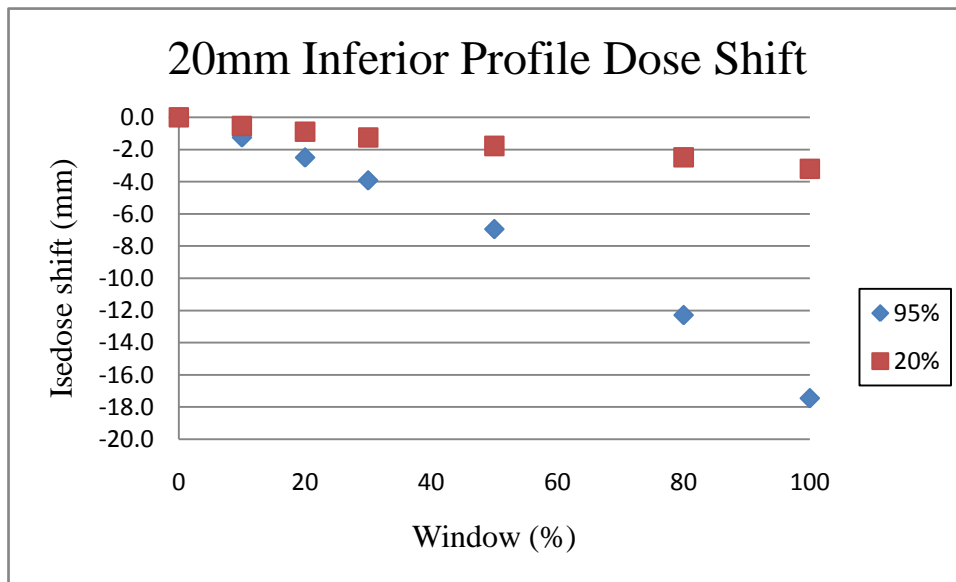


Figure 4.21: Plot of 20 mm motion gated inferior-side profile shift.

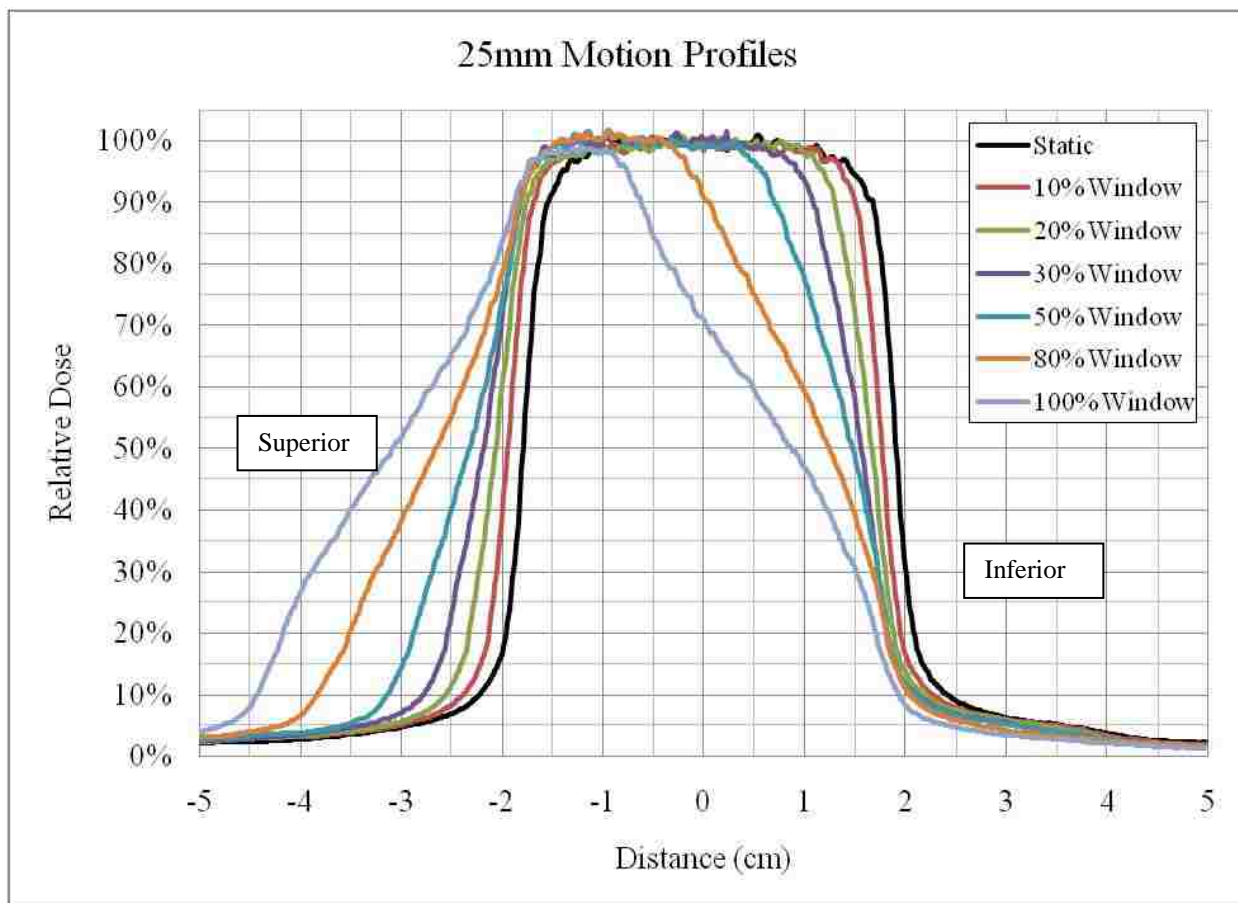


Figure 4.22: 25 mm motion profiles for all measured gating windows.

Table 4.6: Measured profile shifts on the superior and inferior side of the 25 mm motion profiles at 95% and 20% relative dose levels.

25 mm Window	Superior Profile Shift (mm)		Inferior Profile Shift (mm)	
	95%	20%	95%	20%
10%	1.4	1.6	-0.7	-1.2
20%	2.0	3.6	-2.5	-2.0
30%	3.2	5.7	-5.2	-2.7
50%	3.0	9.1	-8.5	-2.7
80%	3.0	15.5	-15.8	-2.7
100%	3.4	21.9	-22.1	-3.7

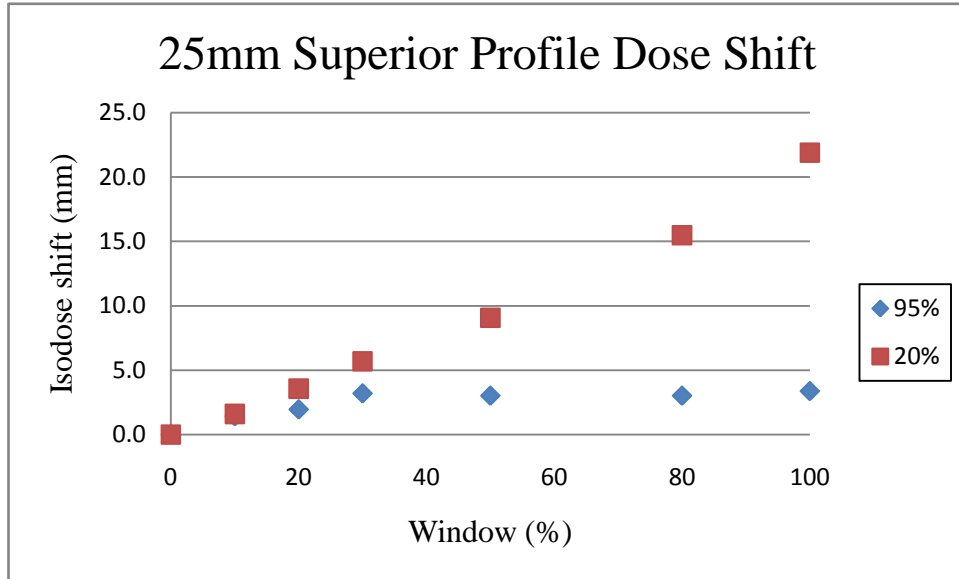


Figure 4.23: Plot of 25 mm motion gated superior-side profile shift.

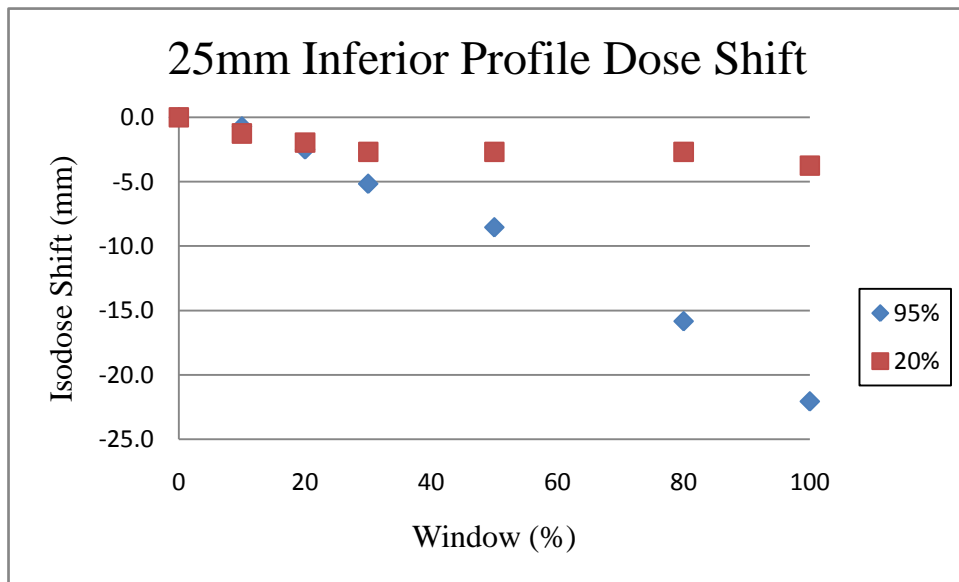


Figure 4.24: Plot of 25 mm motion gated inferior-side isodose shift.

### **4.3.6 Margin Expansion Recommendation**

To evaluate the initial expansion recommendation of using the residual motion for a particular gating window, the measurements of the 20 mm inferior profile shifts were incorporated into the planning system. The residual motions measured with ExacTrac for gating windows of 10, 20, 30 and 100% were 1.7, 3.8, 6.3 and 19.5 mm. These measured values are within 0.5 mm of the expected values of 2, 4, 6, and 20 mm. These differences are less than 0.8 mm, which was the resolution of the ExacTrac system for tracking a moving coil as measured in Aim 2. Therefore, 2, 4, 6, and 20 mm were used as one-dimensional expansions in the direction of motion for 10, 20, 30, and 100% gating windows.

A treatment delivery was performed for each plan with the one-dimensional expansions incorporated for the respective gating window used. Figure 4.25 shows the central film profile of each expanded delivery. Each measured profiles was scaled by the average dose measured across its flat central portion. Because the treatment fields were expanded without a change in monitor units per beam, the output of each field is increased and potentially results in a higher average dose to the target.

The data show that in the case of 10, 20, 30 and 100% gating window levels, expanding the treatment field by the residual motion in the direction of motion results in overdose to some normal tissue in the direction of motion. In the case of the 10% gating window expansion, the treatment field was only expanded by 2 mm and seems to have a negligible difference from the static delivery.

Table 4.7 shows that using the residual motion of the target during the gating to expand the treatment field is larger than necessary. On the inferior side of the profile, for example, the non-expanded fields under-dosed the inferior side of the profile by 3.9 mm at the 30% gating window, but the 6 mm expansion increased the profile past the static phantom profile by 4.3 mm.

The superior-side profiles in Figure 4.26 are relatively unchanged from Figure 4.20 because this side of the treatment field was not expanded. The significant change is the overexpansion of the gated profiles past the static phantom profile on the inferior side.

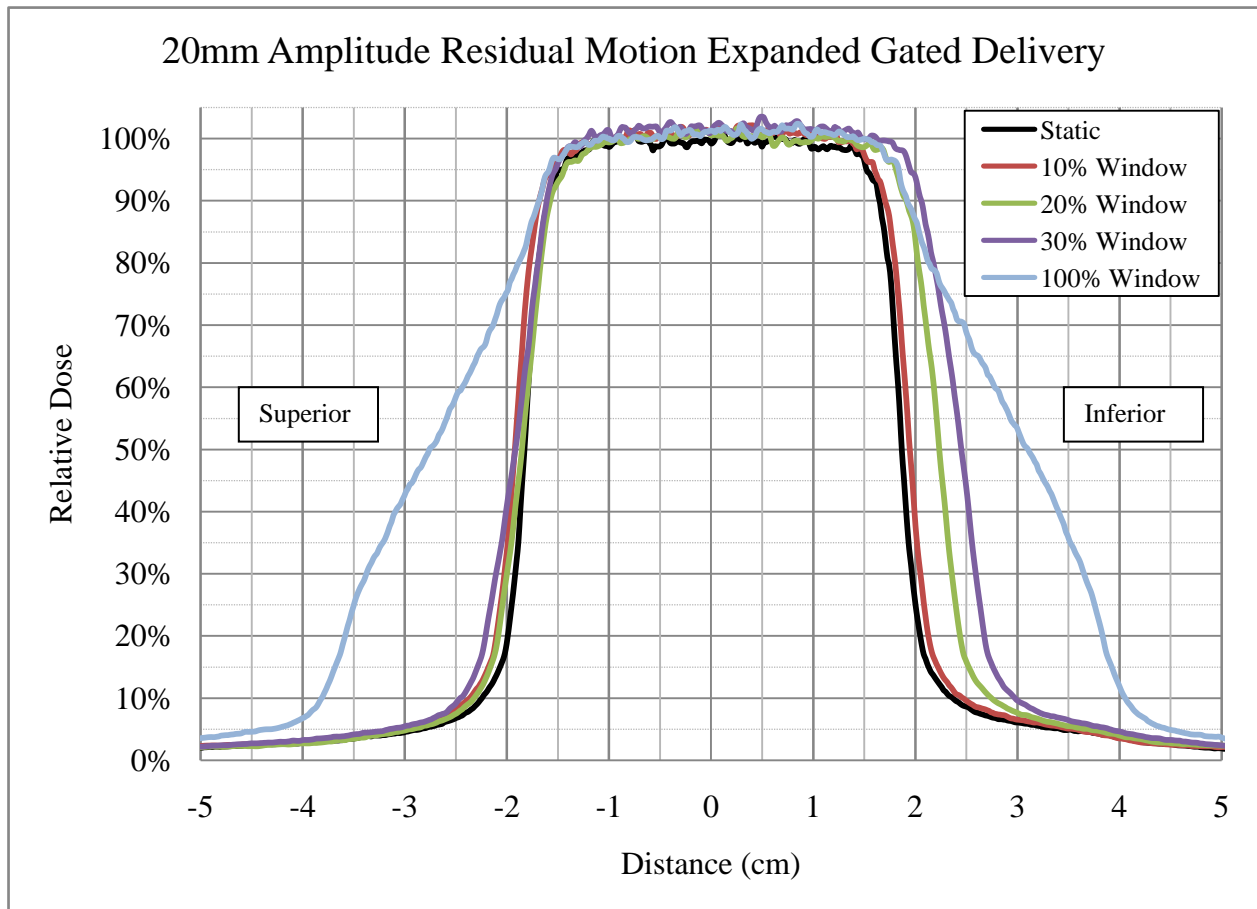


Figure 4.25: 20 mm amplitude motion gated deliveries expanded in the direction of target motion by the residual motion during the gating window.

The main goal of the margin expansions is to provide adequate coverage of the CTV as it moves away from the full-exhale position that the reference gating level is set to. It should be noted in all of the profiles that the gating window also shifts the dose profile past the static delivery on the superior side. This could signal the possibility of shrinking the margins slightly on the superior side of the target, but this was not considered in the margin expansion recommendations used in this project.



Table 4.7: Amount of overexpansion (in mm) beyond the static profile when expanding by the residual motion for the 20 mm motion plan delivered with 10, 20, 30 and 100% gating windows.

Superior Profile Shift (mm)			Inferior Profile Shift (mm)		
<u>Window</u>	<u>95%</u>	<u>20%</u>	<u>Window</u>	<u>95%</u>	<u>20%</u>
10%	1.1	1.2	10%	0.7	0.9
20%	-0.4	1.1	20%	2.7	3.9
30%	0.5	2.3	30%	4.3	6.2
100%	1.2	16.0	100%	2.9	17.8

This project then evaluated expanding the treatment field in the direction of motion by the measured distance of under-dose of the 95% therapeutic dose level on the inferior side of the profile using Table 4.5 for the 20 mm target motion. For a treatment with a gating window of 30%, a one-dimensional field size expansion of 3.9 mm was incorporated in the direction of phantom motion for all nine beams. For treatments that would use gating window widths of 50, 80 and 100%, field size expansions were made for the delivery plan in the direction of motion for all nine beams by 6.9, 12.3, and 17.4 mm, respectively. It should be noted that for a 20 mm uniform target motion, the residual motions of the target during 30, 50, 80, and 100% gating windows are 6, 10, 16 and 20 mm, respectively. As seen in Figure 4.19, the effects of the gating window were to contract the measured inferior dose profile inside the static phantom profile. By expanding these fields, the 95% dose coverage should be re-achieved as seen in the static phantom plan delivery.

Four (30, 50, 80, and 100% gating window level) gated 95%-inferior-dose-shift-expanded plans were delivered to the Quasar phantom. A static phantom delivery of the original, non-expanded plan was also performed. Figure 4.26 shows the corresponding profiles through each of the 4 gated/expanded plans and 1 static phantom delivery as described above.

Note that the superior (left-hand) side of the profiles remains unchanged from the non-expanded, gated deliveries as previous seen in Figure 4.19. As expected on the inferior side of the dose profiles, the 95% dose levels for all 4 margin-expanded deliveries are within 0.8 mm of the 95% dose level of the static phantom delivery profile. This is nearly within the 0.5 mm error limit established from the three stationary profiles from Figure 4.9. By incorporating the project's recommended expansion into the plan delivery, for a 20 mm target motion, similar therapeutic dose coverage of the target was obtained as that of a plan delivered to a stationary phantom.

It should be noted that using a larger gating window results in needing a larger expansion to cover the target. The residual motion increases proportionately to the gating window. The larger residual motion has the disadvantage of delivering dose to larger amounts of normal tissue, as seen in the (low dose) profile expansions in Figure 4.26. This work recommends balancing using as small a gating window as possible without over-extending the amount of time the plan delivery takes due to the smaller beam-on time per respiration.

Table 4.8 lists the recommended margin expansions for various gating windows based on the measured 95% dose profiles. Table 4.9 shows the difference between the data shown in Table 4.8 and the residual motion for each gating window. For a 5 mm and 10 mm target motions, the recommended internal margin expansion is less than 3 mm for gating windows up to 50%. At 15 mm target motion, 10, 20, and 30% gating windows have a recommended margin expansion of less than 3 mm. For 20 mm and 25 mm target motion, the recommended expansion is less than 3 mm only for the 10 and 20% gating window widths.

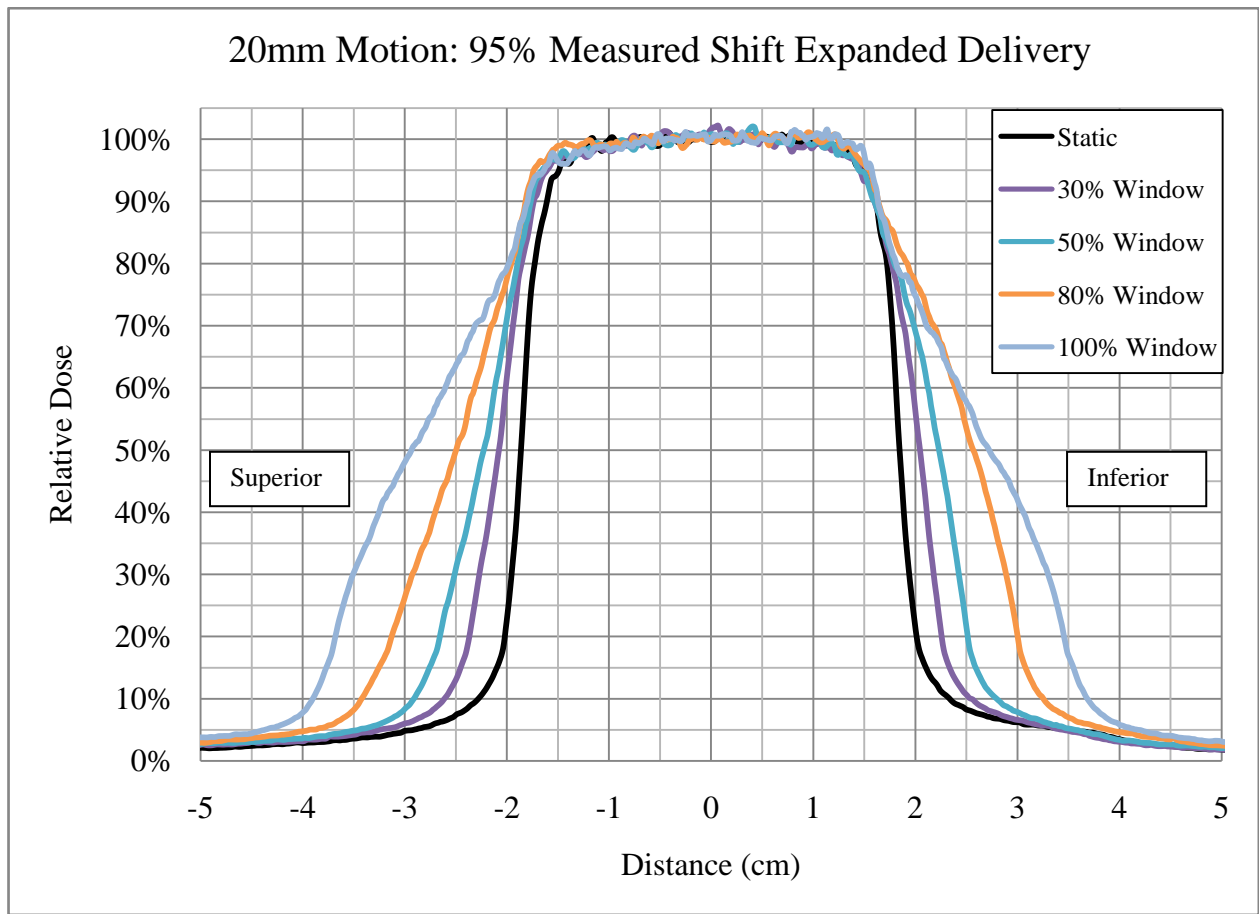


Figure 4.26: 95% dose shift expansion profiles for 30, 50, 80 & 100% gating windows compared to the static phantom delivery.

Table 4.8: Summary of the recommended internal margin expansion based on the size of the 95% under-dose on the inferior side of the gated profile. Gating windows which have a recommended internal margin expansion less than 3 mm for each target motion observed are marked in light green. Gating windows which have a recommended margin larger than 3 mm are marked in light red.

Target Motion (mm)	Recommended margin expansion					
	Gating window					
	10%	20%	30%	50%	80%	100%
5	0.1	0.8	0.6	2.4	4.0	5.4
10	0.5	0.2	1.2	2.7	6.1	8.2
15	0.5	1.6	2.3	4.3	9.3	13.5
20	1.2	2.5	3.9	6.9	12.3	17.4
25	0.7	2.5	5.2	8.5	15.8	22.1

Table 4.9: Difference of recommended margin based on the 95% dose profile shift and the residual motion.

Target Motion (mm)	Gating window					
	10%	20%	30%	50%	80%	100%
5	-0.5	-0.3	-1.1	-0.4	-0.4	-0.1
10	-0.5	-1.8	-1.8	-2.3	-1.9	-1.8
15	-1.0	-1.4	-2.2	-3.2	-2.7	-1.5
20	-0.8	-1.5	-2.1	-3.1	-3.7	-2.6
25	-1.8	-2.5	-2.3	-4.0	-4.2	-2.9

### 4.3.7 Dose-Volume Calculation

The expanded profile data shown in Figure 4.26 were used to estimate increased volumes receiving each dose level (10-95%). While the 95% CTV dose coverage is approximately equal between treatments of a non-gated delivery and a gated delivery, the volume receiving low dose (20%) is increased as an effect of the target motion. This determined the total volume per dose level for a motion-encompassed plan (100% window) and a gated plan (30% window).

Table 4.10 lists the calculations for the plan using a 30% gating window for the dose volumes for a range of dose levels from 10-95%. The “Profile Width” column is the measured overall profile width from Figure 4.26 to estimate the longitudinal dimension for each isodose. “Pinnacle Area/Length” is the estimated area per unit length of each dose level. The column labeled “Dose Volume” is the calculated dose volume using the profile width multiplied by the area per unit length.

Table 4.11 and Table 4.12 show similar data as Table 4.10 using Figure 4.25 to calculate the profile width for the case of the motion (20 mm) encompassed delivery and the static delivery, respectively. The area per unit length calculated from Pinnacle is the same as in Table 4.10, because the effect of the dose shift is in the axis along the direction of motion. Therefore,

the axial dose distribution was considered unchanged for the purposes of this calculation. The total volume was calculated from the product of profile width and pinnacle area per unit length. Only the length of the dose volumes changed due to motion within the gating window.

Figure 4.27 shows that the volume of tissue receiving 20% of the dose is approximately 35% less with 30% gating window delivery than the with motion-encompassed (100% window) delivery. Compared to the static phantom delivery, there is a small increase (approximately 15%) in the 20% dose volume with the 30% gating window delivery. By accounting for the effects of motion with respiratory gating, we can reduce the effect of motion on the delivered dose. From this figure, it is clear that motion-encompassed delivery can adequately cover a target moving with respiration, but the amount of normal tissue receiving low doses is elevated over that of a gated treatment delivery.

Table 4.10: Calculated dose volume data for a 30% gated delivery expanded to cover the CTV.

Dose	Profile Width (cm)	Pinnacle Area/Length (cm)	Dose Volume (cm <sup>3</sup> )
<u>%</u>	<u>30%</u>	<u>30%</u>	<u>30%</u>
10	5.13	273.1	1399.8
20	4.63	234.5	1085.3
30	4.43	107.5	476.4
40	4.29	32.1	137.6
50	4.13	20.9	86.2
60	3.99	11.1	44.4
70	3.83	12.2	46.6
80	3.61	10.3	37.1
90	3.31	8.6	28.4
95	3.06	7.0	21.5

Table 4.11: Calculated dose volume data for a motion-encompassed (100% window level) delivery (20 mm) expanded to cover the CTV.

Dose	Profile Width (cm)	Pinnacle Area/length (cm)	Dose Volume (cm <sup>3</sup> )
<u>%</u>	<u>100%</u>	<u>100%</u>	<u>100%</u>
10	7.57	273.1	2065.7
20	7.14	234.5	1673.9
30	6.78	107.5	729.0
40	6.28	32.1	201.5
50	5.62	20.9	117.4
60	5.02	11.1	55.9
70	4.40	12.2	53.6
80	3.77	10.3	38.7
90	3.44	8.6	29.5
95	3.19	7.0	22.4

Table 4.12: Calculated dose volume data for a static phantom delivery.

Dose	Profile Width (cm)	Pinnacle Area/length (cm)	Dose Volume (cm <sup>3</sup> )
<u>%</u>	<u>Static</u>	<u>Static</u>	<u>Static</u>
10	4.55	273.1	1242.4
20	4.03	234.5	945.1
30	3.9	107.5	419.2
40	3.79	32.1	121.6
50	3.71	20.9	77.4
60	3.63	11.1	40.4
70	3.56	12.2	43.4
80	3.45	10.3	35.4
90	3.23	8.6	27.7
95	2.99	7.0	21.0

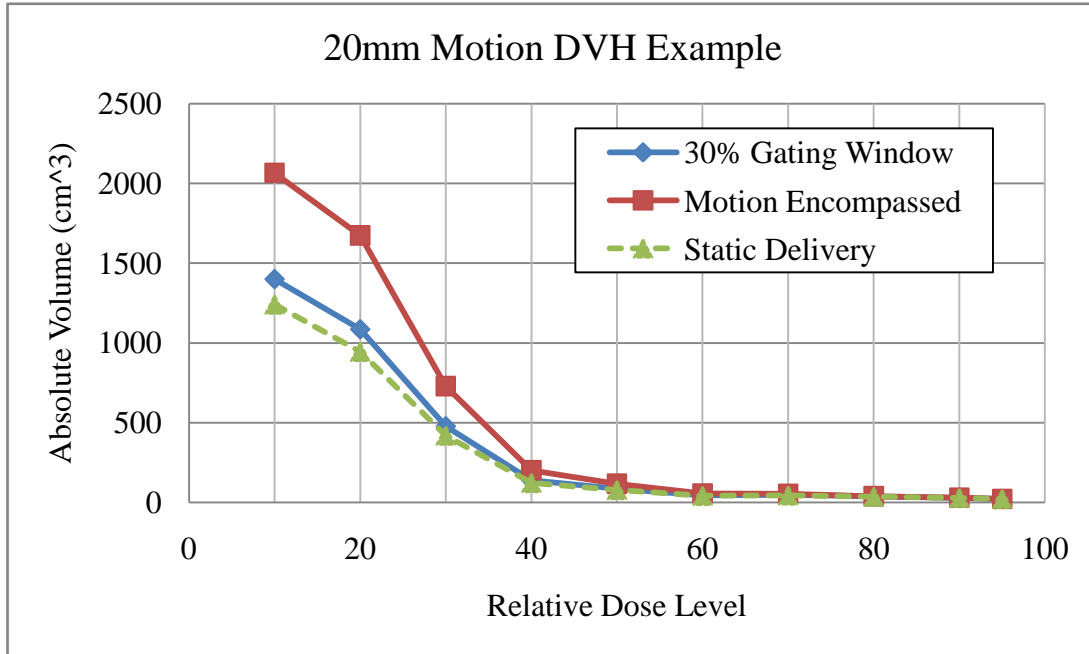


Figure 4.27: Calculated volumes receiving a range of dose levels shown for a comparison of a 30% window gated plan, motion-encompassed (100% gating window) plan, and a stationary phantom delivery with no expansion.

## 4.4 Conclusions

This aim demonstrated that mean target doses measured with radiochromic film and ion chamber measurements agree with Pinnacle-calculated dose to within 1%, and that ExacTrac gating x-ray setup and delivery is accurate to 0.5 mm. We also found that margin expansion in the direction of motion by the expected residual motion proved to be larger than necessary. Coverage of the CTV by 95% dose level was found to be achievable with smaller expansions for all motions and gating windows. The trends of the measured dose profile from each motion amplitude behaved as expected with smaller gating windows producing profiles that more closely matched the shape of the static phantom delivery profile.

An estimate of the phantom volume irradiated with a conventional non-gated plan was compared to a gated plan utilizing a 30% gating window for a cylindrical target with 20 mm

respiratory motion. The CTV coverage achieved with both plans was comparable. However, the volume of tissue receiving 20% of the prescription dose was 35% less for the gated delivery than for the non-gated one. This example demonstrated the ability of gated therapy treatments to spare more normal tissue while maintaining adequate target coverage.

Dose profiles on the superior side of the moving phantom expanded past the static phantom profile, and these margins could in theory be decreased. However, the values of over-expansion on the superior side of the profile were small enough that the potential decrease of those margins was not studied.

This aim demonstrates that using the expected residual motion for margin expansion provides proper target coverage but still irradiates more normal tissue than is optimal. However, the optimal margin expansions measured in this project were limited to a single, simple beam arrangement and a phantom moving in a simple predictable pattern. For patient treatments, the expected residual motion should be used for margin expansion, unless patient-specific measurements are available that demonstrate proper coverage from a smaller expansion.

## 4.5 References

- 4.1. S.S. Vedam, V.R. Kini, P.J. Keall, V. Ramakrishnan, H. Mostafavi, R. Mohan, "Quantifying the predictability of diaphragm motion during respiration with a non-invasive external marker," *Med. Phys.* 30, 505-513 (2003).
- 4.2. P. C. M. Chi, P. Balter, D. Luo, R. Mohan, and T. Pan, "Relation of external surface to internal tumor motion studied with cine CT," *Med. Phys.* 33, 3116-3123 (2006).
- 4.3. C. R. Ramsey, I. L. Cordney, and A. L. Oliver, "A comparison of beam characteristics for gated and nongated clinical x-ray beams," *Med. Phys.* 26, 2086-2091 (1999)
- 4.4. P.J. Keall, G. S. Mageras, J. M. Butler, R. S. Emery, K. M. Forster, S. B. Jiang, J. M. Kapatoes, D. A. Low, M. J. Murphy, B. R. Murray, C. R. Ramsey, M. B. Van Herk, S. S. Vedam, J. W. Wong, E. Yorke, "The management of respiratory motion in radiation oncology report of AAPM Task Group 76," *Med. Phys.* 33, 3874-3900 (2006).



## **5 Conclusions**

### **5.1 Aim 1**

Both the Epson and Vidar scanners showed equivalent performance in terms of scanner repeatability, uniformity, and noise. The Epson scanner performed better than the Vidar scanner in a few categories such as scanner/film noise and scanner uniformity of a blank sheet of film.

One problem with the Epson scanner is the lack of self-calibration of the light source or warm-up test. The user must simply take many preview scans with the Epson scanner and assume the scanner is adequately warmed up. Other issues are the lack of support from the Epson Corporation in regards to medical physics applications and the lack of FDA clearance. Without FDA constraints, graphic arts scanner manufacturers can substitute components and firmware without notice, possibly resulting in significant differences between scanners. Finally, the lack of adequate commercial software for film dosimetry is a major disadvantage.

With the Vidar scanner, a problem was observed with the leading and trailing edges of a scanned film. The leading and trailing edge of the film profile perpendicular to the light source measured a 3% increase in pixel value. The artifacts can be avoided by ignoring the leading and trailing inch of film in a film scan, or by affixing a piece of film to a larger film guide for transportation through the Vidar scanner. The EBT manufacturer recommends, and will provide, a clear polyester sleeve to secure the film (both cut film pieces and whole sheets) when using the Vidar scanner. We found these sleeves to be unacceptable because of circular Newton ring artifacts. When small pieces of cut film are to be analyzed in the Vidar system, they should be attached to a larger film guide for transportation through the Vidar scanner. When a film guide is not used, the leading and trailing inches in the scanned image should not be used.

All film analysis in this project allowed 24 hours between irradiation and scanning. There was no evidence that 24 hours was required, but this time frame was convenient for this work.

Many reports in the literature use a smaller time interval, such as six hours. The film manufacturer recommends waiting at least two hours after irradiation to scan EBT film.

Film-to-film variations within a single batch were very low with a standard deviation of the film response less than 0.51 percent. Therefore, a single calibration film is adequate for an entire batch. However, batch-to-batch variation was significant, so that each batch must be individually calibrated.

## **5.2 Aim 2**

From 4DCT studies of the measured coil length it was determined that at end-respiration (full-exhale and full-inhale), motion induced coil artifacts were less than a millimeter. This work demonstrated that when identifying a coil on phase-sorted CT datasets, a user can locate the coil endpoints with a variation less than 0.5 mm. This aim concluded that 4DCT phase-sorted datasets corresponding to full-exhale and full-inhale would provide the most accurate image of the moving phantom. Due to the mechanics of breathing, exhalation in actual patients is usually more stable and reproducible than inhalation. This project recommends using a full-exhale dataset for treatment planning system calculations and gating the radiation treatment about the full-exhale (50%) phase of respiration.

When determining the extent of a phantom's respiratory motion with an implanted surrogate such as a coil, the ExacTrac system performs better than 4DCT at coil localization. To accurately determine the direction and extent of phantom's internal respiratory motion after coil implantation, this aim recommends using the ExacTrac system. The ExacTrac can localize a moving coil to within 0.8 mm of the expected position, while 4DCT registered errors up to 5.5 mm from the expected coil endpoint position.

For a patient with well-behaved (e.g., no coughing, gasping, or sudden motions) chest wall motion, this work suggests that the ExacTrac system can localize an implanted coil to

within 1 mm. Thus, for patients with an implanted coil, the extent of tumor motion could directly be measured for use in treatment planning and selection of gating parameters.

### **5.3 Aim 3**

This aim demonstrated that mean target doses measured with radiochromic film and ion chamber measurements agree with Pinnacle-calculated dose to within 1%, and that ExacTrac gating x-ray setup and delivery is accurate to 0.5 mm. We also found that margin expansion in the direction of motion by the expected residual motion proved to be larger than necessary. Coverage of the CTV by 95% of the isocenter dose was found to be achievable with smaller expansions for all motions and gating windows.

An estimate of the phantom volume irradiated with a conventional non-gated plan was compared to a gated plan utilizing a 30% gating window for a cylindrical target with 20 mm respiratory motion. The CTV coverage achieved with both plans was comparable. However, the volume of tissue receiving 20% of the prescription dose was 35% less for the gated delivery than for the non-gated one. This example demonstrated the ability of gated therapy treatments to spare more normal tissue while maintaining adequate target coverage.

Dose profiles on the superior side of the moving phantom expanded past the static phantom profile, and these margins could in theory be decreased. However, the values of over-expansion on the superior side of the profile were small enough that the potential decrease of those margins was not studied.

The results demonstrate that using the expected residual motion for margin expansion provides proper target coverage but still irradiates more normal tissue than is optimal. However, the optimal margin expansions measured in this project were limited to a single, simple beam arrangement and a phantom moving in a simple predictable pattern. For patient treatments, the

expected residual motion should be used for margin expansion, unless patient-specific measurements are available that demonstrate proper coverage from a small expansion.

## **5.4 Recommendations**

This work has demonstrated that in a simple system, margin expansion based on residual motion during gating provides proper target coverage with reduced normal tissue dose compared to non-gated delivery. Extrapolating to patient treatments suggests that target margins should be set using the residual motion during gating. For patients without implanted coils, the residual motion can be computed based on the target motion measured from 4DCT and the size of the gating window. For patients with implanted coils, the ExacTrac system can be used to directly measure residual tumor motion during gating.

## **5.5 Response to Hypothesis**

The hypothesis of this work was that gated delivery combined with 4DCT could limit internal margins to less than 3 mm while maintaining 95% prescription dose coverage of moving targets. The hypothesis was found to be true for gating windows of 10% and 20% for target motions up to 25 mm. For smaller motions (5mm and 10 mm), it was true with gating windows up to 50%.

## **5.6 Future Work**

One limitation of this work was the use of a one-dimensional respiratory phantom. The sinusoidal motion utilized throughout this study allowed for predictable and repeatable testing, but a patient will exhibit neither characteristic. The next step of this work is to repeat the coil localization studies on an anthropomorphic phantom which can mimic actual patient motion in more than one dimension. The film measurements and margin recommendations in Aim 3 conclusions should be extended into three-dimensional motion. The effect of patient respiratory

irregularities on the delivered dose should also be characterized before designing gated treatments for patients.

## **Vita**

Jason Edward Matney was born November 27, 1981 in Richmond, Indiana. He is the son of James E. and Linda C. Matney. He grew up on a small dairy farm owned and operated in the Matney family for four generations. Jason graduated from Hagerstown High School in 2000 and went on to attend Ball State University in Muncie, Indiana. He double majored in physics and mathematics, with a minor in astronomy. After graduation he attended Louisiana State University for a master's degree in medical physics.

Jason enjoys cooking and random road trips. He also enjoys college football, particularly SEC and LSU football. In his free time, Mr. Matney is attempting to perfect his beer tasting palate, Frisbee toss, and golf swing.

Permanent Address:  
2637 N. Jacksonburg Rd.  
Cambridge City, IN 47327